

PRECISE HEIGHT ESTIMATION BY DIFFERENTIAL AMPLITUDE MEASUREMENT
FOR AN AIRBORNE CW DOPPLER PROXIMITY SENSOR

A THESIS SUBMITTED TO
THE GRADUATE SCHOOL OF NATURAL AND APPLIED SCIENCES
OF
MIDDLE EAST TECHNICAL UNIVERSITY

BY

AYDIN VURAL

IN PARTIAL FULFILLMENT OF THE REQUIREMENTS
FOR
THE DEGREE OF PHILOSOPHY OF DOCTORATE
IN
ELECTRICAL AND ELECTRONICS ENGINEERING

SEPTEMBER 2012

Approval of the thesis:

**PRECISE HEIGHT ESTIMATION BY DIFFERENTIAL AMPLITUDE
MEASUREMENT FOR AN AIRBORNE CW DOPPLER PROXIMITY SENSOR**

submitted by **AYDIN VURAL** in partial fulfillment of the requirements for the degree of
**Philosophy of Doctorate in Electrical and Electronics Engineering Department, Middle
East Technical University** by,

Prof. Dr. Canan Özgen _____
Dean, Graduate School of **Natural and Applied Sciences**

Prof. Dr. İsmet ERKMEN _____
Head of Department, **Electrical and Electronics Engineering**

Prof. Dr. Altunkan HIZAL _____
Supervisor, **Electrical and Electronics Engineering Dept., METU**

Assoc. Prof. Dr. Şimşek DEMİR _____
Co-supervisor, **Electrical and Electronics Engineering Dept., METU**

Examining Committee Members:

Prof. Dr. Sencer KOÇ _____
Electrical and Electronics Engineering Dept., METU

Prof. Dr. Altunkan HIZAL _____
Electrical and Electronics Engineering Dept., METU

Prof. Dr. Erdem YAZGAN _____
Electrical and Electronics Engineering Dept., Hacettepe Univ.

Assoc. Prof. Dr. Çağatay CANDAN _____
Electrical and Electronics Engineering Dept., METU

Assoc. Prof. Dr. Ali Özgür YILMAZ _____
Electrical and Electronics Engineering Dept., METU

Date: _____

I hereby declare that all information in this document has been obtained and presented in accordance with academic rules and ethical conduct. I also declare that, as required by these rules and conduct, I have fully cited and referenced all material and results that are not original to this work.

Name, Last Name: AYDIN VURAL

Signature :

ABSTRACT

PRECISE HEIGHT ESTIMATION BY DIFFERENTIAL AMPLITUDE MEASUREMENT FOR AN AIRBORNE CW DOPPLER PROXIMITY SENSOR

VURAL, Aydın

Ph.D., Department of Electrical and Electronics Engineering

Supervisor : Prof. Dr. Altunhan HIZAL

Co-Supervisor : Assoc. Prof. Dr. Şimşek DEMİR

September 2012, 110 pages

Airborne Continuous Wave (CW) Doppler proximity sensors are very sensitive, but leaks precise height measurement. It may be possible to estimate the height at the terminal phase (the case where the sensor is close to terrain) precisely by using the Doppler shift and amplitude information. The thesis includes this novel concept with theoretical analysis and simulation results.

Keywords: Doppler Shift, Land Clutter, Proximity Fuze, Radio Sensing

ÖZ

HAVADAN BIRAKILAN SÜREKLİ DALGA DOPPLER YAKLAŞMA SENSÖRLERİNDE DİFERANSİYEL GENLİK ÖLÇÜMÜ İLE HASSAS YÜKSEKLİK TAHMİNİ

VURAL, Aydın

Doktora, Elektrik ve Elektronik Mühendisliği Bölümü

Tez Yöneticisi : Prof. Dr. Altunkan HIZAL

Ortak Tez Yöneticisi : Doç. Dr. Şimşek DEMİR

Eylül 2012, 110 sayfa

Havadan bırakılan sürekli dalga Doppler yaklaşma sensörleri oldukça hassastır, ancak hassas yükseklik ölçümlerinde eksik kalırlar. Doppler kayması ve genlik bilgisini kullanarak mesafeyi son safhada (sensörün yeryüzüne yakın olduğu durumda) hassas olarak tahmin etmek mümkün olabilir. Tez bu yeni konsept için teorik analizleri ve simülasyon sonuçlarını içermektedir.

Anahtar Kelimeler: Doppler Kayması, Yeryüzü Kargaşası, Yaklaşma Sensörü, Radyo Algılaması

To my Wife (Elit AYDIN VURAL), Mother (Güler VURAL) and Sister (Gülden VURAL).

ACKNOWLEDGMENTS

I would like to express my deepest gratitude to my Supervisor Prof.Dr. Altuncan HIZAL and Co-Supervisor Assoc.Prof.Dr. ŐimŐek DEMİR for their guidance and trust on me. I thank my wife Elit AYDIN VURAL for her unlimited support during the long study period.

TABLE OF CONTENTS

ABSTRACT	iv
ÖZ	v
ACKNOWLEDGMENTS	vii
TABLE OF CONTENTS	viii
LIST OF TABLES	xi
LIST OF FIGURES	xii
CHAPTERS	
1 INTRODUCTION	1
1.1 Radio Sensing for Proximity Fuzes	1
1.2 General Height Estimation Techniques used in Proximity Fuzes	2
2 PROXIMITY SENSING CAPABILITIES OF FUZES	5
2.1 Proximity Fuzes	5
2.1.1 Fuzes for Army Munitions	6
2.1.2 Fuzes for Airborne Ballistic Munitions	9
2.1.3 Proximity Capabilities of Proximity Sensors/Fuzes	13
3 HEIGHT ESTIMATION USING DIFFERENTIAL AMPLITUDE MEASUREMENTS	15
3.1 Theory of the Height Estimation Method	15
3.1.1 Land Clutter and Normalized Cross Section	20
3.1.1.1 Radar Cross Section	20
3.1.1.2 Normalized RCS	22
3.1.1.3 Fluctuation Statistics for Clutter Modelling	25
Autocorrelation Function and Power Density Spectrum	25
Fluctuation Statistic	26

	Common Distributions	26
	Decorrelation Time for the Land Clutter	27
	3.1.1.4 Mathematical Clutter Model	29
	3.1.2 Error Correction Factor	33
4	SIMULATION FOR FLAT TERRAIN	39
4.1	Simulation (Flat Terrain)	39
4.2	Estimation Results for the Flat Terrain	40
4.3	Noise Analysis	43
	4.3.1 Effect of VCO Phase Noise	44
	4.3.2 Thermal Noise	50
	4.3.3 Noise Reduction	52
	4.3.3.1 Moving Average Filtering for Noise Reduction	53
	4.3.3.2 Linear Regression (LR) for Noise Reduction	54
5	SIMULATION FOR DOUBLE-PLANE TERRAIN	58
5.1	Simulation for Double-Plane Terrain	58
	5.1.1 Calculating Reflection from a Rectangular Patch	59
	5.1.2 Simulation (Double-Plane Terrain)	62
	5.1.3 Simulation Results (Double-Plane Terrain)	64
5.2	Simulation for a Terrain which is Generated by DTED	66
	5.2.1 Digital Terrain Elevation Data (DTED) Structure	66
	5.2.2 Simulation (DTED Terrain)	69
	5.2.2.1 Triangulation of DTED	71
	5.2.2.2 Calculation of Parameters	73
	5.2.2.3 Simulation GUI	76
	5.2.3 Simulation Results (DTED Terrain)	76
5.3	Doppler Shift Spectrum	79
5.4	Return Power from a Side Patch	81
6	CONCLUSION	86
6.1	Height Estimation Method	86
6.2	Future Studies	87

REFERENCES	89
APPENDICES	
A MATLAB CODES IN THE SIMULATION	92
A.1 Codes for Estimating Height from a Single Planar Surface	92
A.1.1 Calculating Trajectory of the Ballistic Platform	92
A.1.2 Generating Exponential Model of the Land Clutter	93
A.1.3 Calculating Correction Factor by Initial Conditions	94
A.1.4 Calculating Reflected Power from the Terrain	95
A.1.5 Graphical User Interface (GUI) Initialization (Automati- cally Generated by MATLAB™)	96
A.1.6 Height Estimation and Displaying Results in GUI	98
A.2 Codes for Estimating Height from the Terrain Composed of Two-Planes	102
A.2.1 Calculating Reflected Power from Two-Planes	102
A.3 Codes for Estimating Height from the Terrain Generated Using DTED	104
A.3.1 Calculating Trajectory over DTED Terrain	104
A.3.2 Adjusting DTED Limits	105
A.3.3 Decreasing DTED Resolution (Increase in DTED Spacing)	107
A.3.4 Triangulation and Calculation Reflections from Clutter El- ements	108
CURRICULUM VITAE	110

LIST OF TABLES

TABLES

Table 2.1	Proximity Fuzes	13
Table 3.1	Decorrelation Time at 3.6 GHz for Open-Wood Type Terrain	28
Table 3.2	Measured Clutter Data for Grazing Angles between 20° to 70°	29
Table 3.3	Clutter Model Parameters (a,b,c,d) for Various Terrain Types	32
Table 4.1	Thermal Noise Levels at Different Ports of the Receiver	52
Table 5.1	Matrix Intervals for DTED	68
Table 5.2	Release Parameters for DTED Simulation	77

LIST OF FIGURES

FIGURES

Figure 1.1 Conventional Proximity Sensor Triggering	3
Figure 2.1 General Purpose Bomb	6
Figure 2.2 Mortar Projectile	6
Figure 2.3 Artillery Projectile	6
Figure 2.4 M734A1 Proximity Fuze (Mounted)	8
Figure 2.5 M782 Multi-Option Fuze for Artillery (MOFA)	8
Figure 2.6 Proximity Fuze Configurations for General Purpose Bombs	10
Figure 2.7 MK 43 MOD 1 Target Detecting Device	11
Figure 2.8 High Accuracy Radar Proximity Sensor (HARPS)	12
Figure 2.9 Burst Height of HARPS	12
Figure 2.10 DSU-33 C/B Proximity Sensor	13
Figure 3.1 Clutter Element in Spherical Coordinate System	16
Figure 3.2 Angle Definitions	17
Figure 3.3 Length of the Differential Area, $d\rho$	18
Figure 3.4 PSD of Doppler Shift ($h_0 = 100$ m and $\zeta = 60^\circ$)	21
Figure 3.5 Elliptically Illuminated Area (Beam-width Limited Case)	22
Figure 3.6 Range Resolution Interval for a Pulsed Transmitter	23
Figure 3.7 Illuminated Area Strip (Pulse-length Limited Case)	24
Figure 3.8 Standard Deviation of Clutter vs Wind Velocity	28
Figure 3.9 Decorrelation Times vs Wind Velocity at 3.6 GHz for Open-Wood Type Terrain	29

Figure 3.10 Multipath Effect at Near Grazing Incidence	31
Figure 3.11 Constant Gamma Model	31
Figure 3.12 Mathematical Clutter Model for Various Types of Terrain	32
Figure 3.13 Correction Factor for Various Velocities and Various Release Angles ($\theta_B = \phi_B = 70^\circ$)	37
Figure 3.14 Clutter Model for Wooded Hill and Desert Road	37
Figure 3.15 Correction Factor for Wooded Hill and Desert Road ($\theta_B = \phi_B = 70^\circ$)	38
Figure 3.16 Rate of Change in Correction Factor per Degree for Wooded Hill	38
Figure 4.1 Graphical User Interface for Simulating the Reflection from Flat Terrain	40
Figure 4.2 Return Power ($h_0 = 300$ m, $v_0 = 100$ m/s, and $\zeta_0 = 80^\circ$)	41
Figure 4.3 Estimation Result ($h_0 = 100$ m, $v_0 = 100$ m/s, and $\zeta_0 = 80^\circ$)	41
Figure 4.4 Corrected Estimation ($h_0 = 2000$ m, $v_0 = 200$ m/s, $\zeta_0 = 80^\circ$, and $C = 0.0269$)	42
Figure 4.5 Corrected Estimation ($h_0 = 300$ m, $v_0 = 100$ m/s, $\zeta_0 = 80^\circ$, and $C = 0.0179$)	42
Figure 4.6 Relative Error for Various Release Angles ($h_0 = 300$ m, $v_0 = 100$ m/s)	43
Figure 4.7 Relative Error for Various Release Velocities ($h_0 = 300$ m, $\zeta_0 = 90^\circ$)	43
Figure 4.8 Single Channel Proximity Sensor Tx/Rx Module	44
Figure 4.9 Sources of the Phase Noise	45
Figure 4.10 Sample Phase Noise Characteristic (Minicircuits' ROS-3600-619 VCO)	46
Figure 4.11 Distance between the Sensor and the Reflecting Surface Element	46
Figure 4.12 Doppler Spectrum Isodops	49
Figure 4.13 Signal to Noise Ratio	50
Figure 4.14 Sample Receiver Stage with Gains and Noise Figures	51
Figure 4.15 Return Signal with Phase and Thermal Noises	52
Figure 4.16 Height Estimation ($h_0 = 100$ m, $v_0 = 100$ m/s, and $\zeta_0 = 60^\circ$)	53
Figure 4.17 Height Estimation, SNR=80 dB ($h_0 = 100$ m, $v_0 = 100$ m/s, and $\zeta_0 = 60^\circ$)	54
Figure 4.18 Height Estimation, SNR=60 dB ($h_0 = 100$ m, $v_0 = 100$ m/s, and $\zeta_0 = 60^\circ$)	54
Figure 4.19 Height Estimation, SNR=80 dB, Linear Regression Duration 30 ms ($h_0 = 100$ m, $v_0 = 100$ m/s, and $\zeta_0 = 60^\circ$)	56

Figure 4.20 Height Estimation, SNR=80 dB ($h_0 = 200$ m, $v_0 = 100$ m/s, and $\zeta_0 = 60^\circ$)	57
Figure 5.1 Structure of the Double-Plane Geometry	58
Figure 5.2 Differential Clutter Element	59
Figure 5.3 Distances on xx , xz and yz Planes	60
Figure 5.4 Differential Distance, dy	61
Figure 5.5 Integral Limits for Calculating Return Power from Double-Plane Terrain	63
Figure 5.6 Intersection Regions between Plane-1 and Plane-2, (a) Sensor is in Region-1, (b) Sensor is in Region-2	63
Figure 5.7 Intersection Regions between Plane-1 and Plane-2, (a) Sensor is in Region-1 (b) Sensor is in Region-2	64
Figure 5.8 Estimation Error for a Two-Plane Terrain ($h_0 = 100$ m, $v_0 = 200$ m/s, and $\zeta_0 = 60^\circ$)	65
Figure 5.9 Off-Set Distances from the Impact Points	65
Figure 5.10 Estimation Results for Different Off-Set Distances ($h_0 = 100$ m, $v_0 = 200$ m/s, and $\zeta_0 = 60^\circ$)	66
Figure 5.11 Sample Digital Terrain Elevation Data	67
Figure 5.12 Sample Structure for a 7 Cell DTED Data	69
Figure 5.13 Sample Visibility Map Generated by MATLAB™	71
Figure 5.14 Triangulation Structure of the DTED Matrix	71
Figure 5.15 Triangulation of DTED with Two Invisible Posts	72
Figure 5.16 Surface Normals Located at Patch Centroids after Triangulation for a Sample Terrain	72
Figure 5.17 Vectors for Sensor and the Clutter Patch	73
Figure 5.18 Grazing and Bore-sight Decline Angles for a Clutter Patch	75
Figure 5.19 Graphical User Interface of Simulation which is Calculating Parameters for DTED Generated Terrain	76
Figure 5.20 Relation of Doppler Spectrum with Terrain	77
Figure 5.21 Effect of Tilt Angle on to the Received Power	77
Figure 5.22 Simulation Result for Parameters Given in Table 5.2	78

Figure 5.23 Estimation Result for Parameters Given in Table 5.2	78
Figure 5.24 Same Terrain Profile with Three Different Heights	79
Figure 5.25 Angles between the Sensor and Terrain	80
Figure 5.26 Doppler Shift Spectrum for Terrain Profiles given in Figure 5.24	80
Figure 5.27 Two Patch Geometry	81
Figure 5.28 Patch Clutter Model	82
Figure 5.29 Ratio d/h vs Grazing Angle (α_2)	83
Figure 5.30 Ratio d/h vs Patch Tilt Angle for Different Antenna Beamwidths	84
Figure 5.31 Effect of Reflectivity on Ratio (Identical Patches)	84
Figure 5.32 Effect of Reflectivity on Ratio	85

CHAPTER 1

INTRODUCTION

1.1 Radio Sensing for Proximity Fuzes

Fuze is a device that ensures safety of the munitions before and during launch that arms the munitions after launch and that detonates the munitions at a specified condition. There are many kinds of fuzes, the main functions of which are safety, arming and detonation. Detonation timing is crucial to obtain the optimum damage to the target. Some fuzes detonate after the contact with the target, whereas some detonate when approaching to the target and some detonate at a specific time delay. Remote sensing with well planned timing for burst height increases the reliability of the fuze.

A very common remote sensing type is the radio sensing and these type of fuzes are called radio proximity fuzes. The VT fuze, appearing during World War II, is the first proximity fuze, which was used to obtain a stand-off distance for artillery bombs [1, 2]. The early development of fuzes is further discussed in [3] and [4]. Acoustic and photoelectric methods were used in addition to the radio proximity fuzing. Contemporary methods now also include infra-red technology [5].

Radio proximity techniques are not only used for artillery purposes, but these techniques are also utilized in level-sensing and collision avoidance-like applications [6, 7]. Application-specific integrated circuits are also used [8]. To obtain a safe final decision the natural conclusion is that fuzes should combine more than one sensing method [9]. Nevertheless, there is a trade off between complexity and the range resolution. Very fine resolutions could, however, be obtained by utilizing wide bandwidth signals; Ultra-Wide-Band (UWB) solutions are being studied [10–13].

Infrared technology used in proximity sensing is capable of producing accurate results. However, infrared waves suffer in atmospheric conditions such as dust and smoke, both of which are likely to be present on occasions in which proximity sensing is utilized. In such cases radio waves are the remedy for getting a return signal from a target - generally a land surface, building wall or vehicle.

Modulated radio waves are commonly chosen because the signal is time stamped when it is transmitted and when it is received; the range can be calculated by the time difference on the time stamp. The higher the bandwidth of the transmit signal is, the higher the resolution of the range decision. Pulsed or frequency modulated waveforms are used in most of the ranging applications. However, for proximity sensing, pulsed waveforms are not preferable due to blind ranges during the transmission period. Use of UWB, in this sense, is an endeavour towards the use of pulsed waveforms. On the other hand, Frequency Modulated Continuous Wave (FMCW) signals do not suffer from blind ranges due to the low transmit power levels. Nevertheless, leakage, coupling or return from the antenna input terminal will crowd the low frequency spectrum, which corresponds to the spectrum of the near-range targets.

Use of unmodulated Continuous Wave (CW) is simple to implement and eliminates modulated signal problems.

1.2 General Height Estimation Techniques used in Proximity Fuzes

In the earliest applications of the proximity sensors used in the fuzes, sensor perceive the capacitive volume between the ground and the sensor antenna. The capacitance between sensor and the ground adjust the oscillator frequency of the sensor. The change in the frequency of the sensor's oscillator initiates the fuze. The later conventional proximity fuzes use radio waves to sense the proximity. In this technique wave is transmitted from the sensor and reflected back from the terrain. The sensor is functioned after the envelope of the received voltage of the reflected signal exceeds a specific threshold level which can be called "Threshold Detection" (Figure 1.1). These types of fuzes are used mainly for mortar/artillery projectiles and air-to-ground ballistic bombs. The threshold detection technique is used in many conventional applications for height estimation. However, the threshold highly depends on the clutter properties.

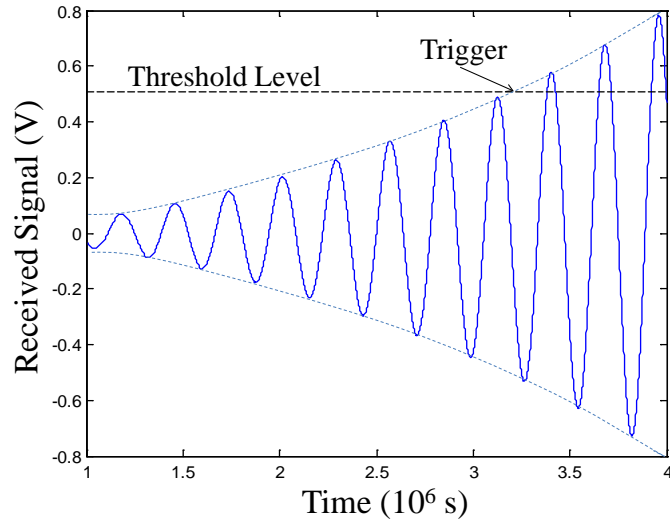


Figure 1.1: Conventional Proximity Sensor Triggering

The reflected energy levels are subject to change for different types of targets due to the different Radar Cross Sections (RCS) which leads a mismatch at the pre-selected height of detonation. Generally target is the terrain where the troops are positioned. To overcome the deviation in the distance estimation due to different reflected energy levels some techniques such as Frequency Modulated Continuous Wave (FMCW) altimeter, pulsed radar, infrared or Ultra Wide Band (UWB) sensors [14] are used for precise height measurement. Acoustic and photoelectric methods were used in addition to the radio proximity fuzing.

Both of these height measurement methods have their own disadvantages especially when the distance is decreased from a few kilometres to a few ten meters and the distance of interest in a few ten meters. There are many studies and variety of patents to overcome the specific limitations of these methods [15–19]. The limitations of FMCW technique especially at relatively short distances can be summarized by:

- Receiver saturation due to leakage of the transmitted signal through the receiver,
- Non-linearity of the chirp pulse,
- Truncation of the beat frequency due to the limited modulated bandwidth,
- Suppression due to oscillator noise when the beat frequency is closer to the oscillation frequency.

For the pulsed system, the complication of the design is a challenging issue and the clutter power reflected from the land is much more higher compared to the return pulse [20]. To avoid blind range for short distances, very short pulse duration is needed which makes the pulsed system more complicated and the required peak signal power is very high when the pulses are shorter.

In this dissertation, a height estimation method using the differential amplitude and the associated Doppler shift of the returned signal from the terrain was defined. The theory is applicable for the sensors used to determine the height of the ballistic platforms. Also this method is applicable for determining the distance between a missile and air-borne target. The main advantage of the theory is the elimination of the clutter effects.

CHAPTER 2

PROXIMITY SENSING CAPABILITIES OF FUZES

2.1 Proximity Fuzes

There are many type of remote sensing used by the fuzes to detect the target at a distance for optimum blast effect. The remote sensing types are Radio Frequency (RF), Inductive, Electrostatic, Magnetic, Electro-Optical, Millimeter Wave, Capacitive, Seismic, and Acoustic. Our interest is the sensing types used to detect the distance between the airborne munitions and the terrain. For this purpose RF sensing and Millimeter Wave sensing is primarily used. The latter is used much more lately than the RF sensing. RF sensing causes the detonation of the explosive charge in the vicinity of the target. It is useful to obtain optimum dispersion of fragments or sub munitions. Since a direct hit is not necessary net effect is that of having an enlarged target. The example of this type of influence-sensing fuze is the radio proximity type. Originally, such fuzes were called “VT” (variable time) fuzes, but the term “proximity” is now preferred.

The optimum distance is calculated according the type of explosive, approach angle to the target, type of the target and intended effect of the explosive. The fuzes used for army and air force applications initiate the munitions, in general, at 2-12 meters. However, the optimum distance is around 4 to 5 meters for airborne general purpose bombs (Figure 2.1) for maximum blast effect. JMEM (Joint Munitions Effectiveness Manual) is one of the calculation sources for the optimum burst height for proximity fuzes.

The most common operation principle of the proximity fuzes is the Threshold Detection. As the bomb approaches the target, the interaction between the emitted and reflected RF energy

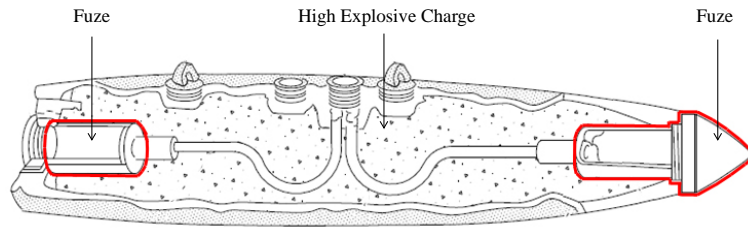


Figure 2.1: General Purpose Bomb

causes a Doppler signal in the receiver stage of the sensor. This return signal from the target is amplified sufficiently to trigger the firing circuit.

In this section, only the proximity sensors used for measuring the air to ground level of the ballistic munitions are investigated.

2.1.1 Fuzes for Army Munitions

Mortar and Artillery projectiles (Figure 2.2 and 2.3) need proximity distance both for optimum fragmentation effect as well as to achieve the stand-off distance for shaped charged munitions. The very first proximity applications used in the mortars and projectiles against the surface targets during the World War II.

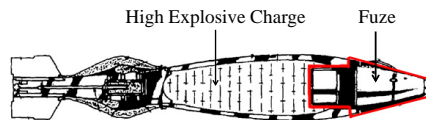


Figure 2.2: Mortar Projectile

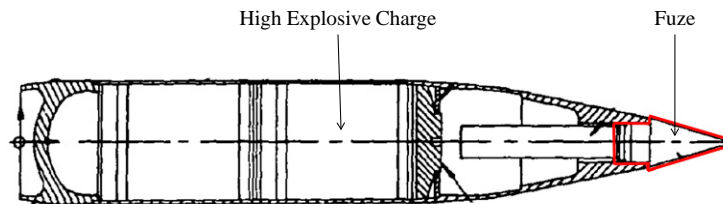


Figure 2.3: Artillery Projectile

M513 Proximity Fuze

These series of mortar fuzes have a CW Doppler sensor. The transmitted signal is returned

with a Doppler shift. When the amplitude of the Doppler shift reaches to a predetermined level, an electrical signal is generated to initiate the detonation of the explosive charge in the fuze (Threshold Detection). These fuzes are expected to detonate within 1 to 10 meters. Due to the different reflectivity characteristics of the terrain the return signal has not the same energy for every type of terrain. If the terrain has high reflectivity the Doppler signal reaches to the threshold level earlier and the detonation occurs early than expected. While the detonation is expected to occur at 1 to 10 meters it may occur at higher distances up to 16 meters. If this is the condition, a metal cap is placed over the fuze to decrease the height of burst by a factor of four. Sometimes, the low reflectivity of the terrain together with the low grazing angle causes the Doppler shift does not reach the threshold level before impact on the terrain. An impact switch is used to initiate the explosive train if the proximity sensor does not function to avoid having unexploded ammunition.

M514 Proximity Fuze

These series of fuzes have the same principle of operation (Threshold Detection). They have higher height of burst compared with the standard VT fuzes (M728 and M732). These fuzes have the same problems to determine the burst height with M513 series fuzes.

M517 and M532 Proximity Fuzes

These series of fuzes have the same principle of operation (Threshold Detection). The height of burst depends on the angle of fall, the nature of the terrain and the approach velocity. These fuzes have the same problems with M513 series fuzes to determine the burst height.

M728 Proximity Fuze

These series of fuzes have the same principle of operation (Threshold Detection). The difference of this fuze from the previous fuzes is the immunity to fall angle. Regardless of the angle of fall the burst height remains the same. But these fuzes still have the problem to correctly determine the burst height.

M766 Proximity Fuze

The M766 Proximity Fuze is used primarily against aerial targets. They have a sensitivity regulation device built-in to the electronic circuitry to adjust the triggering threshold level. The sensitivity device is set according to the clutter whether it is sea or land.

M734A1 Proximity Fuze

M734A1 fuze is one of the sophisticated fuzes used for mortars (Figure 2.4). It is the new generation fuze and the technology based on Frequency Modulated Continuous Wave (FMCW) Directional Doppler Rate Ranging (DDR) technique. This technique significantly improves the accuracy of the fuze's burst height above the ground. This fuze is designed to have a consistent burst height and it is the first example of new generation fuze with this capability. Near surface burst distance is 0 to 1 meters and proximity distance is 1 to 4.3 meters.



Figure 2.4: M734A1 Proximity Fuze (Mounted)

M782 Multi-Option Fuze for Artillery (MOFA)

M782 Multi-Option Fuze for Artillery (MOFA) is the newest generation fuze used in the artilleries (Figure 2.5). Proximity distance is 9 to 10 meters over normal terrain and the burst height accuracy is 95% regardless of the terrain and the firing conditions.



Figure 2.5: M782 Multi-Option Fuze for Artillery (MOFA)

Recent Developments in Artillery Proximity Sensing

A new state-of-the-art proximity sensor for the new generation artillery multifunction fuze is

FRAPPE. It has an FM-CW Microwave Radar Sensor and it has Full Digital Signal Processing capability [21]. The accuracy information does not exist. However, FMCW systems have problems to calculate the short distances.

Extended Range Guided Munitions (ERGM) designated as EX171 achieved 3.3 m burst height with a 0.65 m (20%) accuracy. However, this system is vulnerable to Approach Angle which is ± 10 degrees [22].

Millimeter wave systems (UWB fuzes) are also favorable due to

- Antenna Performance. Narrower bandwidths and higher attainable gain for a given aperture will reduce multipath effects.
- Electronic Countermeasures (ECM). High free space attenuation means low vulnerability to ECM and extremely low side lobe detectability.
- Fog, Cloud, Rain, and Snow Immunity. Low-loss atmospheric propagation characteristics of millimeter waves enhance immunity to obscurants.
- Size and Weight. Components scale with wavelength, thus reducing packaging volume and weight.

But the main disadvantage of the UWB systems is the immaturity.

2.1.2 Fuzes for Airborne Ballistic Munitions

For the modern jet fighter the variety of the proximity fuzes are limited. External Store Certification Process is a challenging and costly task. Thus, the aircraft manufacturers certify a limited number of the fuzes. F-16 Aircraft proximity fuzes will be introduced. There are two types of proximity fuzes used for air-drop munitions. One is the cluster type fuze and the other is pre-frag type of fuze. Pre-frag bombs have metal balls inside the explosive and for maximum effect the bombs must be detonated at an optimum height above the ground.

FMU-56 B/B and D/B Fuzes

These series of fuzes are designed to dispense sub-munitions over a wide area by functioning between 100 to 1000 meters. The accuracy is $\pm 10\%$. The operation principle of these dispenser type fuzes is FMCW.

FMU-110/B Fuze

Similar to FMU-56 fuze, FMU-110/B fuze is used for dispenser munitions. The burst height is 80 to 1000 meters. The accuracy is ± 16 meters at 235 meters.

FMU-56 and FMU-110 series fuzes are both utilize FMCW Radar Altimeter to measure the distance to ground. They are used for the dispenser munitions. Other types of fuzes which are used for airborne ballistic platforms are the proximity fuzes. They are designed to detect the distances shorter than 15 meters. For airborne platforms fuze and the proximity sensor is utilized separately as shown in the Figure 2.6.

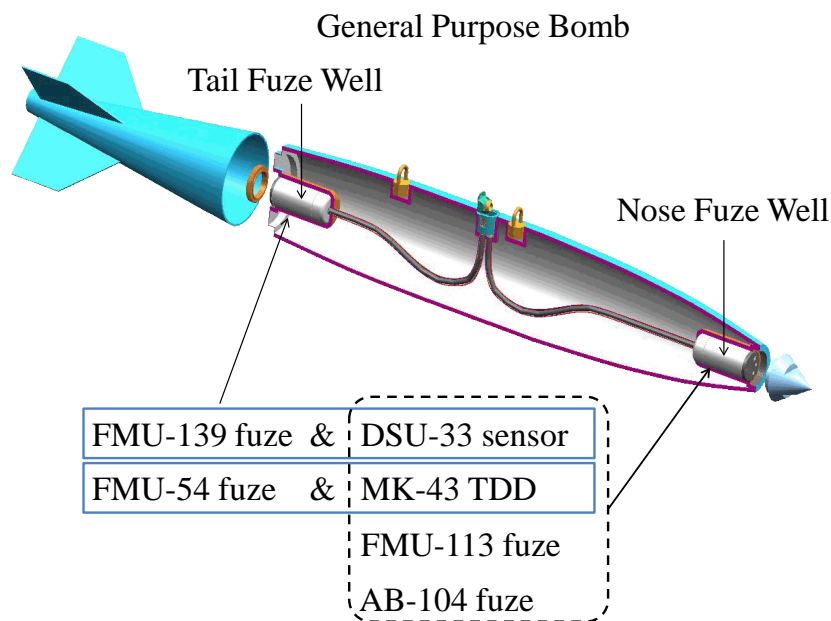


Figure 2.6: Proximity Fuze Configurations for General Purpose Bombs

MK 43 MOD 1 Target Detecting Device(TDD)

MK 43 MOD 1 Target Detecting Device (TDD) is a proximity nose element that gives airburst capability to general purpose bomb fuzes. It is used with FMU-54 A/B impact tail fuze. The form factor is same of a general purpose bomb fuze to be mountable to the fuze well (Figure 2.7). The nominal burst height is 5.3 meters.

DSU-33 A/B, B/B Proximity Sensor

DSU-33 is a proximity sensor used together with FMU-139 series fuzes when the FMU-139 is mounted into the tail fuze well of the bomb. DSU-33 is the most common proximity sensor

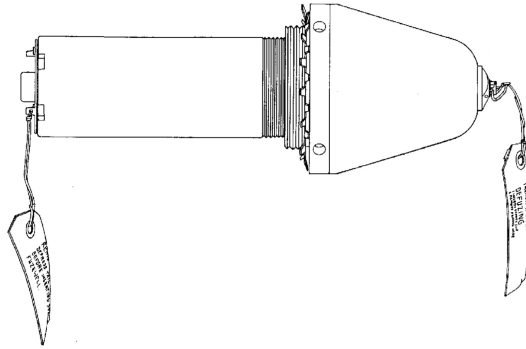


Figure 2.7: MK 43 MOD 1 Target Detecting Device

used for general purpose bombs. The nominal burst height is 6.7 meters with a tolerance of ± 2 meters.

FMU-113/B Proximity Fuze

Unlike the MK43 MOD1 TDD and DSU-33 Proximity Sensor this is a complete fuze used with general purpose bombs with proximity sensing capability. The nominal burst height is 5 meters, however, the burst height varies between 0 to 8.3 meters.

AB-104 Proximity Fuze

AB-104 fuzes are like FMU-113 fuzes and their burst height is between 2 to 12 meters.

MK-43 MOD1 Target Detecting Device and DSU-33 Proximity Sensor together with FMU-113/B and AB-104 fuzes have the same conventional operation principle “Threshold Detection”.

Recent Developments in Proximity Sensing for Airborne Ballistic Munitions

High Accuracy Radar Proximity Sensor (HARPS) [23] is as an updated design to compete with the DSU-33 sensor and based on M734A1 fuze technology (Figure 2.8).

This fuze has a burst height 5 ± 1 meters over target surfaces which reflectivity ranges +5 to -16 dB as:

- Soil (Wet and Dry)
- Concrete (Wet and Dry)
- Water



Figure 2.8: High Accuracy Radar Proximity Sensor (HARPS)

- Dense Foliage
- Desert Scrub

with Approach Velocity from 30 to 500 m/s and with Approach Angles from 15° to 90° from horizontal. The burst height is given in Figure 2.9.

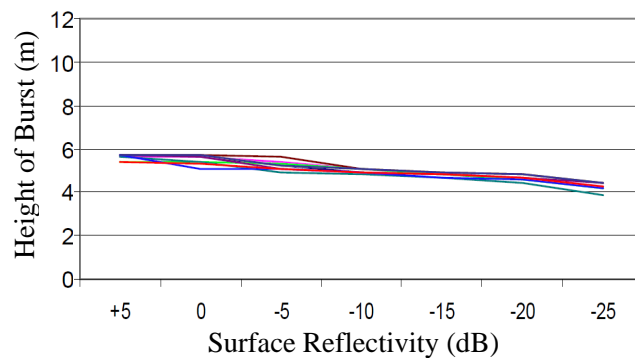


Figure 2.9: Burst Height of HARPS

DSU-33 A/B and B/B sensors are also upgraded as DSU-33 C/B (Figure 2.10) to improve HOB accuracy, as well as to reduce labor and production costs. DSU-33 A/B and B/B sensors have a burst height accuracy of ± 2 meters in theoretical. This accuracy has a reliability less than 80%. The accuracy of the sensor is ± 5 meters when the reliability is 80%. When having a reliability of 100%, the range of the burst height is measured as 0 to 16.7 meters [24]. This statistical data show that the DSU-33 sensors may actuate a firing signal between 0 to 16.7 meters.



Figure 2.10: DSU-33 C/B Proximity Sensor

2.1.3 Proximity Capabilities of Proximity Sensors/Fuzes

The lethal range of the fragmented munitions are affected by the proximity distance. The proximity distances of some sensors and fuzes are given in Table 2.1.

Table 2.1: Proximity Fuzes

FUZE TYPE	USED IN	BURST HEIGHT (HOB)	COMMENT
M513, M513B	Mortar	1 - 10 m	HOB>17 m observed
M513A1, A2	Mortar + Artillery	1-10 m	HOB>17 m observed
M514A3	Artillery	>10 m	Threshold Detection
M517	Mortar	1-10 m	Threshold Detection
M532	Mortar	1-10 m	Angle of Fall Immunity
M728	Mortar + Artillery	1-10 m	Angle of Fall Immunity
M766	Air Defence	-	Terrain Selection (Land or Sea)
M734A1	Mortar	0-1 m, 1-4.3 m	FCW-DDR
M728 (MOFA)	Artillery	9-10 m	HOB Accuracy: 95%
FMU-56B/B, D/B	Cluster Bombs	80-1000 m	FMCW
FMU-110/B	Cluster Bombs	100-1000 m	FMCW
MK 43 MOD 1	GP Bombs	5.3 m	Nominal
DSU-33A/B, B/B	GP Bombs	6.7 ±2 m	Varies 0-16.7 m
FMU-113/B	GP Bombs	5 m	Varies 0-8.3 m
AB-104	GP Bombs	2-12 m	Threshold Detection
HARPS	GP Bombs	5±1 m	FMCW-DDR

Proximity fuzes and sensors used for mortar, artillery and general purpose bombs need much more precise height estimation methods. The constraints to design a height estimation method are:

- Low-cost. When the production quantities are taken into account, the sensor solution must be a low cost solution.
- Simplicity. The fuzing system must be as simple as possible to achieve high reliability required for the munition systems. For some application the available physical space for implementing the fuze sensor is very small, thus a simple solution generally requires less space compared to complicated systems.
- Accuracy. High accuracy is the basic operational requirement for proximity sensing. The effectiveness of the shape-charged munitions used for target penetration, air-defence munitions and anti-personnel fragmented bombs are all highly depended on the precise stand-off distance.

FMCW-DDR and UWB systems reaches to the desired accuracy but the method described within the dissertation promotes a more simpler and low-cost solution compared to FMCW-DDR and UWB systems.

CHAPTER 3

HEIGHT ESTIMATION USING DIFFERENTIAL AMPLITUDE MEASUREMENTS

3.1 Theory of the Height Estimation Method

This study focused on the sensors mounted on ballistic platform (like general purpose bombs and mortar/artillery shells without any propulsion or guidance) to obtain a simple and convenient sensor solution. The target was assumed to be the terrain throughout the thesis. This method can be applied to missile warheads for determining the distance of the missile to airborne targets. The main problem for the current sensors used on the ballistic platforms is the change of the land reflectivity (land clutter). The energy level of a reflected wave from the ground is subject to change for different types of terrain due to the different Land Reflectivity. The various reflection behaviours of the terrain leads a mismatch at the pre-selected height of burst for munitions. Therefore the time and space variation behaviour of the land reflectivity plays an important role in the height estimation technique. The initial assumptions were:

- The region of interest for height estimation is the distance where the ballistic platform (whenever it is an ammunition) is most effective. While the estimation start from a few kilometres down to a few ten meters, reliability of the estimation is important at the proximity distance which is a few ten meters.
- While the distance is a few ten meters, due to the axial high velocity of the platform and the high grazing angle (which is generally between 30° - 70° in real conditions for air drop ballistic munitions), the spatial variation of the clutter can be disregarded in many cases.

- Decorrelation of the reflected signal due to the temporal variation of the clutter (which have been calculated in Section 3.1.1.3) is assumed to be slower than estimation speed.

The total received power reflected back from the target at the sensor with continues wave (CW) transmission was calculated by the radar equation (3.1). (P_0) is the transmitted signal power, (G_0) is the gain of the system, (λ) is the wavelength, (σ) is the target RCS, (F) is the pattern-propagation factor and (r) is the distance from sensor to the target.

$$P_r = \frac{P_0 G_0^2 \lambda^2 \sigma F^4}{(4\pi)^3 r^4} \quad (3.1)$$

The energy level of the reflected power from different regions with different clutter properties is related to:

- Forth power of the inverse of the distance (r),
- Change in the land reflectivity (σ),
- Forth power of the Pattern-Propagation Factor (F)

the other factors such as transmitted power (P_0), gain of the system (G_0), and wavelength (λ) remains the same during the trajectory of the sensor.

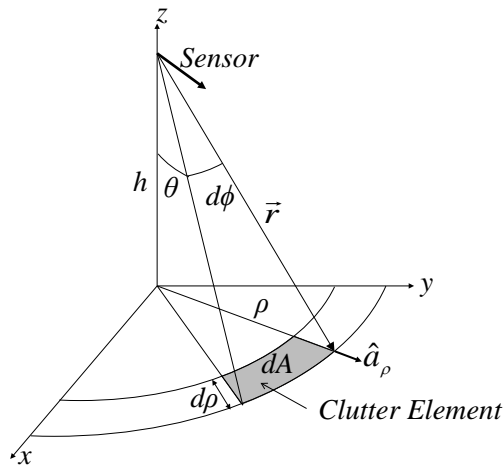


Figure 3.1: Clutter Element in Spherical Coordinate System

The sensor and the relative position of the sensor over the flat terrain is given in Figure 3.1 and Figure 3.2. The received power (dP_r) reflected back from an infinitesimally small area

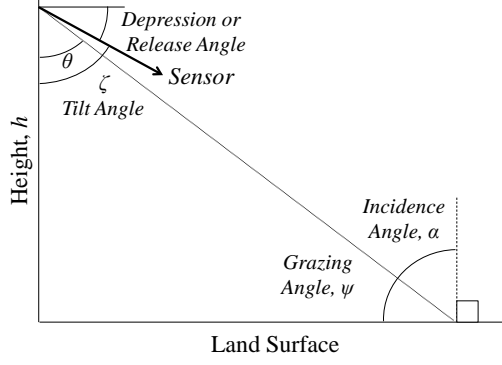


Figure 3.2: Angle Definitions

(dA) equal to:

$$dP_r = \frac{P_0 G_0^2 \lambda^2 F^4(\theta, \phi, \zeta) \sigma_0(\theta) dA}{(4\pi)^3 r^4} \quad (3.2)$$

where $\sigma_0(\theta)$ is the normalized cross section (details are given in Section 3.1.1). Normalized cross section times the clutter area accounts for the radar cross section of the terrain. Radar cross section σ is the reflectivity of the terrain. The transmission line loss, atmospheric attenuation and noise did not included for the calculation of the reflected power (3.1). F is the pattern-propagation factor [25, p.378] which accounts for the polarization and antenna radiation pattern effects. Pattern-propagation factor is the ratio of actual field strength at a point to the field strength if the propagation was in free-space. In the calculations only the antenna field pattern was included for the propagation factor (F). The height of interest is higher than the linear dimension of the antenna which satisfies the far-field assumption.

$$F = f_A(\theta, \phi, \zeta) = \exp\left(-2 \ln(2) \left(\frac{\theta - \zeta}{\theta_B}\right)^2\right) \cdot \exp\left(-2 \ln(2) \left(\frac{\phi}{\phi_B}\right)^2\right) \quad (3.3)$$

If we assume the land reflectivity σ_0 and the tilt angle of the sensor ζ remains unchanged during the estimation period, the derivative of the received power will be related to change of height. With this fact the radar range equation (3.1) was modified to estimate the height.

Using the definitions in Figure 3.3 infinitesimally small area dA is equal to

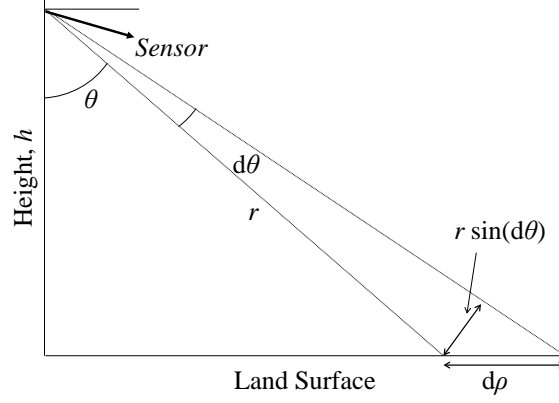


Figure 3.3: Length of the Differential Area, $d\rho$

$$dA = r d\phi d\rho = r d\phi \frac{r d\theta}{\cos(\theta)} \quad (3.4)$$

then substituting the distance (r) with the height of the sensor (h) the equation for received power (3.2) is:

$$dP_r = \frac{P_0 G_0^2 \lambda^2}{(4\pi)^3 \frac{h^4}{\cos^4(\theta)}} \frac{h^2}{\cos^3(\theta)} f_A^4(\theta, \phi, \zeta) \sigma_0(\theta) d\theta d\phi \quad (3.5)$$

$$dP_r = \frac{P_0 G_0^2 \lambda^2}{(4\pi)^3} \frac{\cos(\theta)}{h^2} f_A^4(\theta, \phi, \zeta) \sigma_0(\theta) d\theta d\phi \quad (3.6)$$

Integrating (3.6) over the elevation beam-width (θ_B) and azimuth beam-width (ϕ_B) we get the total received power (P_r) reflected back from the area illuminated by the antenna.

$$P_r = \frac{P_0 G_0^2 \lambda^2}{(4\pi)^3 h^2} \int_{\theta=\zeta-\theta_B/2}^{\zeta+\theta_B/2} \int_{\phi=-\phi_B/2}^{\phi_B/2} f_A^4(\theta, \phi, \zeta) \sigma_0(\theta) \cos(\theta) d\theta d\phi \quad (3.7)$$

$$K = \frac{P_0 G_0^2 \lambda^2}{(4\pi)^3} \quad (3.8)$$

$$I = I(\theta, \phi, \zeta) = \int_{\theta=\zeta-\theta_B/2}^{\zeta+\theta_B/2} \cos(\theta) \sigma_0(\theta) \int_{\phi=-\phi_B/2}^{\phi_B/2} f_A^4(\theta, \phi, \zeta) d\theta d\phi \quad (3.9)$$

$$P_r = \frac{K.I}{h^2} \quad (3.10)$$

$$V_r = \sqrt{2 Z_0 P_r} \quad V_r = \frac{\sqrt{2 Z_0 K I}}{h} \quad (3.11)$$

where Z_0 is the characteristic impedance. Time derivative of the received voltage that we can measure in the sensor results (3.12). To elicit the height (h) information measuring of the time derivative of the height is needed. The time derivative of the height is the vertical velocity (v_z) which is the z -axis component of the velocity vector (v_0) of the sensor.

$$\frac{dV_r}{dt} = \sqrt{2 Z_0 K} \left(\underbrace{\frac{1}{h} \frac{d\sqrt{I}}{dt}}_{zero} + \sqrt{I} \frac{d}{dt} \left(\frac{1}{h} \right) \right) = -\frac{\sqrt{2 Z_0 K I}}{h^2} \frac{dh}{dt} \quad (3.12)$$

It was assumed that integral I (3.9) is constant through the final phase of the sensor. The constant term of (3.12) $\sqrt{2 Z_0 K I}$ cancels by dividing (3.12) to (3.11).

$$\frac{dV_r}{dt} \frac{1}{V_r} = -\frac{\sqrt{2 Z_0 K I}}{h^2} \frac{dh}{dt} \frac{h}{\sqrt{2 Z_0 K I}} = -\frac{1}{h} \frac{dh}{dt} \quad (3.13)$$

$$h = -V_r \left(\frac{dV_r}{dt} \right)^{-1} \frac{dh}{dt} \quad (3.14)$$

The negative rate of change of the height (dh/dt) of the sensor is the vertical velocity v_z .

$$h = \left(\frac{dV_r}{dt} \right)^{-1} V_r v_z \quad (3.15)$$

Vertical velocity was measured from the Doppler frequency ($f_{Doppler}$). The relation between the Doppler frequency and the vertical velocity (v_z) of the sensor is:

$$f_{Doppler} = \frac{2 v_0 \cos(\zeta)}{\lambda} \quad v_z = v_0 \cos(\zeta) = -\frac{dh}{dt} \quad (3.16)$$

where v_0 is the axial velocity of the sensor and λ is the wavelength of the signal. With the information of the time derivative of the received voltage and Doppler frequency shift the height of the sensor was estimated (3.17).

$$h = V_r \left(\frac{dV_r}{dt} \right)^{-1} \frac{f_{Doppler} \lambda}{2} \quad (3.17)$$

In the integral equation (3.9), σ_0 was assumed to be constant due to the assumption that the temporal change of σ_0 (within the estimation period of height) and the change in the tilt angle ζ can be neglected. If the initial axial velocity of the sensor is high and the initial tilt angle ζ is small than the rate of change of ζ with respect to time is negligible. It was observed in simulation results (Chapter 4) that the effect of the variations of the integral with respect to time is negatively effective upon the height estimation. A correction factor was needed to account for the temporal variations of the integral. The calculation of the correction factor is given in Section (3.1.2). The units are as follows:

$$P_0, P_r = dBm,$$

$$G_0, F = dB,$$

$$\lambda, r = m,$$

$$\sigma_0 = m^{-2},$$

$$A = m^2$$

Unless specified, in the calculations gain of the antenna $G_0 = 7.5$ dB, signal frequency $f_0 = 3.6$ MHz, and the beamwidths on elevation and azimuth planes $\theta_B = \phi_B = 70^\circ$.

Doppler spectrum was measured by determining the spectrum of the reflected voltage. The spectrum of the Doppler signal will be maximum for the reflections from the terrain closest to the sensor. A sample power spectrum density (PSD) of the Doppler shift is given in Figure 3.4.

3.1.1 Land Clutter and Normalized Cross Section

The theory rely on the fact that the reflectivity (clutter) of the terrain will remain same during the estimation calculation at a moment in time. The land clutter is the Radar Cross Section (RCS) of the land.

3.1.1.1 Radar Cross Section

When an electromagnetic wave impinges upon a target, the energy reflects back or the target act as an radiating antenna [26]. The reflected energy is scattered isotropically from the radiating element and produce an echo at the receiver of the radar which is equal to the absorbed

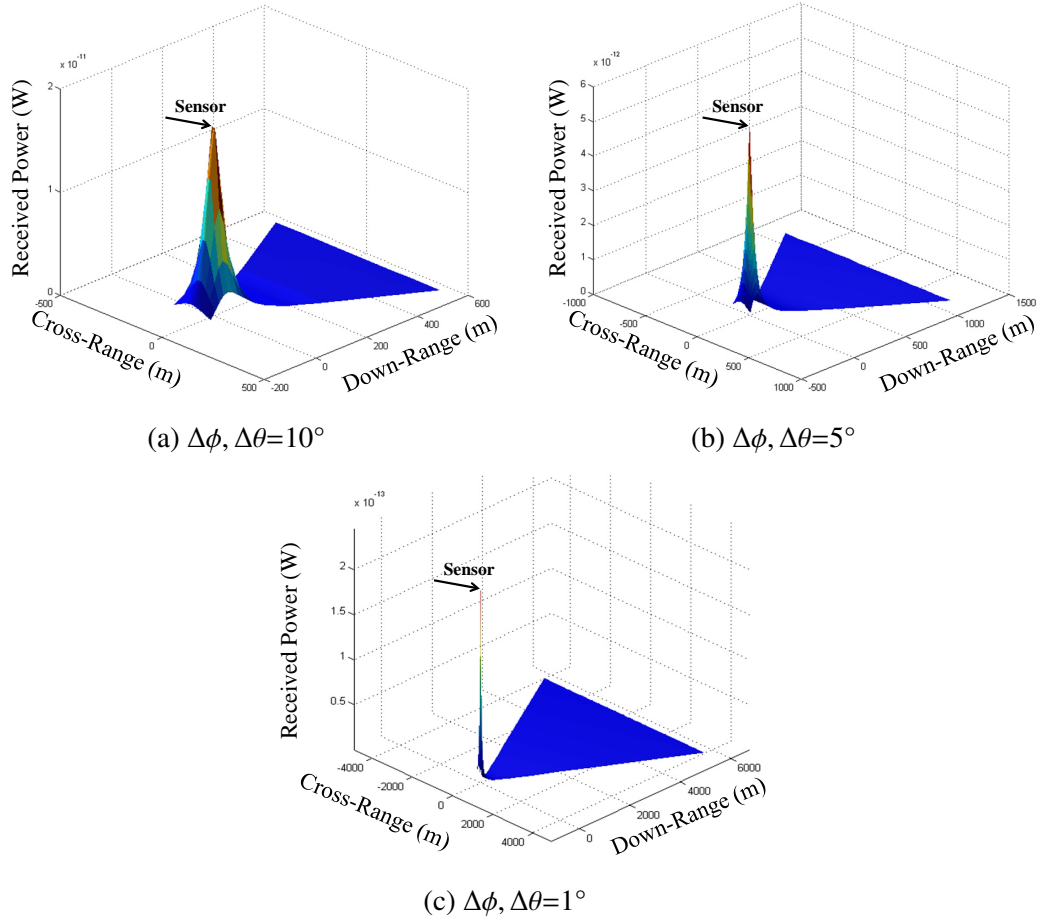


Figure 3.4: PSD of Doppler Shift ($h_0 = 100$ m and $\zeta = 60^\circ$)

power by the frictional area of target. This area is called Radar Cross Section (RCS) [27]. Radar Cross Section (RCS) denoted as σ is sensitive to orientation and wavelength. The cross section is equal to the projected area if the target scatters isotropically, i.e. the cross section of a sphere is equal to the projected area $\sigma = \pi a^2$ where a is the radius of sphere (metal lossless) when $a > \lambda$ where λ is the wavelength of the signal illuminating the target. If the radius of the sphere is small with respect to λ then the RCS will vary with λ^4 . The fourth dependence is known as Rayleigh Law. Resonance phenomenon occurs when the linear dimensions of the target is of the same order of wavelength. This is a highly sensitive and oscillating condition. If the target scatters towards the radar then σ will be larger than its projected area. Each element on the target re-radiates so the separate radiations adds up. While calculating the reflection from a ground the each clutter element acts as a separate radiator. To find the total received power from the terrain the differential power returns from each clutter element are summed up by integrating over the beam-widths of the antenna which illuminates the ground. For a flat sheet of metal with area A , if the radar beam propagating normal to the

sheet $\sigma = 4\pi A^2/\lambda^2$. RCS is a function of angle of incidence and it varies rapidly if λ is small compared to the linear dimensions of object. The average $\bar{\sigma}$ for the plate for small angles γ (excluding main lobe) is $\bar{\sigma} \cong 4\pi\lambda^2/(2\pi\gamma)^4$. Man made targets are generally have larger echoes compared to the echoes coming from the ground, which is also known as ground clutter. Ground clutter is also dependent to the wavelength but there is no exact explained mathematical model for the clutter behaviour.

3.1.1.2 Normalized RCS

Helbert Goldstein (1950) introduced the normalized RCS, σ_0 , radar cross section per unit area of surface. Then the radar cross section σ is equal to $\sigma_0 A$ where A is the area of the smooth surface of land or sea. Smooth surface is the mean for land and sea. When dealing with A the range resolution of the radar must be considered for pulsed radar applications for determining the illuminated area within one pulse duration. Our study is based on CW transmission thus no consideration for pulse was necessary. The area A was calculated by taking the integral of dP_r (3.7) over the antenna beam-widths that accounts for the area covered by the antenna beam illumination. The total illuminated area can be calculated easily by considering the illuminated area as an ellipse (Figure 3.5). The area of the ellipse is equal to (3.19). The total radar cross section of the terrain is calculated by multiplying the area A and the normalized cross section σ_0 .

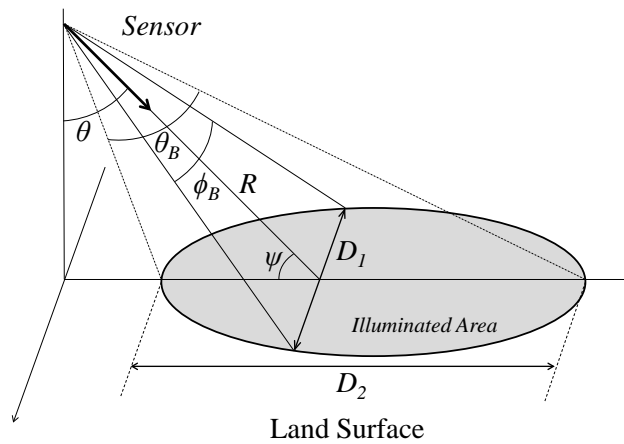


Figure 3.5: Elliptically Illuminated Area (Beam-width Limited Case)

$$D_1 = 2R \tan\left(\frac{\theta_B}{2}\right) \quad D_2 = 2R \tan\left(\frac{\phi_B}{2}\right) \csc(\psi) \quad (3.18)$$

$$A = \frac{\pi}{4} D_1 D_2 = \pi R^2 \tan\left(\frac{\theta_B}{2}\right) \tan\left(\frac{\phi_B}{2}\right) \csc(\psi) \quad (3.19)$$

This case is the beam-width limited case. θ_B is the half power beam-width in elevation plane and ϕ_B is the half power beam-width in azimuth plane. θ_B and ϕ_B are generally taken as the two way half power beam-widths as they are approximately 0.71 times the normal beam-widths [26, p.75]. If the range resolution interval is less than D_2 the illuminated area will be less than the beam-width limited case due to the range resolution interval (Figure 3.6). This condition is most likely to occur for pulsed Doppler sensors especially when the pulse duration is relatively short. In this case the radar cross section of the terrain will be $\sigma_0 A^*$ where A^* is the illuminated area by the pulse (Figure 3.7).

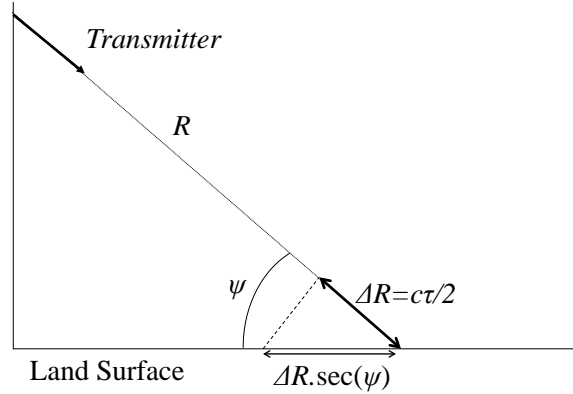


Figure 3.6: Range Resolution Interval for a Pulsed Transmitter

Illuminated area by the pulse (A^*) is calculated by (3.21).

$$D_1 = 2R \tan\left(\frac{\theta_B}{2}\right) \quad D_2^* = \Delta R \sec(\psi) = \frac{c\tau}{2} \sec(\psi) \quad (3.20)$$

$$A^* = D_1 \cdot D_2^* = 2R \frac{c\tau}{2} \tan\left(\frac{\theta_B}{2}\right) \sec(\psi) \quad (3.21)$$

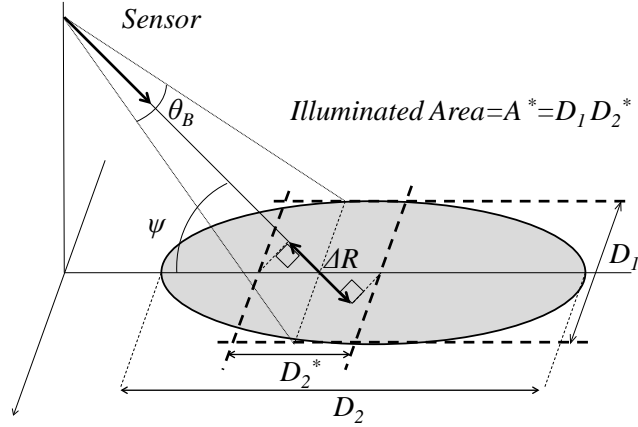


Figure 3.7: Illuminated Area Strip (Pulse-length Limited Case)

The length of the pulse or the beam-width is the key for determining whether the case is beam or pulse limited:

- $D_2 < \Delta R \sec(\psi)$ is the condition for beam-width limited case,
- $D_2 > \Delta R \sec(\psi)$ is the condition for pulse-length limited case.

then **beam-width limited case** is:

$$\frac{2R \tan\left(\frac{\theta_B}{2}\right)}{\frac{c\tau}{2}} < \tan(\psi) \quad (3.22)$$

and **pulse-length limited case** is:

$$\frac{2R \tan\left(\frac{\theta_B}{2}\right)}{\frac{c\tau}{2}} > \tan(\psi) \quad (3.23)$$

These cases for calculating the reflecting area are rough approximations while integrating differential area (dA) yields finer results. In the simulations while the total reflecting terrain was divided into small clutter elements therefore from each patch we have calculated the Doppler frequency and power (Section 5.2).

3.1.1.3 Fluctuation Statistics for Clutter Modelling

Autocorrelation Function and Power Density Spectrum The echo from one type of surface will vary if the target (target is the terrain in our study) orientation or sensor transmitter frequency changed. If the target consist of large numbers of simple targets which are in relative motion the echo will fluctuate in a noise like manner. The fluctuation spectrum will be a composition of the spectra of individual scatterers and the spectra of the group or ensemble of scatterers [26, Chapter 3] [28, Chapter 13].

Rate of this fluctuation can be described by the power density spectrum and by the time autocorrelation function. Autocorrelation function (otherwise specified autocorrelation function is the temporal correlation) $R(\tau)$ of temporally homogeneous function $X(t)$ is defined as:

$$R(\tau) = \lim_{T \rightarrow \infty} \frac{1}{2T} \int_{-\infty}^{\infty} X(t) X(t + \tau) dt \quad (3.24)$$

The power density spectrum is:

$$P(f) = \lim_{T \rightarrow \infty} \frac{1}{2T} \left[\int_{-T}^T X(t) e^{-j2\pi ft} dt \right]^2 \quad (3.25)$$

$P(f)$ is the Fourier Transform of the correlation function

$$P(f) = \int_{-\infty}^{\infty} R(\tau) e^{-j2\pi f\tau} d\tau \quad (3.26)$$

$$R(\tau) = \int_{-\infty}^{\infty} P(f) e^{j2\pi f\tau} df \quad (3.27)$$

The total power combined in the spectrum is

$$R(0) = \int_{-\infty}^{\infty} P(f) df \quad (3.28)$$

Correlation function and the corresponding power spectra contain the same information in

different forms. The Fourier transform of the Gaussian function is also Gaussian and as an example:

$$R(\tau) = e^{-\alpha^2 \tau^2} \Rightarrow P(f) = \frac{2\sqrt{\pi}}{\alpha} e^{-\pi^2 f^2 / \alpha^2} \quad (3.29)$$

Fluctuation Statistic Land clutter is a random process so the probability statistics is a mean to model it. The data available for the clutter is matched to the random probability functions of the some kind. The ratio of occurrence of an event to the number of identical experiments is called the probability of that event. While $p(x)$ is the probability density function which is equal or greater than zero. The probability that x is between all values of x is:

$$\int_{-\infty}^{\infty} p(x) dx = 1 \quad (3.30)$$

The average or mean value of a random variable x is:

$$\bar{x} = \int_{-\infty}^{\infty} x p(x) dx \quad (3.31)$$

The best known distribution is the Gaussian or normal distribution (3.32). σ is the *standard deviation* and a is the *median*.

$$p(x) = \frac{1}{\sigma\sqrt{2\pi}} \exp\left[-\frac{(x-a)^2}{2\sigma^2}\right] \quad (3.32)$$

Common Distributions The most common probability density distributions to express the land clutter properties are Rayleigh, Ricean (Rayleigh plus a constant) and log-normal distributions. If there are many positionally independent scatterers and the average intensity is constant in time, the probability of echo power P is being between a level P and $P + dP$ is given by Rayleigh Distribution (3.33). This is valid for the large number of independent scatterers. \bar{P} is the average power.

$$W(P) dP = \frac{1}{\bar{P}} e^{-P/\bar{P}} dP \quad (3.33)$$

$$\bar{P} = \int_0^{\infty} P W(P) dP \quad (3.34)$$

The probability of the received echo power is being less or greater than a value ($Pr\{P_1 < P < P_2\}$) for the half of the time called the *median* (P_m). The most probable value is called *mode* and for the Rayleigh distribution mode is zero.

$$Pr\{0 < P < P_m\} = \int_0^{P_m} W(P) dP = 0.5 \quad (3.35)$$

If a random component and a constant component exist in the echo the peak power of the distribution is shifted so do mode. This distribution is called Ricean (Rice, 1944).

$$W(P) dP = (1 + m^2) e^{-m^2} e^{-P(1+m^2/\bar{P})} J_0\left(2\text{im} \sqrt{1 + m^2} \sqrt{P/\bar{P}}\right) dP/\bar{P} \quad (3.36)$$

The probability density function for the log-normal distribution can be obtained from normal distribution by the transformation $X = \ln Y$.

$$W(Y) = \frac{1}{Y\sigma_0 \sqrt{2\pi}} \exp\left[-\frac{1}{2\sigma^2} \left(\ln \frac{Y}{Y_m}\right)^2\right] \quad (3.37)$$

Decorrelation Time for the Land Clutter Temporal correlation function specifies to what degree the value of the time function $f(t)$ at one time is correlated with another value τ time units later [26, p.79]. The autocorrelation function $R(\tau)$ is

$$R(\tau) = \lim_{T \rightarrow \infty} \frac{1}{2T} \int_{-T}^T f(t) f(t - \tau) dt \quad (3.38)$$

There are three types of correlation functions. One is the temporal, the other is the frequency (which replaces τ with frequency parameter f), and the last one is spatial (which replaces τ with spatial parameters). The time required for independence of the samples taken from a return with clutter is given by [26, p.79]

$$T_I = \frac{\lambda}{2\sqrt{2\pi}\sigma_v} \quad (3.39)$$

where σ_v is the standard deviation in m/s and T_I is in seconds. σ_v is in velocity rather than frequency for the easy of investigating the different frequencies. $\sigma_v = 0.42 \Delta V$ is in velocity units where ΔV is the half power width for a standard Gaussian shaped spectrum. Spectrum width for land clutter is given in Figure (3.8).

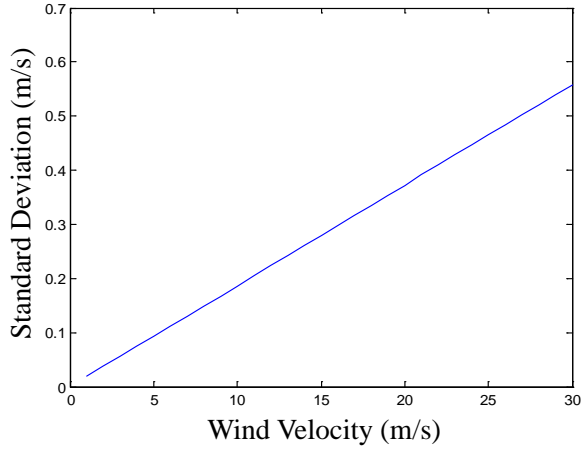


Figure 3.8: Standard Deviation of Clutter vs Wind Velocity

Table 3.1: Decorrelation Time at 3.6 GHz for Open-Wood Type Terrain

Wind Velocity (m/s)	1	4	10	15	20	25	30
Decorrelation Time, T_I (sec)	1.6	0.223	0.089	0.059	0.045	0.036	0.029

Values of the decorrelation time for the land clutter was measured (Table 3.1) and they were found to be similar with the experimental results of N. R. Narayanan, *et al* [29]. They stated that at the wind velocities of 7 to 9 m/s decorrelation time was 40-60 milliseconds at X-band (8-12.4 GHz) at their experiments. We calculated that for a 8 m/s wind velocity, the decorrelation time was 112 milliseconds at 3.6 GHz transmitting frequency (Figure 3.9). For X-band the decorrelation time was been calculated as 32.5 milliseconds and 50 milliseconds respectively for 12.4 GHz and 8 GHz. The estimation period for a specific spot at a time must be less than the decorrelation time to have better results. For 3.6 GHz decorrelation time decreased from 1.6 seconds to 29 milliseconds. In practical application all calculation for estimating the height must be finished before 30 milliseconds to preserve the correlation

of the clutter.

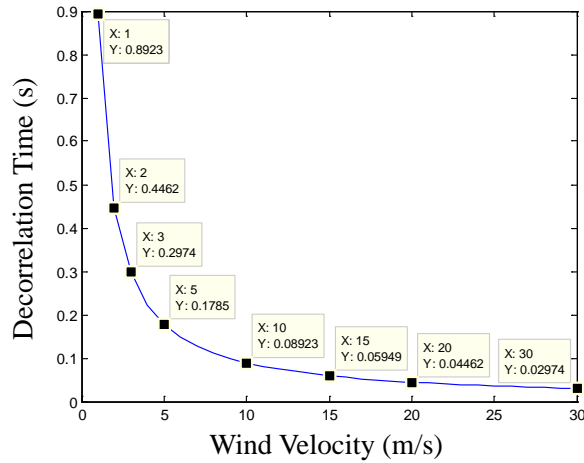


Figure 3.9: Decorrelation Times vs Wind Velocity at 3.6 GHz for Open-Wood Type Terrain

3.1.1.4 Mathematical Clutter Model

Clutter (land reflectivity) is a random variable and there is not a direct formulation or mathematical model. The value of the clutter usually observed experimentally by various laboratories and studies [27], [26, p.314-324], [30], [31]. Some of the measured clutter [26, p.273] data for different type of terrain is given in Table 3.2.

Table 3.2: Measured Clutter Data for Grazing Angles between 20° to 70°

Terrain Type	Average	UHF		L		S		X		Ku	
	γ_m	γ_m	γ_{max}	γ_m	γ_{max}	γ_m	γ_{max}	γ_m	γ_{max}	γ_m	γ_{max}
Desert Road	25	37	30	32	28	28	22	23	10	23	17
Cultivated Land	22	32	18	-	-	-	10	18	10	19	10
Open Woods	16	22	12	15	8	17	10	15	10	15	8
Wooded Hill	15	16	-	-	-	-	-	13	6	15	8
Cities	11	6	-2	11	4	15	5	12	3	-	-

All values are in dB m^2/m^2 and negative.

For land clutter the experimental data is valid for a wide range of frequencies because land clutter is depended to the frequency of the reflecting signal. While the land clutter data is expressed by σ_0 (radar reflectivity or radar cross section per unit area) sometimes a param-

eter γ which is equal to $\sigma_0 / \sin(\psi)$ is used. Average RCS is commonly used to describe the strength of the land clutter echo. Another used parameter is the *median cross section*, σ_0 . Echo strength from terrain fluctuates over a wide range, thus σ_m is easier to measure which is the half of the time the strength is exceeded that value. G.R.Valenzuela and M.B.Laing (1971,1972) studied the many statistical echoes of land and sea and concluded that the echo distributions lie somewhere between Rayleigh and Log-normal distributions [30].

Dependence of σ_0 on incidence angle is divided into three region. First is the Near Grazing Incidence, second is the Plateau Region and the third is the Near Vertical Incidence. In the near grazing there is a rapid change in $\sigma_{0,dB}$ which is the result of the interference formed by the multipath effect (Figure 3.10). In the measurement of σ_0 due to the multipath effect around near grazing incidence, path propagation factor (F) is included.

$$F = 1 + \rho e^{-j\beta\Delta R} e^{-j\phi} \quad (3.40)$$

ρ is the reflection coefficient for the multipath effect. While the wave propagates in the free space reflection coefficient is zero. Each power is proportional to F^4 therefore forward scattering from the terrain significantly effects the cross section of the targets. At higher frequencies such as X-band averaged results approaches to the σ_0 rather than $\sigma_0 F^4$. Multipath effects are less significant for the frequencies above L-band. For multipath effect to be observed surface must be smooth such as

$$h_e \cdot \sin(\psi_c) = \frac{\lambda}{4\pi} \quad (3.41)$$

where h_e is the equivalent surface roughness.

In the Plateau Region the change in the σ_0 is relatively small compared to the changes in the grazing angle (ψ). The change in σ_0 can be approximated by a $\sin(\psi)$ dependence. By assigning a constant $\gamma = \sigma_0 / \sin(\psi)$ the variations due to $\sin(\psi)$ can be neglected. In the near vertical incidence, the measured values of the σ_0 depends to the beam-width of the antenna and it is quite large.

A mathematical model was constructed using the collected data for the grazing angle and the frequency dependence of the land clutter (Figure 3.2). Grazing angle is the angle between the

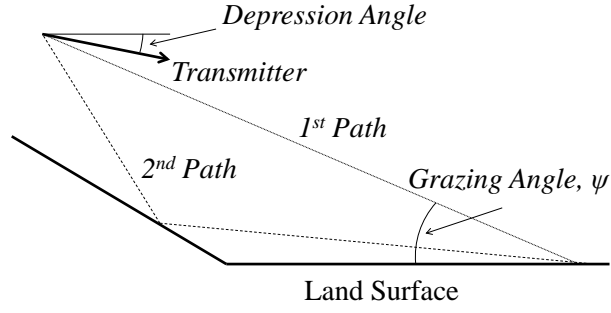


Figure 3.10: Multipath Effect at Near Grazing Incidence

clutter patch and the direction of wave propagation. Land clutter amplitude versus grazing angle was simulated by *Constant Gamma Model* [25], [32] which is defined by parameters, $\sigma_{min}, \gamma, \sigma_{max}$.

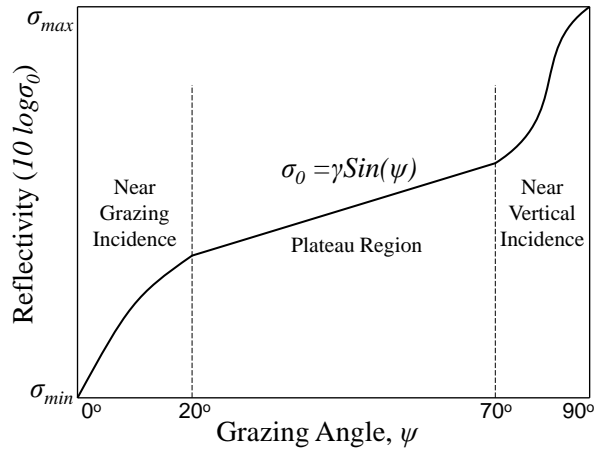


Figure 3.11: Constant Gamma Model

The model defines σ_{min} in the near grazing (0° - 20°) incidence, $\sigma_0 = \gamma \sin(\psi)$ in plateau (20° - 70°) region and σ_{max} near vertical (70° - 90°) incidence (Figure 3.11).

Using “*polyfit*” function in the curve fitting toolbox of MATLAB™, the constant gamma model was formulated with a polynomial $P(\psi)$ (3.42). Where $[a, b, c, d]$ are the result of the *polyfit* function. Appendix (A.1.2) is the source code used to generate $[a, b, c, d]$ parameters by *polyfit* function.

$$P(\psi) = a \cdot e^{b(\psi)} + c \cdot e^{d(\psi)} \quad (3.42)$$

The polynomial parameters of the mathematical model were calculated (Table 3.3) for different types of terrain according to measured clutter data (Table 3.2). Clutter level with respect to grazing angle (Figure 3.12) was generated using equation (3.42) and polynomial parameters (a,b,c,d).

Table 3.3: Clutter Model Parameters (a,b,c,d) for Various Terrain Types

Terrain Type	σ_{max}	γ	σ_{min}	Clutter Parameters			
				a	b	c	d
A Desert Road	-5	-25	-40	0.4642	-0.4400	0.0153	-0.0523
B Cultivated Land	-2	-22	-37	0.9261	-0.4400	0.0304	-0.0523
C Open Woods	4	-16	-31	3.6874	-0.4390	0.1178	-0.0509
D Wooded Hill	5	-15	-30	4.6422	-0.4390	0.1483	-0.0509
E Cities	9	-11	-26	11.6608	-0.4388	0.3708	-0.0507

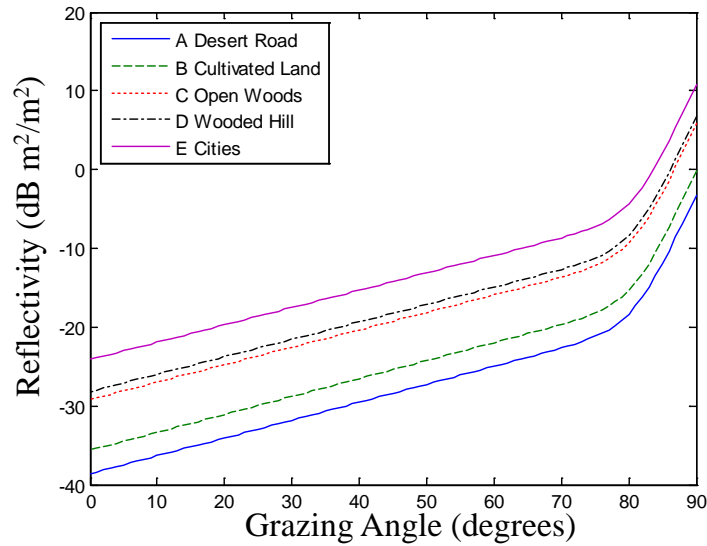


Figure 3.12: Mathematical Clutter Model for Various Types of Terrain

The value of the clutter for Constant Gamma Model at near grazing incidence (0° - 20°) rapidly decreases especially towards 0° but our mathematical model is approximated to a linear function at near grazing incidence. The value of the clutter at near grazing incidences is very small such that σ_{min} is around -25 to -40 dB. For a flat terrain these small grazing angles occur at the points far away from the sensor and the distances between these points and the sensor are relatively long compared with the locations near the sensor with higher grazing angles. The clutter reduction due to the grazing angle and the distance from the sensor is very high at the

locations with small grazing angles. Thus the total effect of these points to the resulting total received power where located at the near grazing incidences is very small. The generated mathematical model matches with the Constant Gamma Model at the near vertical incidence and at the plateau regions better than the match at the near grazing incidence region. But the effect of the points with a smaller grazing angle at the near grazing incidence region is very small so the deviation of the mathematical model from the Constant Gamma Model at near grazing incidences can be neglected.

Unless specified; in the calculations, clutter parameters are taken as $\sigma_{min} = -30$ dB, $\gamma = -15$ dB, and $\sigma_{max} = +5$ dB.

3.1.2 Error Correction Factor

$$V_r = \frac{\sqrt{2Z_0K}\sqrt{I}}{h} \Rightarrow \sqrt{I} = \frac{V_r \cdot h}{\sqrt{2Z_0K}} \quad (3.43)$$

Taking the time derivative of the received voltage and dividing it with the received voltage the constant terms cancels and time varying parameters remains. The integral I was assumed to be constant (3.12) and the time derivative of the integral I was assumed to be zero. Time derivative of integral I (3.50) is zero unless there is no time varying parameters. While the integral I is a time varying parameter the time derivative of it will be non-zero and a new equation was derived for height estimation according to non-zero time derivative of the integral I . Negative change in the height of the sensor with respect to time is the vertical velocity (v_z) of the sensor.

$$\frac{dV_r}{dt} = \sqrt{2Z_0K} \left(\frac{1}{h} \frac{d\sqrt{I}}{dt} - \frac{\sqrt{I}}{h^2} \frac{dh}{dt} \right) = \frac{\sqrt{2Z_0K}}{h} \left(\frac{d\sqrt{I}}{dt} + \frac{V_r \cdot v_z}{\sqrt{2Z_0K}} \right) \quad (3.44)$$

Height of the sensor was estimated by (3.45). If the integral I in (3.45) is zero we get the height estimation equation (3.15) which have been used in the simulation.

$$h = \frac{\sqrt{2Z_0K} \frac{d\sqrt{I}}{dt} + V_r v_z}{\frac{dV_r}{dt}} \quad (3.45)$$

A new parameter called *Correction-Factor* (C) was defined. C is the time derivative of the

square root of the integral I .

$$C = \frac{d\sqrt{I}}{dt} \quad (3.46)$$

Height estimation equation with a time varying integral I is:

$$h = \sqrt{2Z_0K} \cdot C \cdot \left(\frac{dV_r}{dt}\right)^{-1} + V_r \left(\frac{dV_r}{dt}\right)^{-1} \frac{f_{Doppler} \lambda}{2} \quad (3.47)$$

While the integral has two variables θ and ϕ , only the θ component is time varying due to the change of the tilt angle (ζ) during the ballistic trajectory of the sensor.

$$I(\theta, \phi, \zeta) = \int_{\theta=\zeta-\theta_B/2}^{\zeta+\theta_B/2} \int_{\phi=-\phi_B/2}^{\phi_B/2} \cos(\theta) \sigma_0(\theta) f_A^4(\theta, \phi, \zeta) d\theta d\phi \quad (3.48)$$

$$f_A(\theta, \phi, \zeta) = \underbrace{\exp\left(-2\ln(2)\left(\frac{\theta-\zeta}{\theta_B}\right)^2\right)}_{f_A(\theta, \zeta)} \cdot \underbrace{\exp\left(-2\ln(2)\left(\frac{\phi}{\phi_B}\right)^2\right)}_{f_A(\phi)} \quad (3.49)$$

$$I(\theta, \phi, \zeta) = \underbrace{\int_{\theta=\zeta-\theta_B/2}^{\zeta+\theta_B/2} \cos(\theta) \sigma_0(\theta) f_A^4(\theta, \zeta) d\theta}_{I_\theta} \cdot \underbrace{\int_{\phi=-\phi_B/2}^{\phi_B/2} f_A^4(\phi) d\phi}_{I_\phi} \quad (3.50)$$

The integral I was separated into its two variables I_θ and I_ϕ while the ζ variable is only effects the θ component. Chain rule was used to find the time derivative of the integral I , while the integral changes due to change of the tilt angle ζ with respect to time. Derivative of integral I with respect to tilt angle ζ times the time derivative of tilt angle ζ is the time derivative of the integral I (3.51).

$$\frac{d\sqrt{I(\theta, \phi, \zeta)}}{dt} = \frac{d\sqrt{I(\theta, \phi, \zeta)}}{d\zeta} \frac{d\zeta}{dt} = \frac{1}{2\sqrt{I(\theta, \phi, \zeta)}} \frac{dI(\theta, \phi, \zeta)}{d\zeta} \frac{d\zeta}{dt} \quad (3.51)$$

$$\frac{dI(\theta, \phi, \zeta)}{d\zeta} = I_\phi \cdot \frac{dI_\theta}{d\zeta} + I_\theta \cdot \underbrace{\frac{dI_\phi}{d\zeta}}_{zero} = I_\phi \cdot \frac{dI_\theta}{d\zeta} \quad (3.52)$$

There is no variation of I_ϕ with respect to tilt angle ζ and the derivative of I_ϕ is zero then the correction factor C is:

$$C = \frac{d\sqrt{I}}{dt} = \frac{I_\phi}{2\sqrt{I_\theta I_\phi}} \frac{dI_\theta}{d\zeta} \frac{d\zeta}{dt} = \frac{1}{2} \sqrt{\frac{I_\phi}{I_\theta}} \frac{dI_\theta}{d\zeta} \frac{d\zeta}{dt} \quad (3.53)$$

To find the derivative of I_θ with respect to tilt angle ζ Leibniz' Rule (3.54) was used because the tilt angle ζ appears in the limits of the integral I_θ and in the integrand.

$$\frac{d}{d\alpha} \int_{a(\alpha)}^{b(\alpha)} f(x, \alpha) dx = \frac{db(\alpha)}{d\alpha} f(b(\alpha), \alpha) - \frac{da(\alpha)}{d\alpha} f(a(\alpha), \alpha) + \int_{a(\alpha)}^{b(\alpha)} \frac{\partial}{\partial \alpha} f(x, \alpha) dx \quad (3.54)$$

Applying Leibniz' Rule to integral I_θ :

$$\begin{aligned} \frac{dI_\theta}{d\zeta} &= \frac{d}{d\zeta} \left(\int_{\zeta-\theta_B/2}^{\zeta+\theta_B/2} \sigma_0(\theta) f_A^A(\theta, \zeta) \cos(\theta) d\theta \right) = \frac{d}{d\zeta} \left(\int_{a(\zeta)}^{b(\zeta)} g(\zeta, \theta) d\theta \right) \\ &= \underbrace{g(\zeta, b(\zeta)) \frac{db(\zeta)}{d\zeta}}_A - \underbrace{g(\zeta, a(\zeta)) \frac{da(\zeta)}{d\zeta}}_B + \underbrace{\int_{a(\zeta)}^{b(\zeta)} \frac{g(\zeta, \theta)}{d\zeta} d\theta}_C \end{aligned} \quad (3.55)$$

we get $\frac{dI_\theta}{d\zeta} = A B C$ where A,B and C are given in (3.57), (3.58) and (3.59) respectively.

$$\frac{db(\zeta)}{d\zeta} = \frac{d(\zeta + \theta_B/2)}{d\zeta} = 1 \quad \frac{da(\zeta)}{d\zeta} = \frac{d(\zeta - \theta_B/2)}{d\zeta} = 1 \quad (3.56)$$

$$A = g(\zeta, b(\zeta)) \cdot 1 = \sigma_0(\zeta + \theta_B/2) \exp \left[-8 \ln 2 \left(\frac{-\theta_B/2}{\theta_B} \right) \right] \cos(\zeta + \theta_B/2) \quad (3.57)$$

$$B = g(\zeta, a(\zeta)) \cdot 1 = \sigma_0(\zeta - \theta_B/2) \exp \left[-8 \ln 2 \left(\frac{\theta_B/2}{\theta_B} \right) \right] \cos(\zeta - \theta_B/2) \quad (3.58)$$

$$\begin{aligned}
C &= \int_{\zeta-\theta_B/2}^{\zeta+\theta_B/2} \sigma_0(\theta) \cos(\theta) \frac{d}{d\zeta} \left[\exp \left(-8 \ln 2 \left(\frac{\zeta-\theta}{\theta_B} \right)^2 \right) \right] d\theta \\
&= \int_{\zeta-\theta_B/2}^{\zeta+\theta_B/2} \sigma_0(\theta) \cos(\theta) (-16 \ln 2) \left(\frac{\zeta-\theta}{\theta_B} \right) \left[\exp \left(-8 \ln 2 \left(\frac{\zeta-\theta}{\theta_B} \right)^2 \right) \right] d\theta \quad (3.59)
\end{aligned}$$

Tilt angle ζ changes with the gravitational force (g) and ζ approaches to zero at infinity. The rate of change in the tilt angle ζ is given in (3.60)

$$\frac{d\zeta}{dt} = \frac{d}{dt} \left(\arctan \left(\frac{v_x}{v_z} \right) \right) = \frac{d}{dt} \left(\arctan \left(\frac{v_{0x}}{v_{0x} + gt} \right) \right) = - \frac{v_{0x} \cdot g}{(v_{0x} + gt)^2 + v_{0x}^2} \quad (3.60)$$

To calculate the correction factor, the information of the release angle and velocity must be known.

In real situations, before the release of the munitions, operation planners prepares an operation plan which defines the release velocity and angle. Using the planned information, the correction factor can be loaded on ground prior to the operation. Another possible way to load the correction factor to the sensor is to get the actual release velocity and angle from the carrier (such as an aircraft) and the correction factor can be calculated by the sensor processor. This solution seems to be complicated at first sight but to send actual initial release parameters from the aircraft to the sensor is feasible. Main timing setups, such as arming time, functioning time, or burst height can be programmed by the pilot in many modern fuze systems by using the wire communication (via an umbilical cable) or magnetic coupling just before the release of the munitions. The same connection setup may be used to provide the initial release parameters from aircraft to the sensor. A good estimated normalized cross section σ_0 can be preloaded if the target location and the reflection properties of the terrain are known.

For the reflection parameters $\sigma_{max} = 1$, $\gamma = -10$ and $\sigma_{min} = -20$ dB the correction factors were calculated for velocities 100 m/s to 500 m/s and for the release angles of 0° to 90° (Figure 3.13). It was observed that the correction factor approaches to zero when the release angle approaches to vertical (towards the center of the earth's gravitational force). If the sensor release angle is near vertical the gravitational force is nearly aligned with the sensor axial velocity so there is not any change in the direction of the sensor keeping the angles

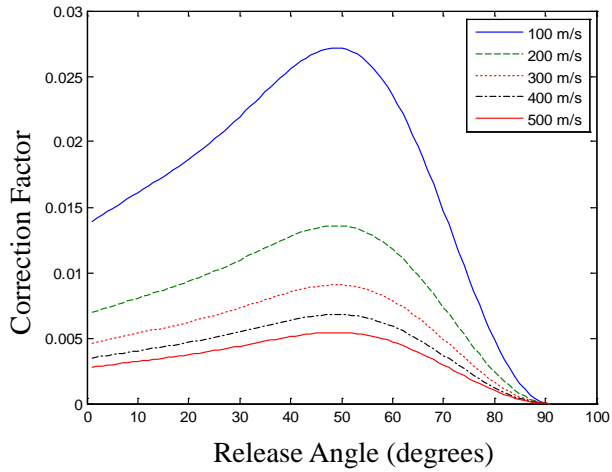


Figure 3.13: Correction Factor for Various Velocities and Various Release Angles ($\theta_B = \phi_B = 70^\circ$)

unchanged and yielding zero correction factor. The reflection coefficients differs for different types of terrain. From Table 3.2 the difference between average γ values for desert road and wooded hill is approximately 10 dB. For the *wooded hill* type terrain the clutter modelled with the clutter parameters $\sigma_{max} = 5$, $\gamma = -15$ and $\sigma_{min} = -30$ dB and for the *desert road* type terrain the clutter modelled with the clutter parameters $\sigma_{max} = -5$, $\gamma = -25$ and $\sigma_{min} = -40$ dB (Figure 3.14).

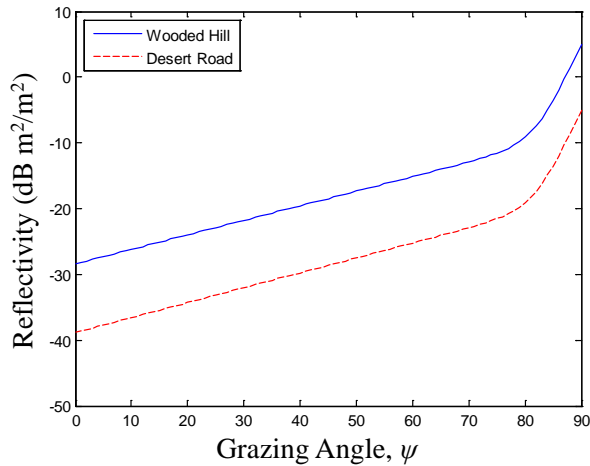


Figure 3.14: Clutter Model for Wooded Hill and Desert Road

The correction factor for wooded hill and desert road for different velocities and release angles was calculated (Figure 3.15) using the clutter model for desert road and wooded hill.

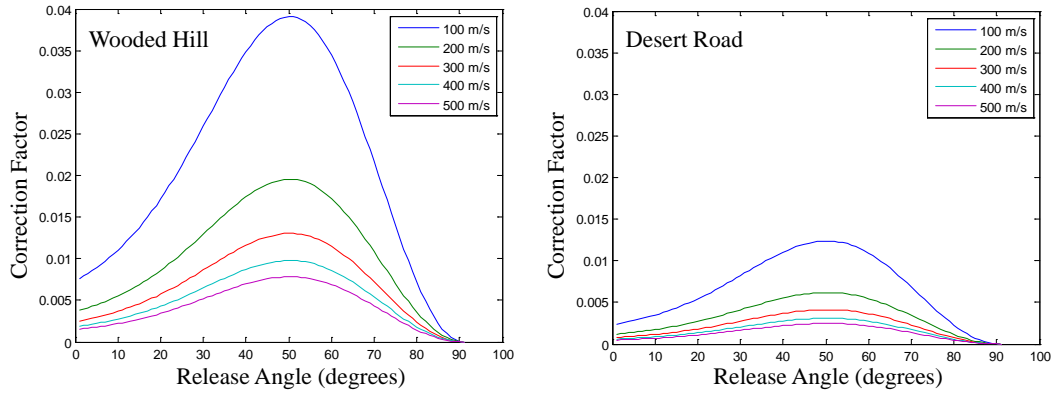
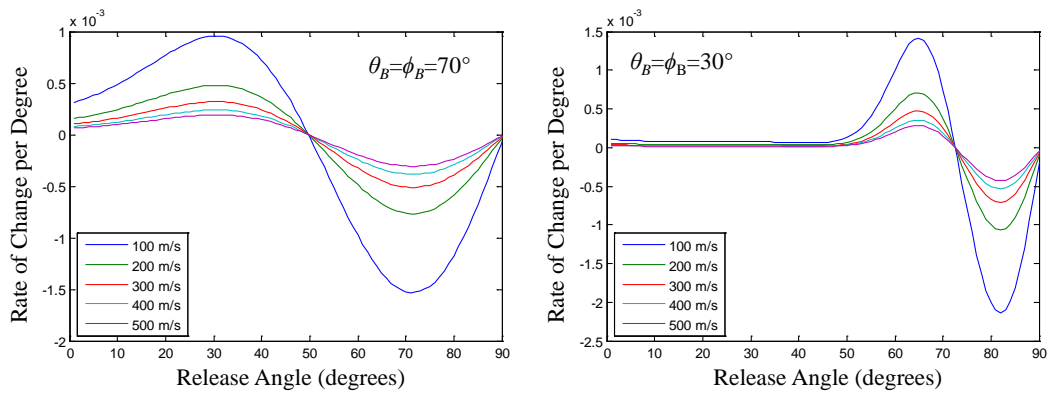


Figure 3.15: Correction Factor for Wooded Hill and Desert Road ($\theta_B = \phi_B = 70^\circ$)

The rate of change in correction factor per degree is the measure of the sensitivity of the sensor to the release parameter. For higher beamwidths and higher velocities the sensor is more sensitive to release angle variations (Figure 3.16). In practical situations, if the correction factor is calculated for a low release angle at the planning phase and then the actual release deviates from the planned, the adversely effects of the erroneous correction factor on the height estimation if higher for large antenna beamwidths when compared with the narrower antenna beamwidths.



(a) Antenna Beamwidths= 70°

(b) Antenna Beamwidths= 30°

Figure 3.16: Rate of Change in Correction Factor per Degree for Wooded Hill

CHAPTER 4

SIMULATION FOR FLAT TERRAIN

4.1 Simulation (Flat Terrain)

A numerical simulation for calculating the trajectory and received power at the antenna port was programmed using MATLAB™ GUI to estimate the height using (3.45) (Figure 4.1). Initially, the release (dive) angle and the trajectory of the sensor was calculated. Initial velocity of the sensor generally ranges from 125 m/s to 250 m/s for fighter aircraft and the release angle ranges from 0° to 50°. At each defined sampling point vertical and horizontal velocities and the tilt angle was calculated. The received power at the antenna port and the Doppler shift were calculated using predefined system parameters such as: transmitted power, antenna elevation and azimuth beamwidths, gain, and land clutter parameters. Finally, calculated power was used to estimate the height.

To simulate the environment in a more realistic manner, the land reflectivity was modeled as described in Section 3.1.1.4. Normalized RCS σ_0 (radar cross section per unit area) was used in the calculations. The radar cross section σ is equal to $\sigma_0 A$ where A is the area of the illuminated terrain. In the new approach this area was calculated indirectly by integrating the received signal power (dP_r) reflected from the infinitesimally small area dA over the antenna beamwidth, thus resulting in the total reflection from the whole area covered by the antenna beam. Land clutter with the parameters σ_{min} , γ , σ_{max} were expressed as an exponential parametric model (3.42). Using MATLAB curve fitting toolbox the parameters a , b , c , and d , were determined. With the help of this model of the land clutter, the experimental data collected by various experiments for land clutter were used in the simulation to take the dependence of reflectivity to the grazing angle into account.

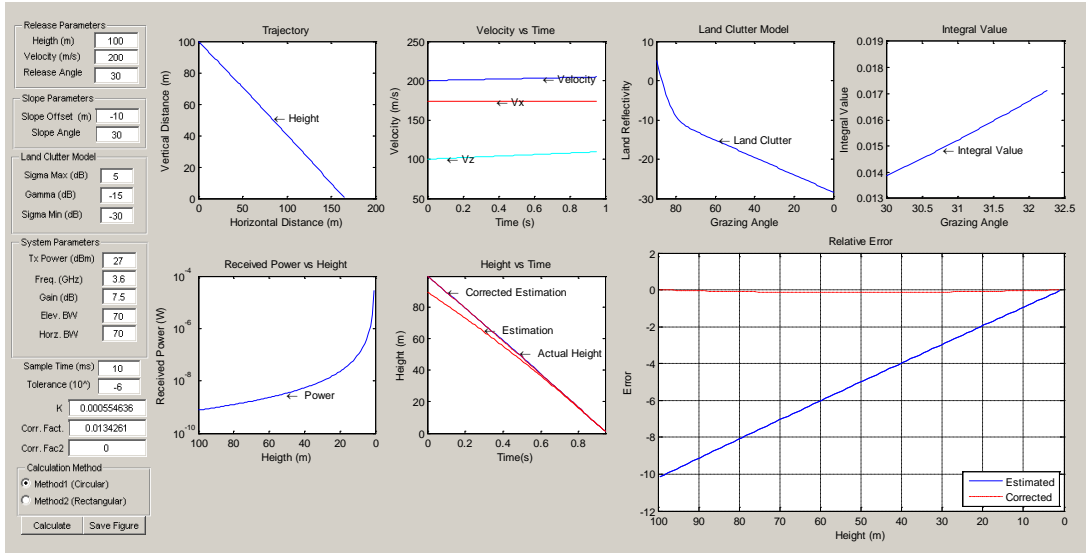


Figure 4.1: Graphical User Interface for Simulating the Reflection from Flat Terrain

In the simulation, release parameters (height, velocity, and angle), land reflectivity parameters (σ_{min} , γ , σ_{max}), sensor parameters (P_0 , G_0 , θ_B , ϕ_B , λ), and sampling time can be set. At every sampling time the received power with respect to sensor position and tilt angle were calculated.

The outputs of the simulation are:

- Trajectory and velocity components of the sensor,
- Land clutter mathematical model according to the constant gamma model parameters,
- Received power,
- Estimated height (without correction factor applied), and corrected estimation of the height (with correction factor applied).

4.2 Estimation Results for the Flat Terrain

As an application example, consider a sensor with an initial velocity of 100 m/s and release angle of 20° . For this sensor, spatial distribution of the received power is given in Figure 4.2. It was assumed that transmitted power is 33 dBm, gain of the antenna is 7.5 dB, frequency is 3.6 GHz and elevation and azimuth beamwidths are 70 degrees.

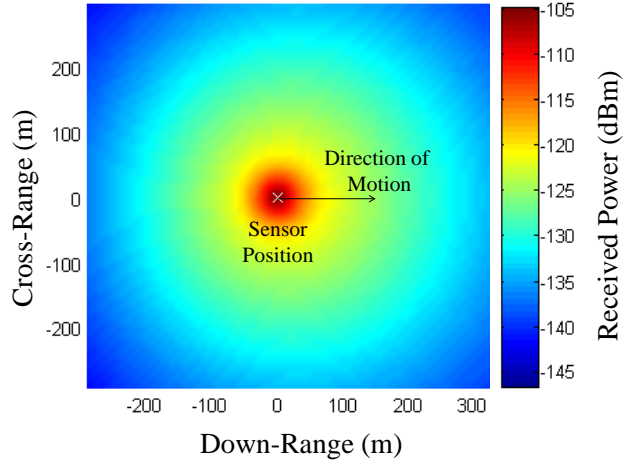


Figure 4.2: Return Power ($h_0 = 300$ m, $v_0 = 100$ m/s, and $\zeta_0 = 80^\circ$)

The estimation of the height of this sensor released from 300 m is calculated to be as given in Figure 4.3. As seen in this figure, there is a considerable initial estimation error.

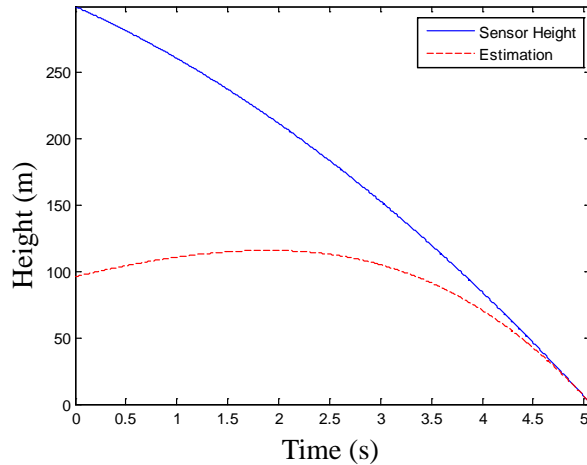


Figure 4.3: Estimation Result ($h_0 = 100$ m, $v_0 = 100$ m/s, and $\zeta_0 = 80^\circ$)

The results with corrected estimation for a sensor released at two different altitudes, velocities and angles are given in Figure 4.4 and Figure 4.5.

Main source of estimation error is the change of the tilt angle during the sensor trajectory. Corrected estimation yields a maximum relative error less than 12.5% (Figure 4.5). When the release velocity is smaller the tilt angle change is faster. Similarly, the rate of change in the tilt angle is faster when the release angle is small. For the cases with higher release angles and higher release velocities, lower margin of error can be obtained as depicted in Figure 4.6 and

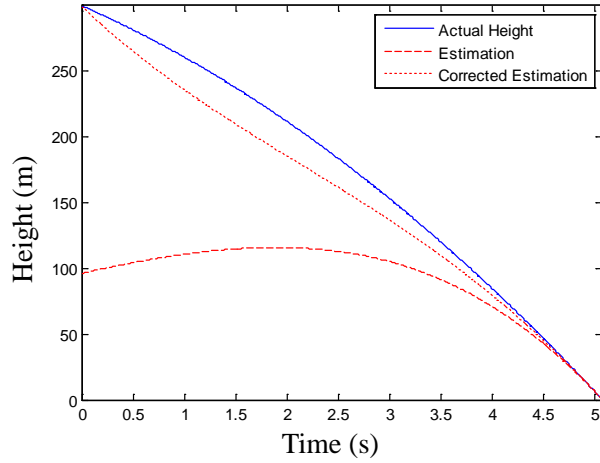


Figure 4.4: Corrected Estimation ($h_0 = 2000$ m, $v_0 = 200$ m/s, $\zeta_0 = 80^\circ$, and $C = 0.0269$)

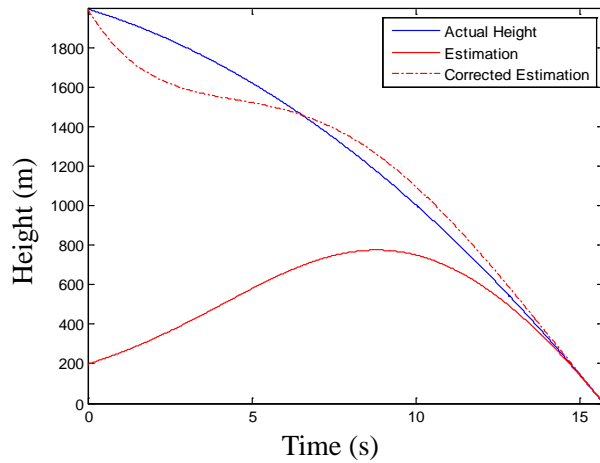


Figure 4.5: Corrected Estimation ($h_0 = 300$ m, $v_0 = 100$ m/s, $\zeta_0 = 80^\circ$, and $C = 0.0179$)

Figure 4.7. While the release angle increases change in the tilt angle of the sensor during the trajectory decreases and this results in less absolute error in height estimation (Figure 4.6), similarly, while the release velocity is higher the change in the tilt angle and in the integral I is smaller yielding more accurate results (Figure 4.7).

Variation in the received voltage amplitude depends on the change in height, but the change partially depends on the integral I . The change in I is caused by the changes in land reflectivity and by the changes in tilt angle ζ .

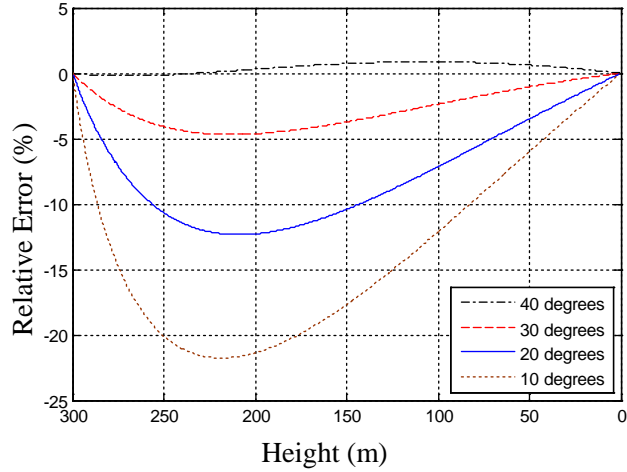


Figure 4.6: Relative Error for Various Release Angles ($h_0 = 300$ m, $v_0 = 100$ m/s)

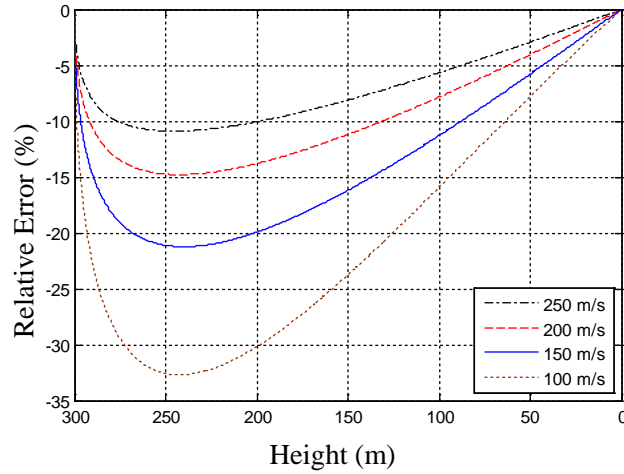


Figure 4.7: Relative Error for Various Release Velocities ($h_0 = 300$ m, $\zeta_0 = 90^\circ$)

4.3 Noise Analysis

Transmit and receive sections of a sample Proximity Sensor system is given in Figure 4.8. This sample system was analysed for noise considerations.

Flow of charges and holes in the solid state devices and the thermal vibrations in any microwave component at a temperature above absolute zero is the cause of the noise. Noise temperature (T) is the expression of the noise introduced to the system. For the receivers, noise considerations play an important role because it is one of the dominant limitations limiting the effectiveness of the receiver. System will be subjected to two kinds of noises. One is the phase noise and the other is the thermal noise. The phase noise (P_N) is oriented from

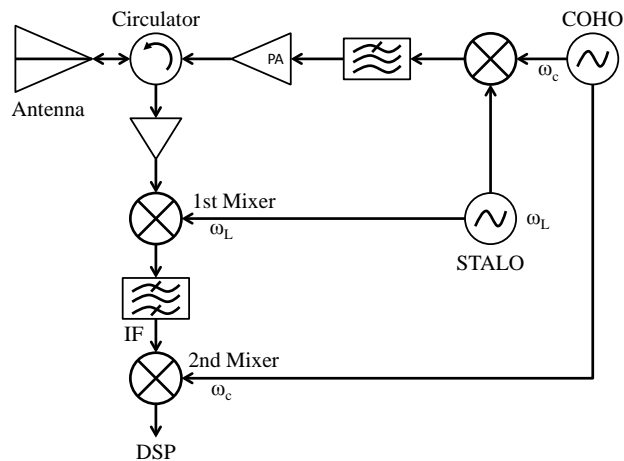


Figure 4.8: Single Channel Proximity Sensor Tx/Rx Module

the voltage controlled oscillator (VCO); the thermal noise (T_N) is oriented from VCO, solar/galactic noises (which are called cosmic noises) and atmospheric absorption noises. The amplitude noise of a VCO is approximately 20 dB lower than the phase noise.

4.3.1 Effect of VCO Phase Noise

The sources of the phase noise of a VCO is caused mainly by;

- *Flicker Noise* depends on the VCO characteristics at low frequencies. The traps (holes and electrons) in the emitter-base depletion layer (formed by the contaminations and crystal defects) holds and release the carriers in a random way and cause low-frequency noise.
- *The Thermal Noise* in the oscillator loop may be selectively enhanced by the loop, resulting phase noise. Also, the thermal noise may directly modulate the oscillation frequency in the oscillation loop.

The phase noise levels according to the carrier frequency is expressed in dBC/Hz and the characteristics of the VCOs are measured in 1 Hz bandwidth centred at the off-set frequency from the carrier. The phase noise sources are given in Figure 4.9.

The phase and the thermal noises of the VCO may be injected to the receiver IF side via;

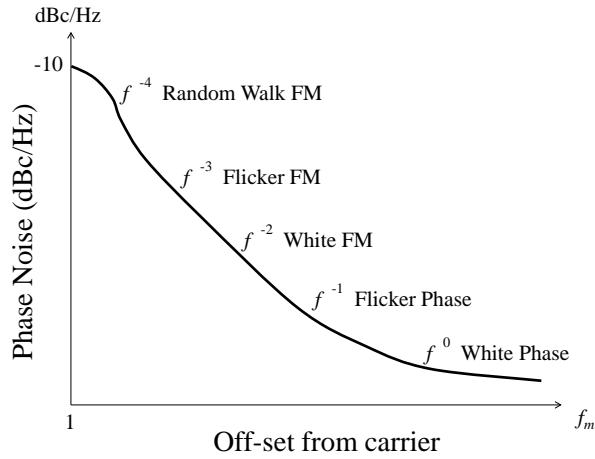


Figure 4.9: Sources of the Phase Noise

- Local Oscillator (LO) port of the mixer,
- Leaking from circulator,
- Reflecting back from antenna,
- Reflecting back from ground.

The phase noise of the local oscillator (w_{pnc}) in dBc/Hz can be mathematically modeled by a power equation (4.1). Sample data is taken from Mini-Circuits' ROS-3600-619 VCO which is a 2950 to 3600 MHz VCO [33](Figure 4.10).

$$w_{pnc,dBc/Hz} = 680 \cdot f^{-0.017} - 680 \quad (4.1)$$

Spectral density $S_{pn}(\omega_n)$ of the phase noise at the input of the DSP port in Figure(4.8) can be modelled by (4.2) [34]. $\chi_n(\omega_n)$ is the correlation factor (4.4). ω_n is the rate of deviation from from the carrier frequency.

$$S_{pn}(\omega_n) = w_{pn}(\omega_n) \times \chi_n^2(\omega_n) \quad (4.2)$$

$$w_{pn}(\omega_n) = 10^{(w_{pnc,dBc/Hz})/10} \quad (4.3)$$

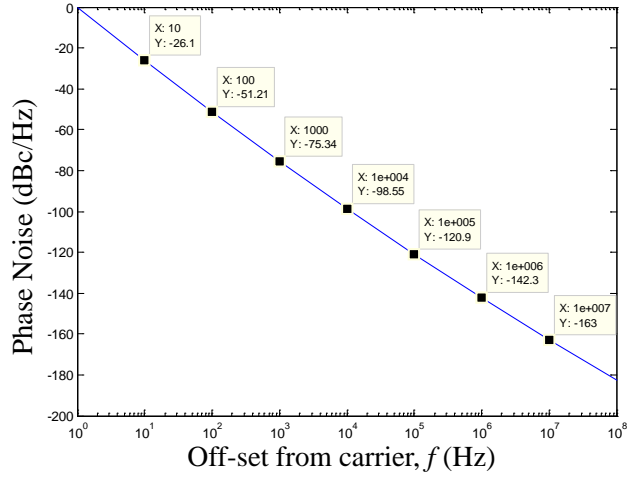


Figure 4.10: Sample Phase Noise Characteristic (Minicircuits' ROS-3600-619 VCO)

$$\chi_n(\omega_n) = 2 \sin\left(\frac{\omega_n T_d}{2}\right) = 2 \sin\left(\frac{\omega_n 2|\vec{r}'|}{c}\right) \quad (4.4)$$

The time delay between the transmitted signal T_d is related to the position of the reflection point on the surface. The relative position of the reflecting surface is a function of (θ, ϕ, ζ) in Figure (4.11).

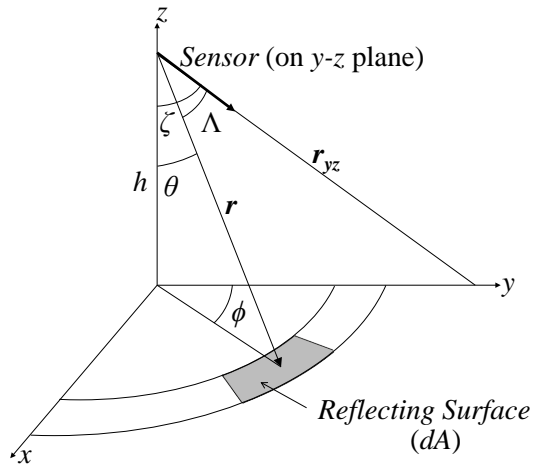


Figure 4.11: Distance between the Sensor and the Reflecting Surface Element

The frequency deviation from the carrier is the Doppler shift and expressed by (4.5)

$$f_{Doppler} = \frac{2 v_0 \cos(\Lambda)}{\lambda} \quad (4.5)$$

$$\cos(\Lambda) = \frac{\vec{r}_{yz} \cdot \vec{r}}{|\vec{r}_{yz}| \times |\vec{r}|} \quad (4.6)$$

$$\cos(\Lambda) = \frac{1 + \frac{\cos(\phi)}{\tan(\zeta) \tan(\theta)}}{\sqrt{1 + \cot^2(\zeta)} \sqrt{1 + \cot^2(\theta)}} \quad (4.7)$$

The time delay between the transmitted signal and the received signal (T_d) is a function of distance (r), and r is related to the Doppler shift through the angles (θ, ϕ, ζ). Therefore r can be expressed by a function of Doppler shift ($g(f_{Doppler})$) resulting in (4.8)

$$\chi_n(\omega_n) == 2 \sin\left(\frac{\omega_n}{2} \frac{2g(f_{Doppler})}{c}\right) \quad (4.8)$$

Phase noise will be entering to the system through the FFT process of the echo signal. If the relative error due to the Doppler frequency measurement is assumed to be less than 1%, then the maximum Doppler shift deviation ($\Delta f_{Doppler}$) must be;

$$\Delta h = C \cdot \left(\frac{dV_r}{dt}\right)^{-1} + V_r \left(\frac{dV_r}{dt}\right)^{-1} \frac{\Delta f_{Doppler} \lambda}{2} \quad (4.9)$$

$$\frac{\Delta h}{h} < \frac{\Delta f_{Doppler}}{f_{Doppler}} < 0.01 \quad \Rightarrow \quad \Delta f_{Doppler} = 20\text{Hz} @ v_0 = 100\text{m/s}, f_0 = 3.6\text{GHz} \quad (4.10)$$

Thus, the phase noise power (P_{pn}) entering to the system can be found by (4.14), where P_r is the received power.

$$\Delta P_{pn}^{Center}(f_{Doppler}, \Delta f_{Doppler}) = \Delta P_r(f_{Doppler}, \Delta f_{Doppler}) \cdot \int_{\Delta f_d/2}^{3\Delta f_d/2} w_{pn}(\omega_n) \chi_n^2(\omega_n \frac{T_d}{2}) df_n \quad (4.11)$$

$$\Delta P_{pn}^{Left}(f_{Doppler}, \Delta f_{Doppler}) = \Delta P_r(f_{Doppler}, \Delta f_{Doppler}) \cdot \int_{\Delta f_d/2}^{3\Delta f_d/2} w_{pn}(\omega_n) \chi_n^2(\omega_n \frac{T_{d1}}{2}) df_n \quad (4.12)$$

$$\Delta P_{pn}^{Right}(f_{Doppler}, \Delta f_{Doppler}) = \Delta P_r(f_{Doppler}, \Delta f_{Doppler}) \cdot \int_{\Delta f_d/2}^{3\Delta f_d/2} w_{pn}(\omega_n) \chi_n^2(\omega_n \frac{T_{d_2}}{2}) df_n \quad (4.13)$$

$$\Delta P_{pn}^{Total} = \Delta P_{pn}^{Center} + \Delta P_{pn}^{Left} + \Delta P_{pn}^{Right} \quad (4.14)$$

Spectral Density of the Return Power

Spectral density of the return power ($P_r(f_{Doppler})$) can be calculated analytically. Doppler spectrum for an airborne radar was derived by [26, p.388]. Spectrum at the radar receiver is dominated by the platform motion. The assumptions for deriving the spectrum were as follows:

- The antenna beam-width is less than 0.25 radians with a circular symmetry in radiation pattern. The antenna pattern was also assumed to have a circular symmetry in radiation pattern (5.25).
- Clutter is assumed to be homogeneous with a mean velocity smaller than the velocity of the platform so the Doppler spectrum was dominated by the platform motion.
- Target and clutter are many times the unambiguous range and the unambiguous range is related to the pulse duration.

One or more side-lobe involved in the calculations where the calculations were based on the main beamwidth. Outside of the first side-lobe the side-lobe clutter spectrum is essentially flat.

The Doppler spectral density is given in (4.15) where the angle between the antenna axis and the direction of the platform (squint angle) is Λ (Figure 4.12).

$$w_m(f_d) = \frac{10^{-8} P_t d_t G_0^2 \lambda^3 \theta_1 \sin(\psi) \sigma_0(\psi)}{h^2 v \sin(\Lambda)} \quad (4.15)$$

w_m is the maximum spectral density in watts/hertz at f_d where

d_t transmit duty cycle,

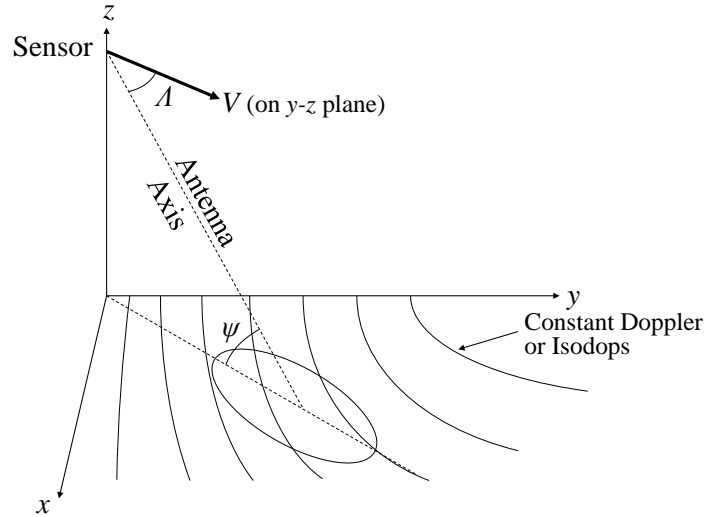


Figure 4.12: Doppler Spectrum Isodops

- G_0 peak antenna gain,
- θ_1 one-way half-power beamwidth,
- $\sigma(\psi)$ normalized backscatter coefficient at angle ψ ,
- v velocity of the platform in Knots.

The shape of the main beam clutter spectrum is:

$$w_m(f_d \pm \Delta f) = w_m(f_d) \operatorname{erfc} \left[\frac{0.0387 \lambda \Delta f}{v \theta_1 \sin(\Lambda)} \right] \quad \text{W/Hz} \quad (4.16)$$

where erfc is the complement of the error function.

$$\operatorname{erfc}(x) = \frac{2}{\sqrt{\pi}} \int_x^{\infty} e^{-t^2} dt \quad (4.17)$$

f_d is the Doppler frequency of the echoes from the center of the main beam and calculated by (4.18) where v is in meter/seconds.

$$f_d = \frac{2v \cos(\Lambda)}{\lambda} \quad (4.18)$$

The relation between the distance (r) and the Doppler shift ($f_{Doppler}$) is directly available in the DTED simulation in Section (5.2). Using the DTED simulation the phase noise of the system was calculated. The SNR level is given in Figure 4.13. The parameters are; Release velocity=100 m/s, Release Angle=40°, Transmitted Power=33 dBm, Frequency=3.6 GHz, and Antenna Beamwidths (azimuth and elevation)=30°.

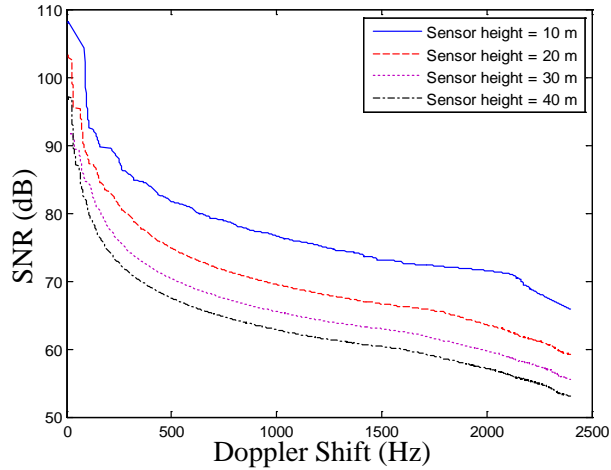


Figure 4.13: Signal to Noise Ratio

The low frequency components are much more correlated resulting higher SNR levels. The SNR is more than 50 dB for the heights lower than 50 meters.

4.3.2 Thermal Noise

Thermal noise (TN) is oriented from VCO and from solar, galactic (which are called cosmic noises) and atmospheric absorption noises. It is assumed that the thermal noise due to galactic and solar noises will be dominant. VCO will contribute to overall system noise by introducing phase noise to the receiver side from the LO port and due to reflection from ground. Total antenna temperature (T_A) is the sum of the cosmic noise temperature ($T_{b,ant}$) and atmospheric absorption noise temperature (T_e). Cosmic noise temperature also called brightness temperature (T_b) is equal approximately to 100° K. T_a is the ambient temperature, T_e is the effective noise temperature (result of atmospheric absorption noise).

$$T_A = T_{b,ant} + T_e = T_b \left(1 - \frac{T_e}{T_a} \right) + T_e \quad (4.19)$$

For the case of the ambient temperature is 323° K (50° C) and atmospheric absorption loss (L) is 1 dB, the effective noise temperature (T_e) and the total effective antenna temperature (T_A) is equal to:

$$T_e = T_a(L - 1) = 323 \left(10^{\frac{1}{10}} - 1 \right) \approx 84^\circ \text{ K} \quad (4.20)$$

$$T_A = T_b \left(1 - \frac{T_e}{T_a} \right) + T_e = 100 \left(1 - \frac{84}{323} \right) + 84 \approx 154^\circ \text{ K} \quad (4.21)$$

For a network with noise figure F_n , gain G , and bandwidth BW , the relationship between the input and the output noise temperature can be found by (4.22) and the thermal noise power TN can be calculated by (4.23). k is the Boltzmann constant and is equal to 1.38×10^{-23} .

$$T_{n,out} = ((F - 1)T_0 + T_{n,in}) G \quad (4.22)$$

$$TN = k T_n G BW \quad (4.23)$$

The noise figure, gain and bandwidth values for a single channel receiver is given in Figure 4.14.

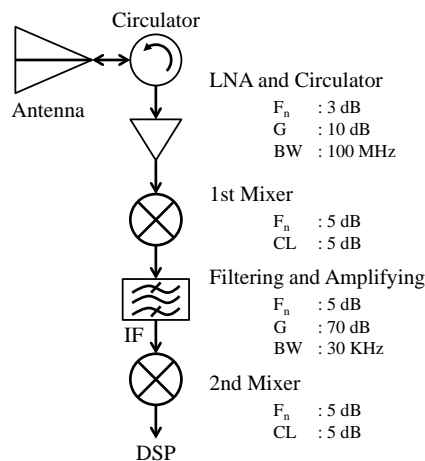


Figure 4.14: Sample Receiver Stage with Gains and Noise Figures

The thermal noise levels at different ports are given in Table 4.1.

Table 4.1: Thermal Noise Levels at Different Ports of the Receiver

	Antenna	1 st Mixer Input	1 st Mixer Output	2 nd Mixer Input	DSP Input
Noise Temperature (° K)	154	734	1894	3054	4214
Thermal Noise Power (TN_{dBm})	-96.7	-86.7	-94.9	-51.1	-124.0

The received signal, phase noise and the thermal noise at the DSP port of the system is given in Figure 4.15.

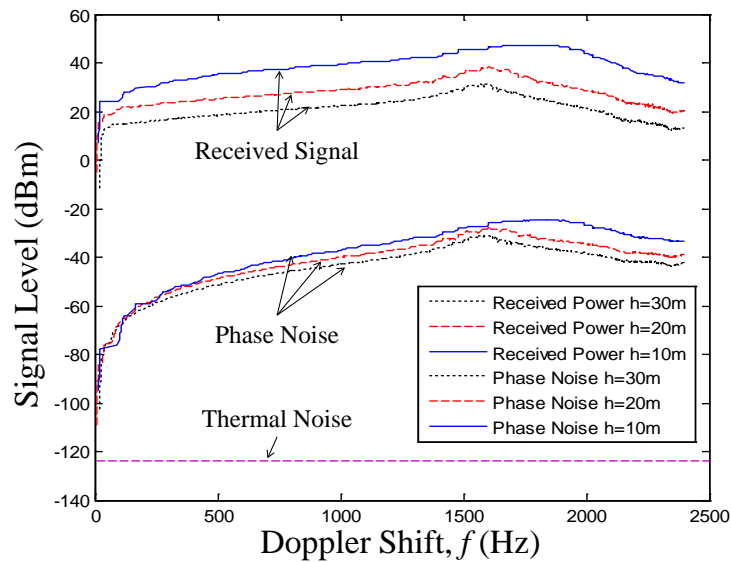


Figure 4.15: Return Signal with Phase and Thermal Noises

4.3.3 Noise Reduction

To observe the effect of the noise to the estimation a noise to the amplitude of the received voltage was added. The error of height estimation for the initial parameters $h_0 = 100\text{m}$, $v_0 = 100\text{m/s}$, and $\zeta_0 = 60^\circ$ is shown in Figure 4.16.

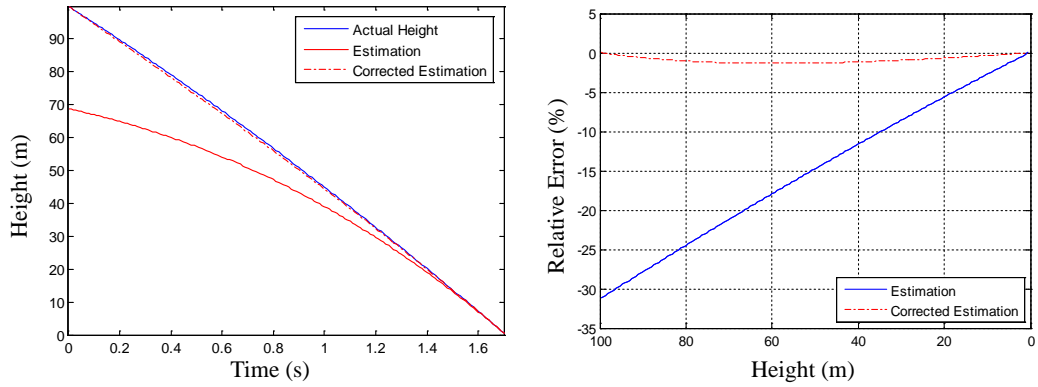


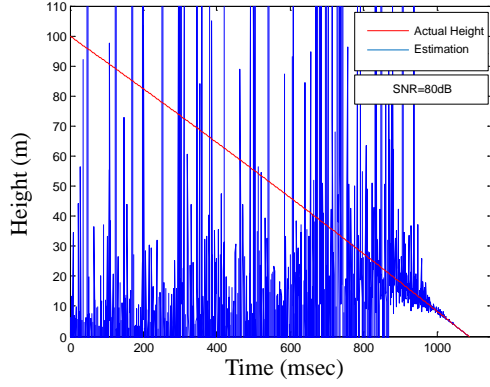
Figure 4.16: Height Estimation ($h_0 = 100$ m, $v_0 = 100$ m/s, and $\zeta_0 = 60^\circ$)

4.3.3.1 Moving Average Filtering for Noise Reduction

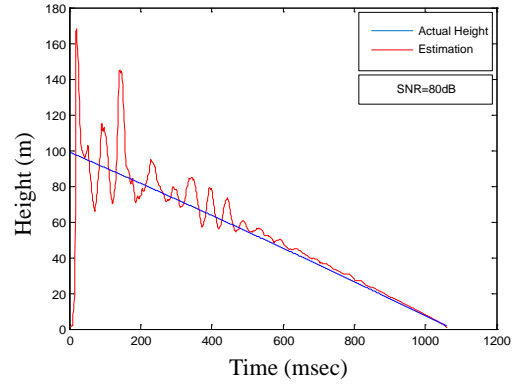
For the ideal case with the specified parameters there is only a relative error of less than 5% for the corrected estimation. However, the estimation of height is much worse than the ideal case if there is a noise on the envelope of the received voltage (Figure 4.17.(a)). The estimated height is maximum 10 meters.

In this case the SNR level was around 80 dB and the inserted noise was Additive White Gaussian Noise (AWGN). Additive White Gaussian Noise is assumed to have zero mean and unknown variance σ^2 is normally distributed. It is a random process having the uniform spectrum density at all frequencies. Two values of white noise in any moments of time (regardless how close each other) are always independent [35, p.288]. To overcome this problem filtering the envelope of the received signal can enhance the performance of the estimation. For using only a moving average window filter (with a duration of 10 ms) the height can be estimated tolerably up to 50 meters (Figure 4.17.(b)).

For an SNR of 60 dB the maximum estimation limit decreases down to 5 meters (Figure 4.18.(a)). By taking the average of the voltage signal the noise effect decreases and the maximum estimation height can be increases up to 30 meters (Figure 4.18.(b)).

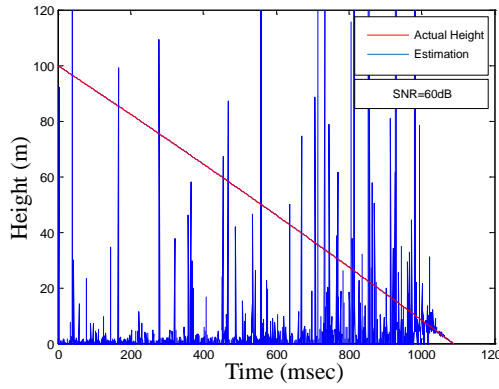


(a) Without Filtering

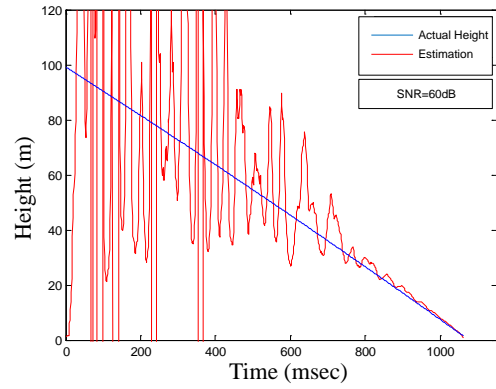


(b) With Filtering

Figure 4.17: Height Estimation, SNR=80 dB ($h_0 = 100$ m, $v_0 = 100$ m/s, and $\zeta_0 = 60^\circ$)



(a) Without Filtering



(b) With Filtering

Figure 4.18: Height Estimation, SNR=60 dB ($h_0 = 100$ m, $v_0 = 100$ m/s, and $\zeta_0 = 60^\circ$)

4.3.3.2 Linear Regression (LR) for Noise Reduction

Estimation of the height for a noiseless ideal environment yielded very close results for the estimation of height. When a Gaussian white noise is added to the received signal amplitude the estimation had some high estimation errors especially when the SNR is considerably low. A linear model for the voltage level using linear regression to avoid resulting peaks in the estimation due to the additive noise was modelled. The estimated model (4.24) is a *linear second order model* whereas the order of the model can be any size.

$$Y = \beta_0 + \beta_1 X + \beta_{11} X^2 + \epsilon \quad (4.24)$$

By using Least Squares Estimation (LSE) the error was tried to minimized by ($\sum \epsilon^2$) which

is the sum of the deviations of the estimation from the true line. For a *linear first order model* let Y be the model to be predicted (4.25) and \hat{Y} is the prediction of Y (4.26).

$$Y = \beta_0 + \beta_1\chi + \epsilon \quad (4.25)$$

$$\hat{Y} = b_0 + b_1\chi. \quad (4.26)$$

Sum of the errors S is

$$S = \sum_{i=1}^n \epsilon_i^2 = \sum_{i=1}^n (Y_i - \beta_0 - \beta_1\chi_i) \quad (4.27)$$

to estimate b_0 and b_1 they were replaced with β_0 and β_1 and the sum of the squares of the deviation was set to zero.

$$\frac{\partial S}{\partial \beta_0} = -2 \sum_{i=1}^n (Y_i - b_0 - b_1\chi_i) = 0 \quad (4.28)$$

$$\frac{\partial S}{\partial \beta_1} = -2 \sum_{i=1}^n \chi_i (Y_i - b_0 - b_1\chi_i) = 0. \quad (4.29)$$

Equations (4.28) and (4.29) are called the normal equations. Deriving b_0 and b_1 from normal equations we get

$$b_1 = \frac{\sum (\chi_i - \hat{\chi})(Y_i - \hat{Y})}{(\chi_i - \hat{\chi})^2} \quad (4.30)$$

$$b_0 = \bar{Y} - b_1\hat{\chi} \quad (4.31)$$

$$\bar{\chi} = \sum \frac{\chi_i}{n} \quad \bar{Y} = \sum \frac{Y_i}{n} \quad (4.32)$$

Then the final predicted model \hat{Y} was found by (4.33)

$$\hat{Y} = \bar{Y} + b_1 (\chi - \bar{\chi}) \quad (4.33)$$

The normally distributed error is assumed to have zero mean and an unknown variance σ^2 and is only for the response data not in predictor data [36]. While the AWGN have zero mean and normally distributed, linear regression method was applied in the estimation. The noisy voltage envelope is predicted by linear regression to acquire a smoother envelope. Linear regression method was applied to the voltage envelope before estimating the height for a duration of 30 ms and the estimation result is given in Figure 4.19 and in Figure 4.20.(a) and for a linear regression with a duration of 50 ms the estimation is given in Figure 4.20.(b).

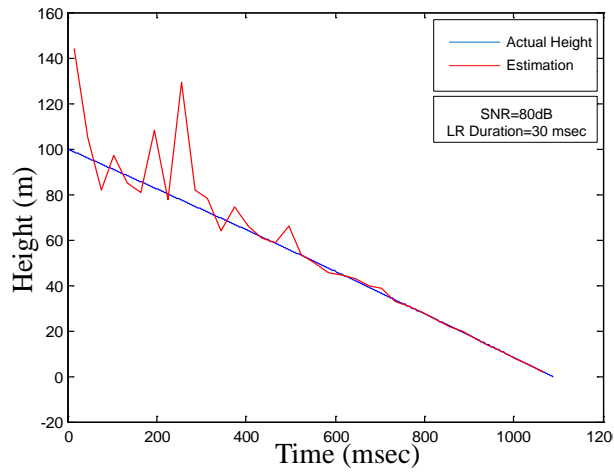
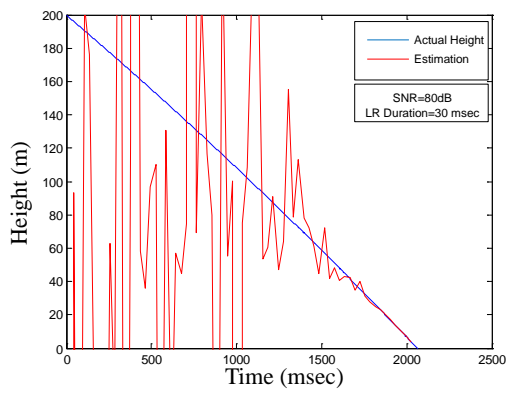
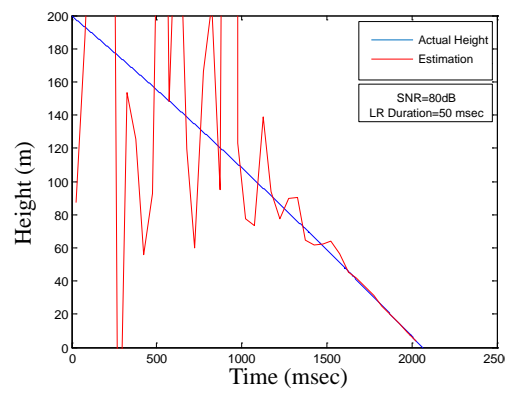


Figure 4.19: Height Estimation, SNR=80 dB, Linear Regression Duration 30 ms ($h_0 = 100$ m, $v_0 = 100$ m/s, and $\zeta_0 = 60^\circ$)



(a) Linear Regression Duration=30 ms



(b) Linear Regression Duration=50 ms

Figure 4.20: Height Estimation, SNR=80 dB ($h_0 = 200$ m, $v_0 = 100$ m/s, and $\zeta_0 = 60^\circ$)

CHAPTER 5

SIMULATION FOR DOUBLE-PLANE TERRAIN

5.1 Simulation for Double-Plane Terrain

In Section (3) the reflection from a planar surface was calculated without any irregularities on the terrain. This is an ideal situation but in real conditions terrain has a lot of irregularities. At the final phase of the sensor which is a height less than 30 meters the illuminated area by the antenna is limited and it may be thought as a planar surface depending on the structure of the terrain. Reflections from a terrain composed of two planes was calculated and the height is estimated to investigate the behaviour of the sensor over non uniform terrain.

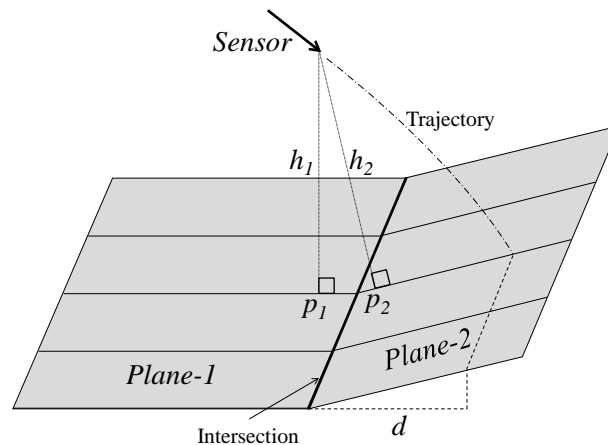


Figure 5.1: Structure of the Double-Plane Geometry

The condition with a two planar surface is the easiest condition to simulate and calculate relevant parameters except one single planar terrain which was calculated in Section (4). Problem of the two-planes structure was defined and the reflected power together with the Doppler shift

was calculated according to Figure 5.1.

5.1.1 Calculating Reflection from a Rectangular Patch

In Section (3) the reflected power from a clutter element was calculated using spherical coordinate system (3.2). The received power from a differential clutter element (Figure 5.2) in rectangular coordinate system given in (5.1).

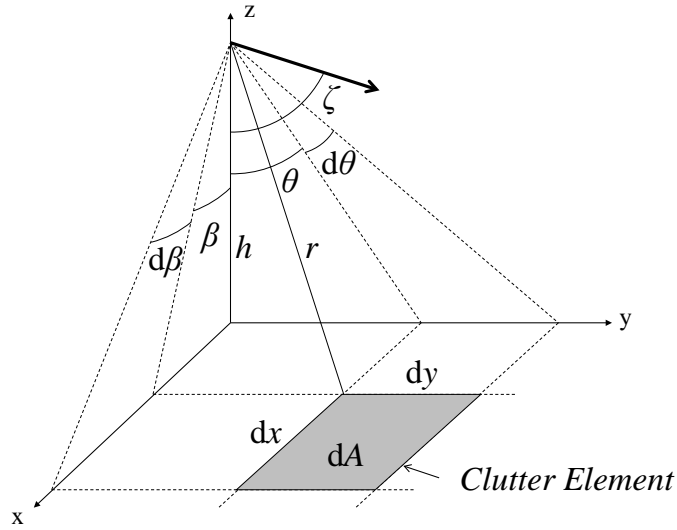


Figure 5.2: Differential Clutter Element

$$dP_r = \frac{P_0 G_0 \lambda^2 F^4(\theta, \beta, \zeta) \sigma_0(\alpha) dA}{(4\pi)^3 r^4} \quad (5.1)$$

Integral of (5.1) was taken at the limits of the antenna beam-widths both at the azimuth and elevation planes to calculate the total reflection by summing-up the reflections from each clutter elements which are illuminated by the sensor beam (5.2). Clutter area is dx times dy. Integral limits were between the beam-widths of both the azimuth and elevation patterns. In the rectangular coordinate system ($\zeta - \theta$) was the angle on the elevation plane and β was the angle on the azimuth plane. The sensor axis was assumed to be lying on the yz plane which is the elevation plane for the easy of formulation (Figure 5.3).

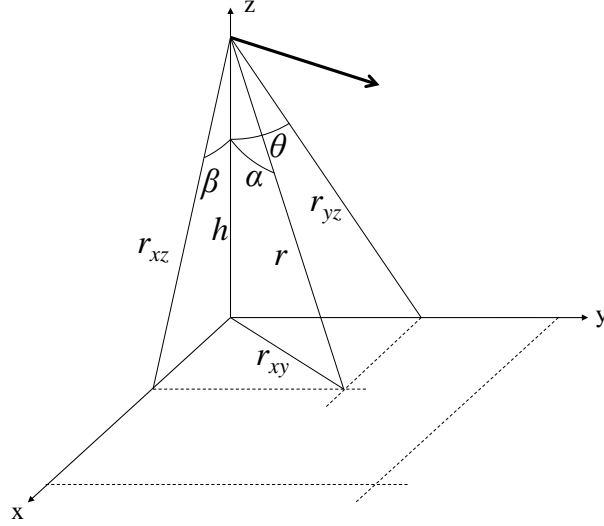


Figure 5.3: Distances on xx , xz and yz Planes

$$P_r = \frac{P_0 G_0 \lambda^2}{(4\pi)^3} \int_{\theta=\zeta-\theta_B/2}^{\zeta+\theta_B/2} \int_{\beta=-\phi_B/2}^{\phi_B/2} \frac{f_A^4(\theta, \beta, \zeta) \sigma_0(\alpha) \, dx \, dy}{r^4} \quad (5.2)$$

where

$$F = f_A(\theta, \beta, \zeta) = \exp\left(-2 \ln(2) \left(\frac{\theta - \zeta}{\theta_B}\right)^2\right) \cdot \exp\left(-2 \ln(2) \left(\frac{\beta}{\phi_B}\right)^2\right) \quad (5.3)$$

Total reflected power was calculated after defining the problem on a spherical coordinate system due to the fact that the antenna beam illuminated the terrain on a conical basis which is appropriate to calculate with a spherical coordinate system. In the geometry with two-planes the intersection of the planes constitute a straight line which is more suitable to rectangular coordinate system. Reflection from *Plane-1* and *Plane-2* was calculated separately to find the total reflection from the whole terrain. Lower and upper integral limits were taken up to or down to intersection point for each plane. To take the integral in the rectangular coordinate system the clutter element was defined in rectangular coordinate system. In the rectangular coordinate system area of the clutter element was found by dx times dy . Differential distances dx and dy was calculated from Figure 5.4. The slant distances from sensor to the clutter element dA on the xy , xz and yz planes is r_{xy} , r_{xz} and r_{yz} respectively (Figure 5.3).

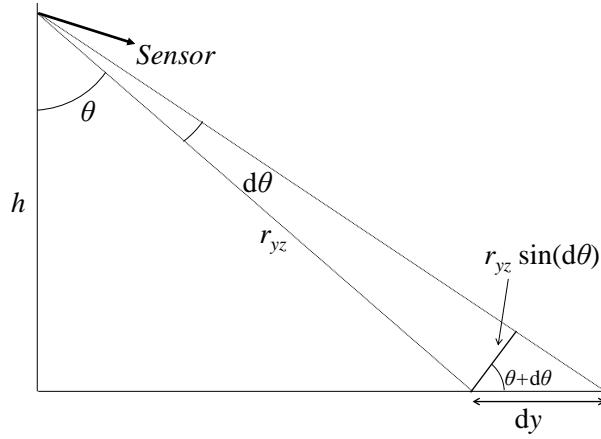


Figure 5.4: Differential Distance, dy

$$dx = \frac{r_{xz} \sin(d\beta)}{\cos(\beta + d\beta)} = \frac{r_{xz} d\beta}{\cos(\beta)} \quad (5.4)$$

$$dy = \frac{r_{yz} \sin(d\theta)}{\cos(\theta + d\theta)} = \frac{r_{yz} d\theta}{\cos(\theta)} \quad (5.5)$$

$$r_{xz} = \frac{h}{\cos(\beta)} \quad r_{yz} = \frac{h}{\cos(\theta)} \quad (5.6)$$

$$dA = dx dy = \frac{r_{xz}}{\cos(\beta)} \frac{r_{yz}}{\cos(\theta)} d\beta d\theta = \frac{h^2}{\cos^2(\beta) \cos^2(\theta)} d\beta d\theta \quad (5.7)$$

Relation between the height of the sensor and the distance of the sensor to the clutter element can be defined by:

$$r_{xy}^2 = h^2 \tan^2(\theta) + h^2 \tan^2(\beta) \quad (5.8)$$

$$r^2 = h^2 + r_{xy}^2 = h^2 + h^2 \tan^2(\theta) + h^2 \tan^2(\beta) \quad (5.9)$$

$$r = \frac{h}{\sqrt{1 + \tan^2(\theta) + \tan^2(\beta)}} \quad (5.10)$$

$$\alpha = \tan^{-1} \left(\frac{r_{xy}}{h} \right) = \tan^{-1} \left(\frac{\sqrt{h^2 \tan^2(\theta) + h^2 \tan^2(\beta)}}{h} \right) = \tan^{-1} \left(\sqrt{\tan^2(\theta) + \tan^2(\beta)} \right) \quad (5.11)$$

Using differential clutter area (5.7) and replacing r by h (5.10) in radar range equation (5.2) we got the equation for the total received power for rectangular coordinate system (5.12). For the land clutter, the grazing angle α is expressed in terms of the azimuth angle β and elevation angle θ in equation (5.11).

$$P_r = \frac{P_0 G_0^2 \lambda^2}{(4\pi)^3 h^2} \int_{\theta=\zeta-\theta_B/2}^{\zeta+\theta_B/2} \int_{\beta=-\phi_B/2}^{\phi_B/2} \frac{f_A^4(\theta, \beta, \zeta) \sigma_0(\alpha)}{[1 + \tan^2(\theta) + \tan^2(\beta)]^2 \cos^2(\theta) \cos^2(\beta)} d\theta d\beta \quad (5.12)$$

5.1.2 Simulation (Double-Plane Terrain)

The simulation used for flat-terrain was modified to calculate the received power and Doppler shift from the double plane terrain. Grazing angle of the second plane α and the off-set distance ($y_s - y_0$) between projection of the sensor's tip coordinate to the Plane-1 and the intersection point of two planes can be set as a parameter in the simulation to define the terrain (Figure 5.5).

Calculation of Received Power

The received power reflected from the double-terrain was calculated using (5.12). The integral was separated to two pieces to calculate the returns from each plane. For the first region the integral limit L1 and for the second region the integral limit L2 is shown in Figure 5.5.

While we defined the total received power on a rectangular basis we can easily calculate the return power from double-plane by splitting the integral into two. If the total received power formulation was based on circular coordinate system as in flat-terrain it was not possible to calculate the total return from double-plane structure.

Calculation of Doppler Shift

While we estimate the height of the sensor we use the Doppler shift information as the temporal variation of the height. Whenever two surfaces is exists there will be two Doppler maxima from each planes. Neglecting the antenna pattern we can roughly assume that the sensor measure the Doppler shift from Plane-1 when it is on Region-1 and from Plane-2 when it is on

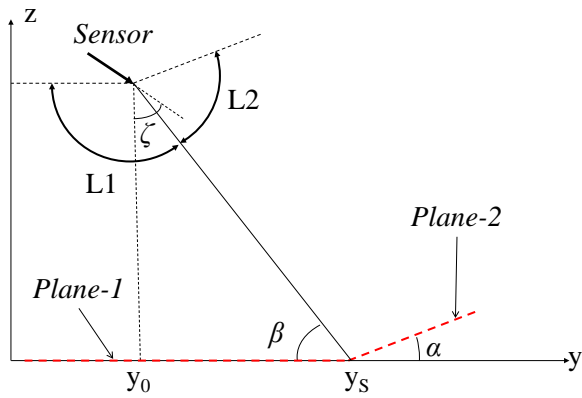


Figure 5.5: Integral Limits for Calculating Return Power from Double-Plane Terrain

Region-2. The border of the Region-1 and Region-2 is defined as the plane dividing the whole region into two equal pieces over the planes as shown in Figure 5.6.

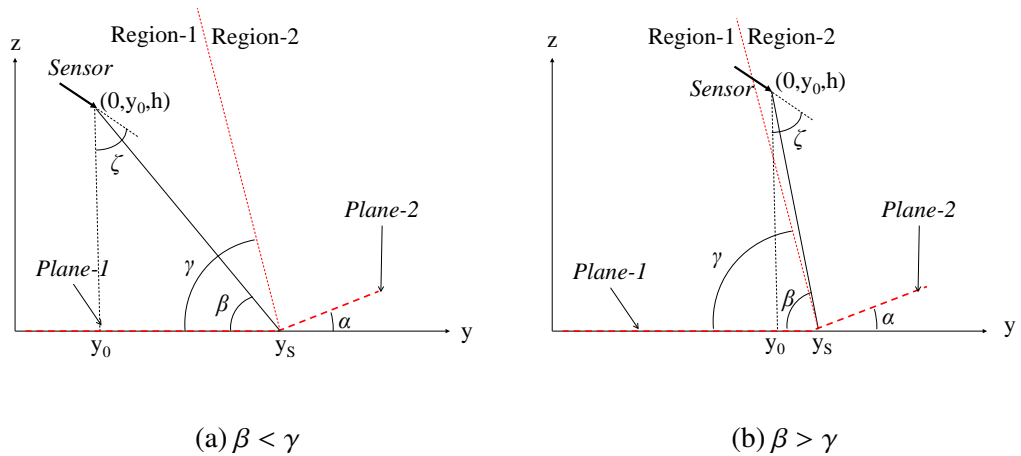


Figure 5.6: Intersection Regions between Plane-1 and Plane-2, (a) Sensor is in Region-1, (b) Sensor is in Region-2

Figure 5.6.(a) shows when the sensor is in the first region (case-1) and Figure 5.6.(b) shows when the sensor is in the second region (case-2). For the power spectral density of the Doppler signal two factors play major role, one is the angle of reflection (grazing angle) and the other is the distance of the reflecting surface. The peak power of the Doppler spectrum occurs due to the reflection from the nearest point on the surface when the sensor is looking towards the surface as shown in Figure 3.4. While we defined two cases for the sensor, one is when the sensor is on the Region-1 and the other is on the Region-2, the nearest point from the surface

to the sensor in case-1 is from the Plane-1 and in case-2 from the Plane-2 (Figure 5.7).

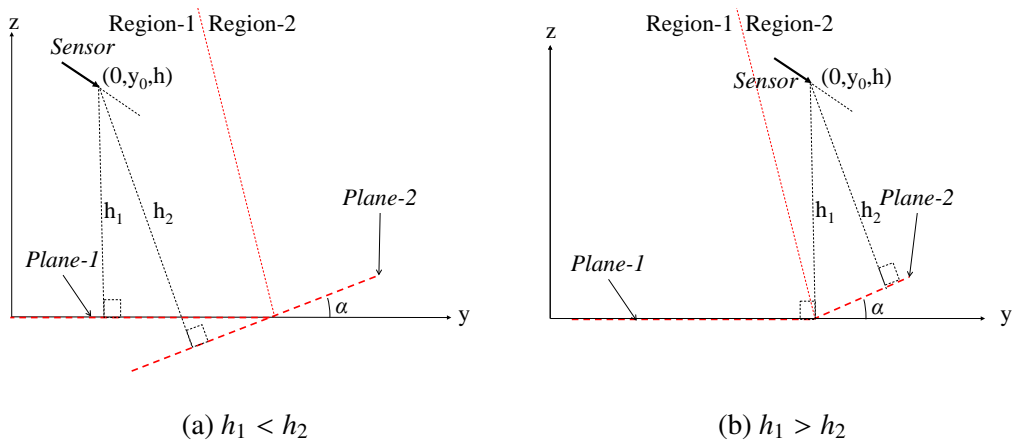


Figure 5.7: Intersection Regions between Plane-1 and Plane-2, (a) Sensor is in Region-1 (b) Sensor is in Region-2

In the first case the peak Doppler power results from Plane-1 ($h_1 < h_2$) and in the second case peak power results from Plane-2 ($h_1 > h_2$). So in the simulation the Doppler shift from the first plane is used in case-1 and the Doppler shift from the second plane is used in case-2. Therefore a vivid change in the vertical velocity occurs when the sensor passes from first region to the second region.

5.1.3 Simulation Results (Double-Plane Terrain)

This approach is shown to be useful for flat surfaces. This method is still applicable when the reflections come from two planar surfaces as shown in Figure 5.1.

The estimation and corrected estimation for sensor's height relative to terrain is calculated with the same method and the result is given in Fig. 5.8. The peak amplitude of the Doppler shift occurs from the nearest point from sensor to the plane (terrain). The peak amplitude of the Doppler shift occurs due to the reflections from Plane-1 if h_1 (the nearest distance from sensor to the Plane-1) is shorter than h_2 . If h_1 is longer than h_2 the peak amplitude occurs due to the Plane-2. Regarding the sensor position, h_1 is shorter than h_2 initially and the vertical velocity is calculated according to Plane-1 using the Doppler shift information. When h_2 becomes shorter than h_1 , the peak amplitude return occurs from Plane-2 and the vertical velocity is calculated according to the Plane-2. This sudden change in the highest Doppler

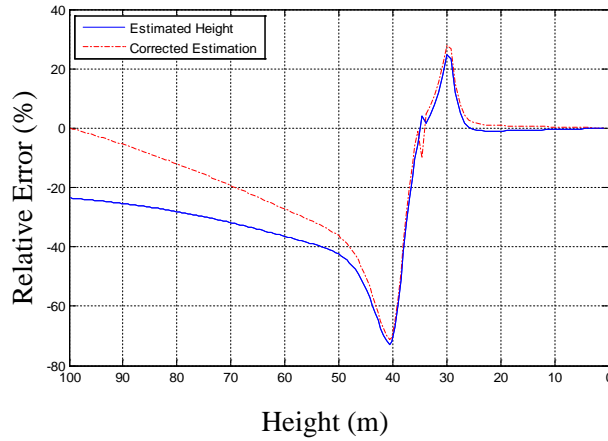


Figure 5.8: Estimation Error for a Two-Plane Terrain ($h_0 = 100$ m, $v_0 = 200$ m/s, and $\zeta_0 = 60^\circ$)

frequency causes a sharp change in estimation (between 50 to 25 meters).

The sudden change in the highest Doppler frequency is expected to occur earlier if the sensor is moved towards the intersection of Region-1 and Region-2 as shown in Figure 5.9.

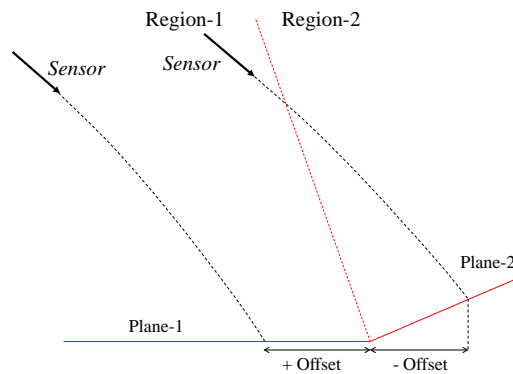


Figure 5.9: Off-Set Distances from the Impact Points

Position of the sensor was shifted towards the intersection between Region-1 and Region-2 by an off-set distance. While the sensor passes through Region-1 to Region-2 the peak errors in the height estimation occurs. For different off-set distances height estimation results are given in Figure 5.10.

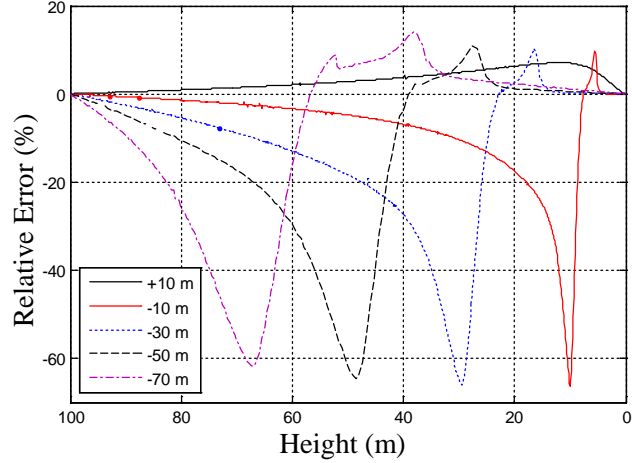


Figure 5.10: Estimation Results for Different Off-Set Distances ($h_0 = 100$ m, $v_0 = 200$ m/s, and $\zeta_0 = 60^\circ$)

5.2 Simulation for a Terrain which is Generated by DTED

The theory is shown to be effective for flat-terrain and double-plane terrain. To analyse the performance of the sensor over realistic terrain we need to calculate the received power and Doppler shift spectrum over the realistic terrain. Digital Terrain Elevation Data (DTED) can be easily used to generate a sample realistic terrain. We need to manipulate DTED to find the total reflected power and Doppler shift spectrum. DTED is only used to generate digital terrain data.

5.2.1 Digital Terrain Elevation Data (DTED) Structure

Digital Terrain Elevation Data (DTED) is a standard for terrain elevation values of National Imagery and Mapping Agency (NIMA) [37]. DTED was used to simulate the terrain in our study (Figure 5.11). The terrain elevation information is expressed in meters and by the intersections of rows and columns within the elevation data matrix the position of the data point is calculated. Theoretical range of elevations are between $\pm 32,767$ meters and in practice the elevation values are between $+9,000$ meters to $-12,000$ meters. *Horizontal Datum* is the World Geodetic System (WGS 84). and *Vertical Datum* is the Mean Sea Level (MSL) as determined by the Earth Gravitational Model (EGM) 1996. While the simulation used the DTED data as a sample terrain the reliability of the World Geodetic System or the elevation data is not important. DTED files consist of several files and the data file includes the elevation information

of the related position. DTED has three levels of detail in use:

- DTED Level 0 has a resolution of approximately 900 meters,
- DTED Level 1 has a resolution of approximately 90 meters and
- DTED Level 2 has a resolution of approximately 30 meters between adjacent data points.

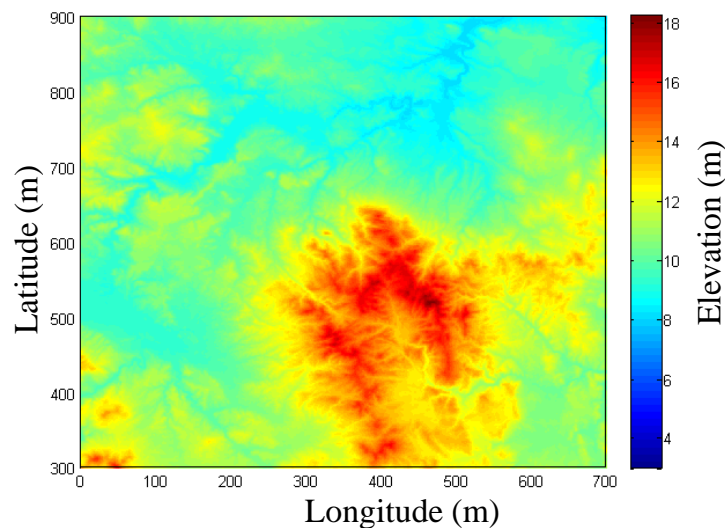


Figure 5.11: Sample Digital Terrain Elevation Data

A data file of DTED is a 1° by 1° cell defined by latitudes and longitudes of a geographic reference system regardless of the level. The “.dt0”, “.dt1”, and “.dt2” file extensions in a DTED file cluster are the elevation data files for DTED Level 0, Level 1 and Level 2, respectively. DTED specifications vary by the region of interest and are divided into groups by the latitude of the region (Table 5.1).

We used the DTED data for the region 0° - 50° in northern hemisphere but the distance of 1° of latitude and longitude assumed to be the same. The resolution of a m by n elevation data file varies by the total number of the data points in one degree of latitude (m) and one degree of longitude (n) (5.13).

Table 5.1: Matrix Intervals for DTED

					Data Spacing (seconds)			
		Zone	Latitude		Latitude	Longitude		
DTED-0	I	0°	-	50°	North-South	30	×	30
	II	50°	-	70°	North-South	30	×	60
	III	70°	-	75°	North-South	30	×	90
	IV	75°	-	80°	North-South	30	×	120
	V	80°	-	90°	North-South	30	×	180
DTED-1	I	0°	-	50°	North-South	3	×	3
	II	50°	-	70°	North-South	3	×	6
	III	70°	-	75°	North-South	3	×	9
	IV	75°	-	80°	North-South	3	×	12
	V	80°	-	90°	North-South	3	×	18
DTED-2	I	0°	-	50°	North-South	1	×	1
	II	50°	-	70°	North-South	1	×	2
	III	70°	-	75°	North-South	1	×	3
	IV	75°	-	80°	North-South	1	×	4
	V	80°	-	90°	North-South	1	×	6

$$\begin{array}{c}
 \text{Total elevation points in one degree of latitude} \\
 \mathbf{D}_{m \times n} = \begin{bmatrix} d_{11} & d_{12} & \dots & d_{1n} \\ d_{21} & d_{22} & \dots & d_{2n} \\ \vdots & \vdots & \ddots & \vdots \\ d_{m1} & d_{m2} & \dots & d_{mn} \end{bmatrix} \quad (5.13)
 \end{array}$$

DTED elevation data cover 1° of latitude and longitude and the resolution is defined by the total number of cells in 1° of latitude (cell size is the same for latitudinal direction, or vice versa). The spatial reference is the Northern Latitude Limit and Western Latitude Limit defined in the reference vector (Figure 5.12).

The reference file associated with the DTED data file is an a three by one reference vector ($\mathbf{V}_{Reference}$). The first element is the total number of cells within 1° of latitude or longitude (cells/degree), the second element is the Northern Latitude Limit and the third element is the Western Latitude Limit (5.14). To convert latitude and longitude information in units of metres; distance between two consecutive latitude and longitude lines (1°) was assumed to be constant (111194.9 metres). Reference vector is used to determine the resolution and the

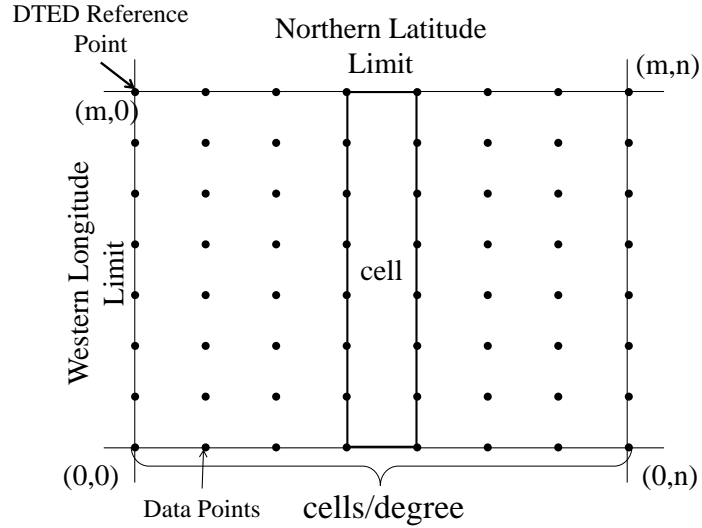


Figure 5.12: Sample Structure for a 7 Cell DTED Data

geographical position of the DTED. To convert latitude longitude information of DTED to any element in the matrix requires to use of the whole reference vector information.

$$V_{Reference} = [(cells/degree) \quad Northern \text{ Latitude Limit} \quad Western \text{ Longitude Limit}] \quad (5.14)$$

5.2.2 Simulation (DTED Terrain)

In our study DTED was used to simulate the terrain. While the DTED used in the simulation just for a terrain model the latitude and longitude limits and the reliability of the elevation data was not essential. The Northern Latitude Limit was taken as 1200 meters (and was converted to the units of degrees) initially and The Southern Latitude Limit was taken as 0. The Western Longitude Limit was taken as zero, and The Eastern Longitude Limit was taken as 1200 meters (and was converted to the units of degrees). The conversion was conducted using (5.15) and (5.16).

$$\text{latitude} = \frac{(x_0 + x)}{111,194.9} \quad \{x \text{ in meters}\} \quad (5.15)$$

$$\text{longitude} = \frac{(y_0 + y)}{111,194.9} \quad \{\text{y in meters}\} \quad (5.16)$$

Relevant problem with the use of DTED in the simulation can be summarized by:

- Spatial Resolution:

The worst resolution is approximately 900 meters and with DTED Level 2 resolution is 30 meters at best. The region of interest in the sensor is less than 50 meters and while the sensor approach to the terrain the resolution of the terrain is insufficient for calculations and discrimination.

- Latitude and Longitude Limits:

DTED matrix represent the elevation within a region of 1° by 1° cell defined by latitudes and longitudes. The number of the cells per degree is the resolution of DTED. To calculate the return power from such a large area is unnecessary in many cases. To have a smaller area than 1° by 1° needs matrix manipulation.

For different positions of the sensor different resolution in DTED was used in the simulation (regarding to the height of the sensor) to lessen the calculation load. The majority of the calculation load is the determination of the visibility of the elevation points from the sensor position. For visibility the MATLAB™'s command "*viewshed*". *viewshed* command computes points visible from a point on a digital elevation data grid. The sensor position was provided to *viewshed* command as latitude and longitude in units of degrees. So the position of the sensor which is defined as *x,y in units of meters* was converted to *latitude and longitude in units of degrees*. The visibility map then contains ones at the positions visible from the sensor location, and zeros where the line of sight is obscured by terrain (Figure 5.13). While the position of the sensor in *viewshed* is in units of degrees we converted the position of the sensor (x,y) in units of meters to (latitude, longitude) in units of degree. Regardless of the spatial position of the DTED on the World 1 degree of latitude and longitude was assumed to be 111,194.9 kilometres for conversion purposes.

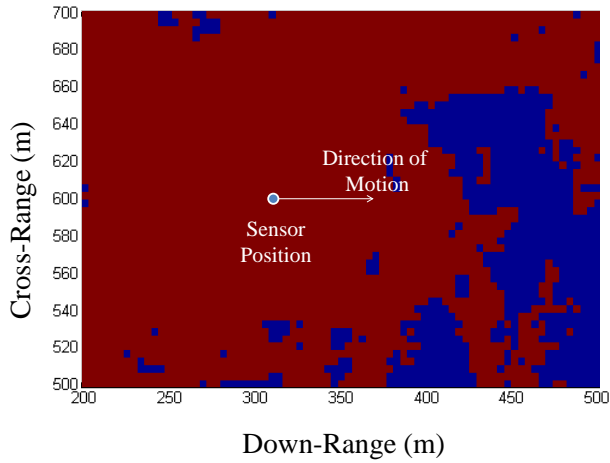


Figure 5.13: Sample Visibility Map Generated by MATLAB™

5.2.2.1 Triangulation of DTED

Using the visibility map calculated by *viewshed* triangulation of the elevation data was calculated to set-up the patches of the terrain. Numbering of the vertices of patches is shown in Figure 5.14.

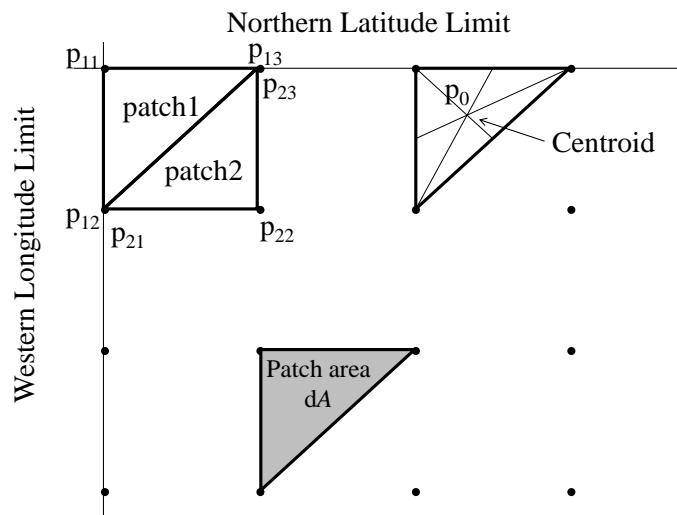


Figure 5.14: Triangulation Structure of the DTED Matrix

The visible elevation points (posts) from the sensors current position were calculated using *viewshed* and while a data point was obscured or shadowed the related patches with that point undermined. It was possible to undermine the patch whenever at least one point related to that

patch was invisible (obscured or shadowed) or at least two points related to that patch were invisible and the triangulation code (A.3.4) eliminates any patch in the first case. An example of the triangulation process with two posts are invisible is given in Figure (5.15).

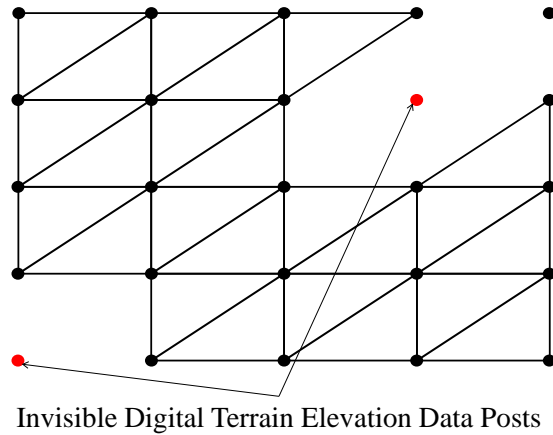


Figure 5.15: Triangulation of DTED with Two Invisible Posts

The triangulation was based on the grid triangulation which is easier to implement. The result after applying the grid triangulation and normal vector calculation for a sample terrain is given in Figure 5.16.

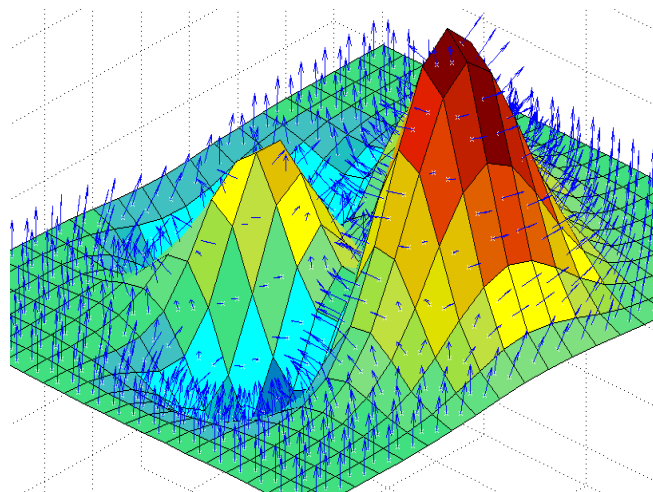


Figure 5.16: Surface Normals Located at Patch Centroids after Triangulation for a Sample Terrain

5.2.2.2 Calculation of Parameters

In the simulation DTED-1 file which has a resolution approximately 90 meters. The distance between two consecutive data posts were translated as 1 meter in the simulation as the data used as a random terrain. Therefore, the highest resolution was 1 meter per each cell. A single DTED-2 type file has 1201 by 1201 data posts (which actually covers 1 degree of latitude and longitude) corresponds to 90 meters of separation and the separation was translated as 1 meter resulting a total of 1200 meters by 1200 meters area. Total number of data posts were 1.442.401. The triangulation and the calculation of reflection parameters such as return power and Doppler frequency were calculated in a short time but to find the visible points from the sensor position using *viewshed* command last longer to execute compared to calculation of parameters.

To calculate the totalpower received from the terrain generated using DTED; area, normal vector, distance vector from sensor to the patch, the angle between sensor antenna bore-sight axis and distance vector to calculate the antenna pattern effect and grazing angle for each triangle clutter element patch (dA) were calculated (Figure 5.17).

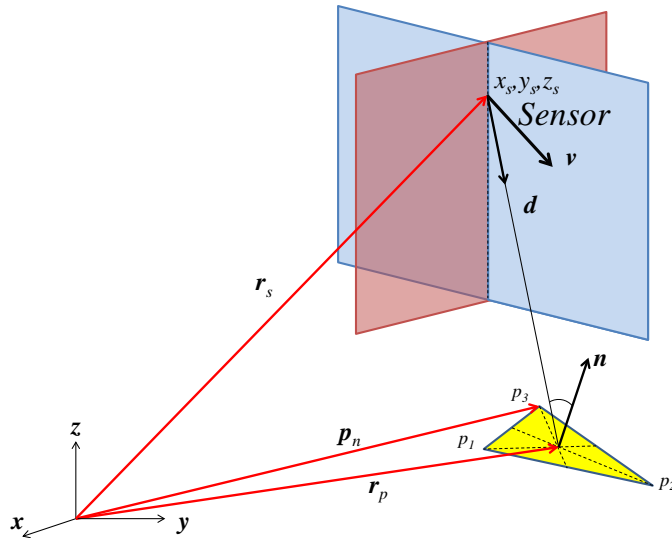


Figure 5.17: Vectors for Sensor and the Clutter Patch

$p_1(x, y)$, $p_2(x, y)$ and $p_3(x, y)$ are the positions of the three corners of the patch on $x - y$ axis and $Z(p_1)$, $Z(p_2)$ and $Z(p_3)$ are the elevation of the each corner of a patch where position vector of the n^{th} corner \vec{p}_n is

$$\vec{p}_n = p_n(x) \cdot \hat{a}_x + p_n(y) \cdot \hat{a}_y + Z(p_n) \cdot \hat{a}_z \quad (5.17)$$

Let \vec{r}_s be the position vector and \hat{v} be the direction vector of the sensor and \vec{r}_p be the patch position vector which is the centroid of the triangle

$$\hat{v} = \hat{v}_x + \hat{v}_y + \hat{v}_z = \frac{v_x}{|\vec{v}_0|} \cdot \hat{a}_x + \frac{v_y}{|\vec{v}_0|} \cdot \hat{a}_y + \frac{v_z}{|\vec{v}_0|} \cdot \hat{a}_z \quad (5.18)$$

where the initial velocity vector of the sensor is $\vec{v}_0 = v_x \cdot \hat{a}_x + v_y \cdot \hat{a}_y + v_z \cdot \hat{a}_z$.

$$\vec{r}_p = \frac{p_1(x) + p_2(x) + p_3(x)}{3} \cdot \hat{a}_x + \frac{p_1(y) + p_2(y) + p_3(y)}{3} \cdot \hat{a}_y + \frac{Z(p_1) + Z(p_2) + Z(p_3)}{3} \cdot \hat{a}_z \quad (5.19)$$

The normal vector \hat{n} of the triangle patch is

$$\hat{n} = \vec{u} \times \vec{v} = (\vec{p}_3 - \vec{p}_2) \times (\vec{p}_1 - \vec{p}_2) = \det \begin{vmatrix} \hat{a}_x & \hat{a}_y & \hat{a}_z \\ u_x & u_y & u_z \\ v_x & v_y & v_z \end{vmatrix} \quad (5.20)$$

The distance vector \vec{d} from the sensor to the triangle patch centroid is

$$\vec{d} = \vec{r}_p - \vec{r}_s \quad (5.21)$$

The angle decline from the antenna bore-sight is β and the grazing angle is α . Angle α was found from the negative of the dot product of the normal vector of the patch \hat{n} and the distance vector \vec{d} . The decline angle was calculated by the dot product of the velocity vector \hat{v} of the sensor and the unit vector \hat{d} of distance vector \vec{d} (Figure 5.18).

$$\alpha = -\hat{n} \cdot \hat{d} = -\hat{n} \cdot \frac{\vec{d}}{|\vec{d}|} \quad \beta = \hat{v} \cdot \hat{d} = \hat{v} \cdot \frac{\vec{d}}{|\vec{d}|} \quad (5.22)$$

Then the area of the triangle patch (dA_p) was calculated by the cross product of the adjacent edges of the patch referencing with the right hand rule.

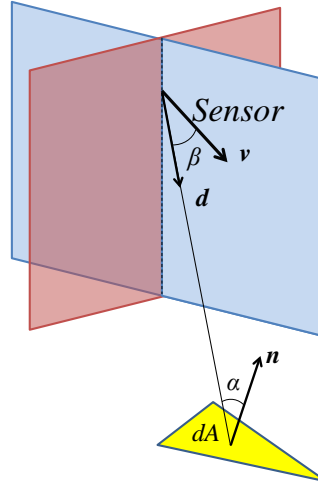


Figure 5.18: Grazing and Bore-sight Decline Angles for a Clutter Patch

$$dA_p = \frac{1}{2} \sqrt{\left| \det \begin{pmatrix} p_1(x) & p_2(x) & p_3(x) \\ p_1(y) & p_2(y) & p_3(y) \\ 1 & 1 & 1 \end{pmatrix} \right|^2 + \left| \det \begin{pmatrix} p_1(y) & p_2(y) & p_3(y) \\ Z(p_1) & Z(p_2) & Z(p_3) \\ 1 & 1 & 1 \end{pmatrix} \right|^2 + \left| \det \begin{pmatrix} Z(p_1) & Z(p_2) & Z(p_3) \\ p_1(x) & p_2(x) & p_3(x) \\ 1 & 1 & 1 \end{pmatrix} \right|^2} \quad (5.23)$$

The received power reflected back from the clutter patch element at the sensor is calculated using (3.2).

$$dP_r = \frac{P_0 G_0^2 \lambda^2 F^4(\beta) \sigma_0(\alpha) dA_p}{(4\pi)^3 |\vec{d}|^4} \quad (5.24)$$

Assuming the antenna beam-widths are equal both for the elevation and azimuth ($\theta_B = \phi_B$) with a circular symmetry then the equation (3.49) becomes

$$F(\beta) = \exp\left(-2 \ln(2) \left(\frac{0.5\beta}{\theta_B}\right)^2\right) \quad (5.25)$$

The terrain was assumed to have a uniform reflectivity (clutter) over the area of interest. By using DTED patches each patch can be assigned to a different reflection coefficient and by doing so complex terrain types can be simulated.

5.2.2.3 Simulation GUI

A MATLAB™ GUI is programmed to calculate the Return Power and Doppler Shift Spectrum from the terrain which is generated by DTED (Figure 5.19).

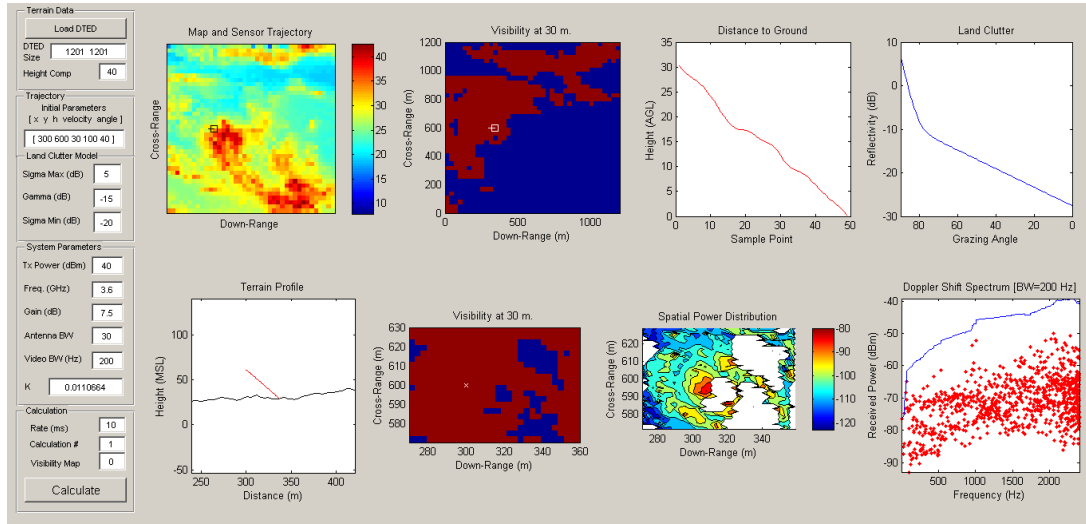


Figure 5.19: Graphical User Interface of Simulation which is Calculating Parameters for DTED Generated Terrain

Visible points from the sensor point of view, power return and Doppler shift frequency from each patch was calculated by the simulation.

5.2.3 Simulation Results (DTED Terrain)

Two main outputs of the simulation are the Power Spectrum and Frequency Spectrum of the Doppler Shift. The spectral density of the reflected signal at the receiver was directly calculated by the reflections from each clutter element patch dA_p on the DTED terrain. The calculated power spectrum by the simulation for a flat terrain generated from DTED and the relation of the spectrum components with respect to the terrain is shown in Figure 5.20. Return power from each patch is represented by a red dot in the spectrum.

The results for return power for a sensor located 300 m above the terrain is given in Figure 5.21. In Figure 5.21.(a) the sensor is tilted 30° down ($\zeta = 60^\circ$) from the horizon and in Figure 5.21.(b) the sensor is down-looking ($\zeta = 0^\circ$) towards the terrain.

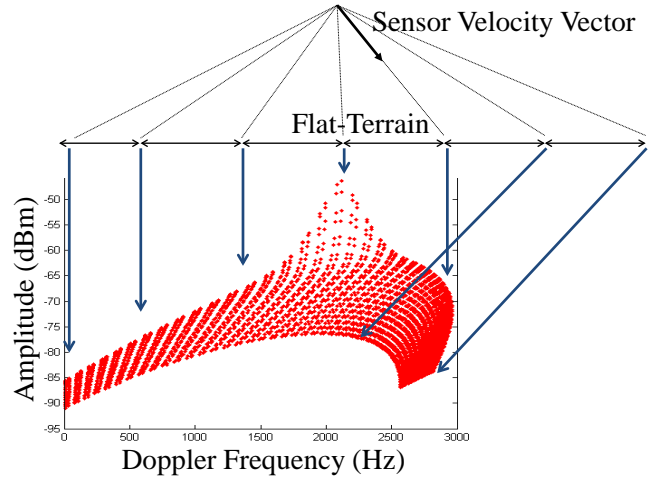


Figure 5.20: Relation of Doppler Spectrum with Terrain

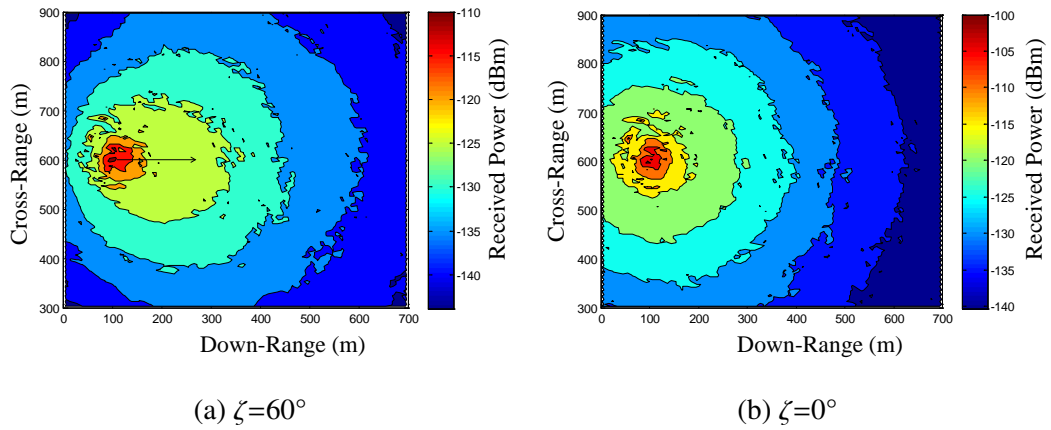


Figure 5.21: Effect of Tilt Angle on to the Received Power

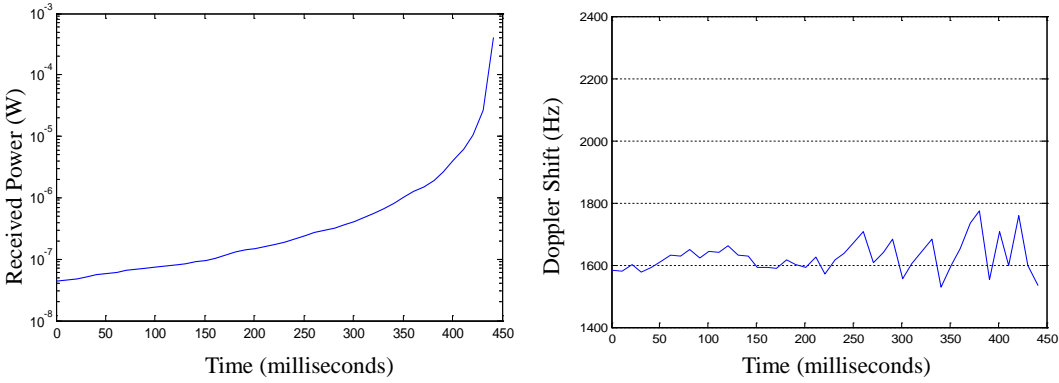
The received power and Doppler shift obtained with a 10 ms sampling rate for a flat terrain was calculated using the DTED simulation. The parameters are given in Table 5.2.

Table 5.2: Release Parameters for DTED Simulation

Release height	30 m	Transmitted power	33 dBm	Frequency	3.6 GHz
Release velocity	100 m/s	Antenna gain	7.5 dB	Sampling Rate	10 ms
Release angle	40°	Antenna beamwidths	30°	Terrain	Wooded

Received power for the sample simulation is given in Figure 5.22.(a) and the Doppler shift is given in Figure 5.22.(b). The ripples observed at the Doppler shift is caused by low DTED resolution. In the simulation 1×1m DTED was used. For lower heights especially when the

sensor gets closer to the ground the low relative resolution of the DTED causes calculation errors.



(a) Received Power at the Antenna Port

(b) Doppler shift

Figure 5.22: Simulation Result for Parameters Given in Table 5.2

The estimated height is given in Figure 5.23. While the estimation was calculated for a flat terrain the relative error is expected to be less. However the low resolution of DTED cause calculation errors. The derivative of the received voltage is sensitive to the errors in the received voltage thus small variations of the received voltage causes large estimation errors.

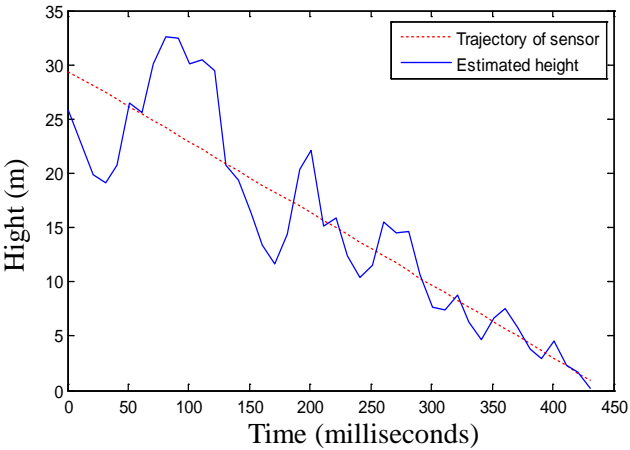


Figure 5.23: Estimation Result for Parameters Given in Table 5.2

5.3 Doppler Shift Spectrum

The reflected power and Doppler shift were calculated for a sensor released from 30 meters Above Ground Level (AGL) with an initial velocity of 100 m/s and the release angle is 50°. The beamwidths both in azimuth and elevation were 30°. Three different terrain profiles are given in Figure 5.24. In case-1 the nearest distance from sensor to the ground is at the 40° and two surfaces facing towards the sensor at 50° and 60° down the sensor as seen in Figure 5.25. In case-2 the same terrain is extruded and still the nearest distance from sensor to the ground is at the 40° and two surfaces facing towards the sensor at 50° and 60° down the sensor. In case-3 the terrain is extruded more than case-1 and case-2.

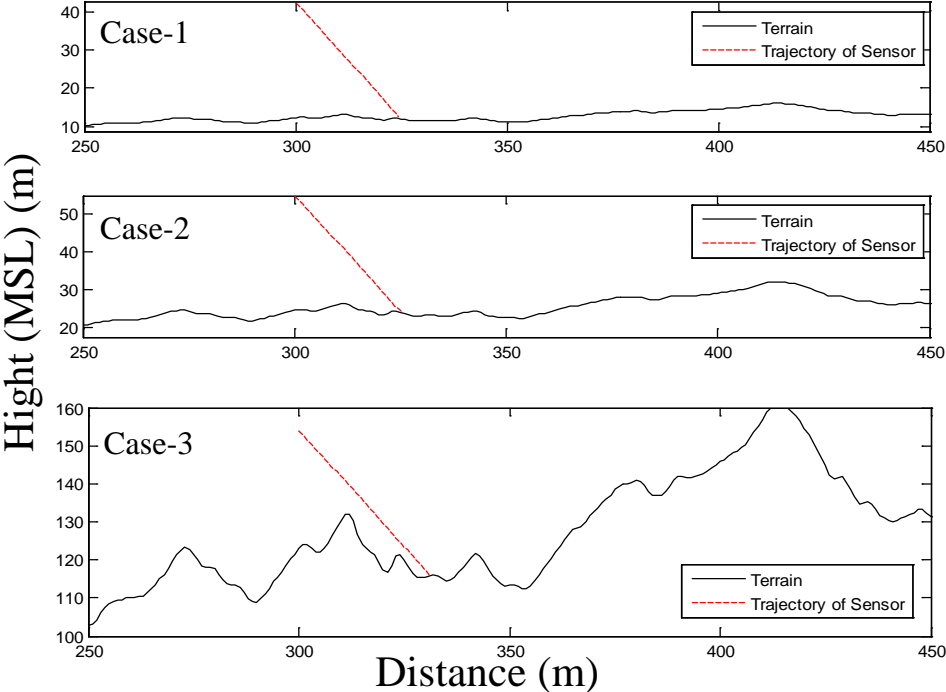


Figure 5.24: Same Terrain Profile with Three Different Heights

When the resulting echo signal is analysed the highest power density of the Doppler shift occurs due to the nearest distance for case-1 and case-2. In case-1, the maximum Doppler shift in power density occurs at the frequency which is -0.8 times the maximum Doppler shift. The maximum frequency of the Doppler shift is 2400 Hz according the sensor velocity ($v_0 = 100$ m/s and $f_0 = 3.6$ GHz). The shift with the maximum power density corresponds approximately to a 37° off-set from the sensor direction which is the result of the reflection

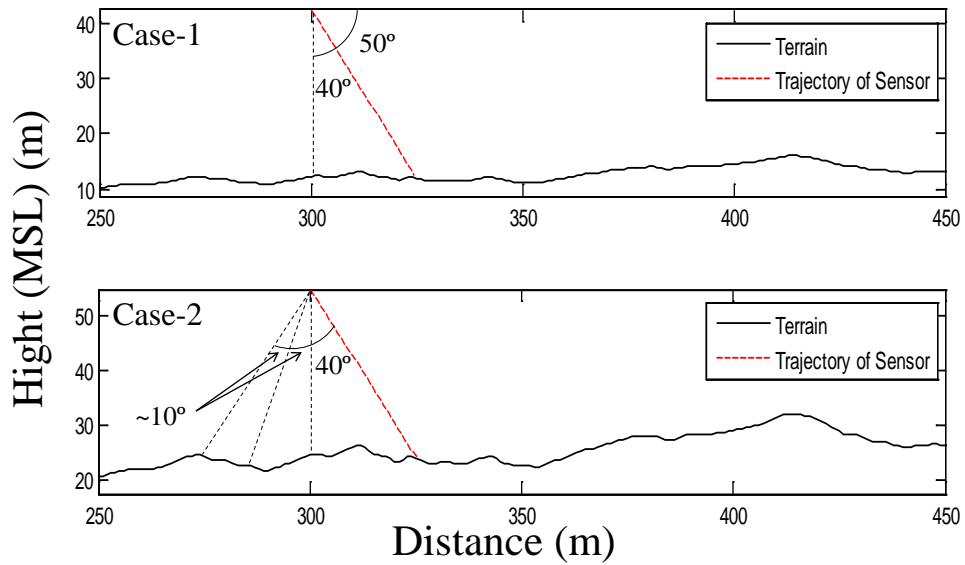


Figure 5.25: Angles between the Sensor and Terrain

from the nearest point. The nearest point is located approximately 40° off-set from the sensor direction for case-1 and case-2. In case-2 when the terrain height is increased two more maxima of the power density occurs at 50° and 57° off-sets from the sensor direction as expected (Figure 5.26).

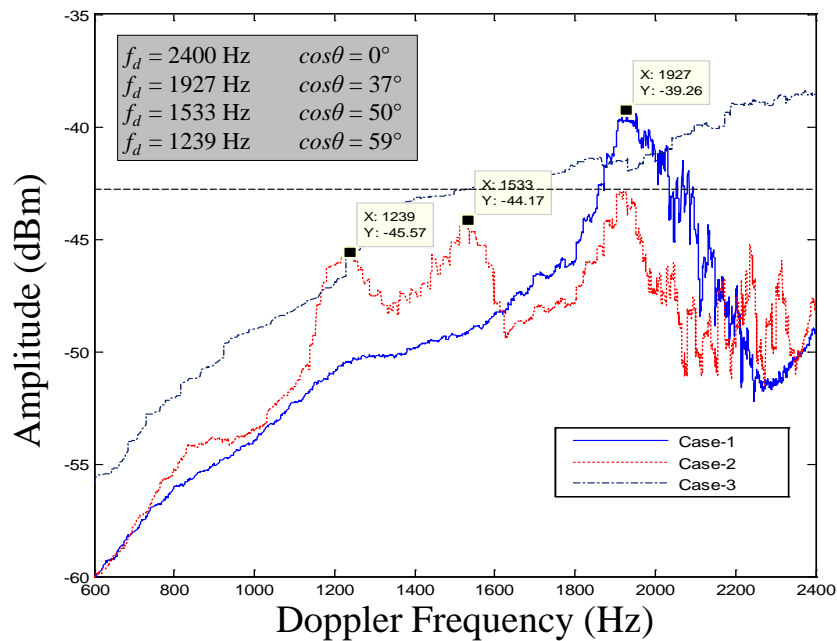


Figure 5.26: Doppler Shift Spectrum for Terrain Profiles given in Figure 5.24

In case-3, while the height of the terrain is increased more the faces of the terrain looking

to the sensor are also increased at the bore-sight direction. The increase in the area of the bore-sight patches over the terrain results maximum peak to occur at the bore-sight of the sensor. The results shows that the information of the terrain roughness is an important factor effecting the power density of the Doppler shift spectrum. From the Doppler spectrum obtained from various terrains shows that it is not a straightforward task to make a conclusion for determining the maximum power density of the Doppler shift spectrum directly from terrain information. Therefore, conditions when the return signal from a side patch is higher than the return signal from the bore-sight patch was analysed in Section 5.4.

5.4 Return Power from a Side Patch

The geometry of the two patches (one is the bore-sight and the other is the side patch) is given in Figure 5.27.

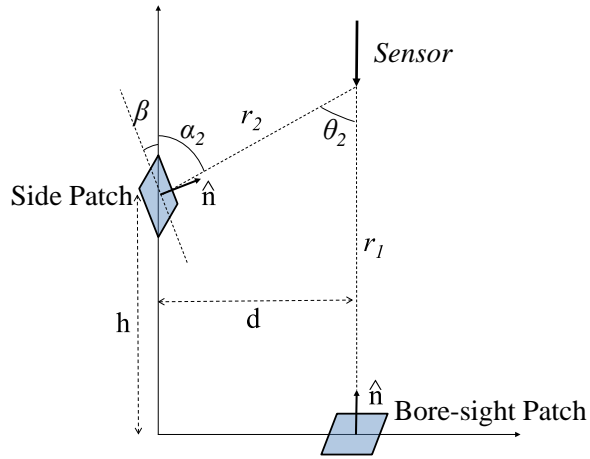


Figure 5.27: Two Patch Geometry

In the case of two patches, the power density of the return signal for the side patch is greater than the power density from the bore-sight patch when the condition (5.26) is satisfied.

$$dP_{r_1} < dP_{r_2} \Rightarrow \frac{P_0 G_0^2 \lambda^2 F^4(\theta_1, \phi_1, \zeta) \sigma_0(\alpha_1) dA_1}{(4\pi)^3 r_1^4} < \frac{P_0 G_0^2 \lambda^2 F^4(\theta_2, \phi_2, \zeta) \sigma_0(\alpha_2 + \beta) dA_2}{(4\pi)^3 r_2^4} \quad (5.26)$$

It was assumed that;

- Two patches have the same identical area ($dA_1 = dA_2$) and clutter properties (Figure 5.28)
- The first patch (bore-sight patch) is located directly in front of the sensor axis ($\zeta = \theta_1 = \phi_1 = 0$) and the first patch's normal is directed towards the sensor ($\alpha_1 = 0$),
- The two patches lie on the elevation axis ($\phi_2 = 0$).

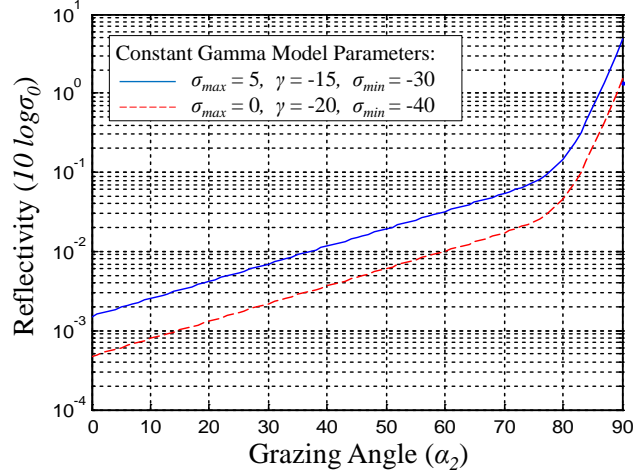


Figure 5.28: Patch Clutter Model

Deriving the equation (5.26) we get the condition (5.27) for the distances of the patches relative to the sensor axis.

$$r_2 < r_1 \frac{F(\theta_2, \phi_2, \zeta)}{F(\theta_1, \phi_1, \zeta)} \sqrt[4]{\frac{\sigma_0(\alpha_2)}{\sigma_0(\alpha_1)}} \quad (5.27)$$

$$F(\theta, \phi, \zeta) = \exp\left(-2 \ln(2) \left(\frac{\theta}{\theta_B}\right)^2\right) \cdot \exp\left(-2 \ln(2) \left(\frac{\phi}{\phi_B}\right)^2\right) \quad (5.28)$$

$$r_2 = \frac{d}{\sin(\alpha_2)} \quad r_1 = h + \frac{d}{\tan(\alpha_2)} \quad (5.29)$$

$$\frac{r_2}{r_1} = \frac{d}{\sin(\alpha_2)} \frac{1}{h + \frac{d}{\tan(\alpha_2)}} = \frac{d \sin(\alpha_2)}{h \sin(\alpha_2) + d \cos(\alpha_2)} \quad (5.30)$$

$$\frac{d \sin(\alpha_2)}{h \sin(\alpha_2) + d \cos(\alpha_2)} < \frac{\exp\left(-2 \ln(2) \left(\frac{\theta_2}{\theta_B}\right)^2\right) \cdot \exp\left(-2 \ln(2) \left(\frac{\phi_2}{\phi_B}\right)^2\right)}{\exp\left(-2 \ln(2) \left(\frac{\theta_1}{\theta_B}\right)^2\right) \cdot \exp\left(-2 \ln(2) \left(\frac{\phi_1}{\phi_B}\right)^2\right)} \sqrt[4]{\frac{\sigma_0(\alpha_2 + \beta)}{\sigma_0(\alpha_1)}} \quad (5.31)$$

$$\frac{d \sin(\alpha_2)}{h \sin(\alpha_2) + d \cos(\alpha_2)} < \underbrace{\exp\left(-2 \ln(2) \left(\frac{\alpha_2}{\theta_B}\right)^2\right)}_{G(\alpha, \beta, \theta_B)} \sqrt[4]{\frac{\sigma_0(\alpha_2 + \beta)}{\sigma_0(0)}} \quad (5.32)$$

Finally, the condition for the return power density from patch-2 exceeds the return from the patch-1 is found by the ratio of the distances of the patches to the sensor (5.33). As an example, for the side patch (patch-2) return power density is greater than the return power density of the bore-sight patch (patch-1) if ratio d/h is smaller than the values in Figure 5.29.

$$\frac{d}{h} < \frac{\sin(\alpha_2)G(\alpha_2, \beta, \theta_B)}{\sin(\alpha_2) - \cos(\alpha_2)G(\alpha_2, \beta, \theta_B)} \quad (5.33)$$

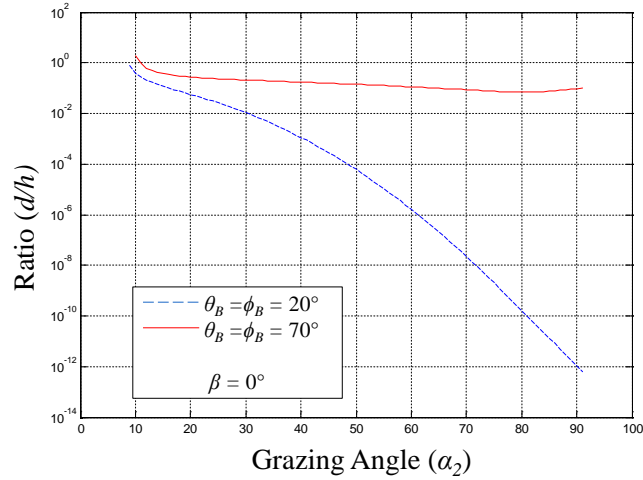


Figure 5.29: Ratio d/h vs Grazing Angle (α_2)

The return power density of the side patch will be greater than the return power density from the bore-sight patch if the ratio of d/h is smaller than the value given in Figure 5.30 for different patch tilt angles (β). This condition is satisfied only for specific grazing angles (α_2).

The ratio of d/h is obviously much more smaller for an antenna with narrower beam compared with a larger beam antenna as shown in Figure 5.29 and 5.30. Different reflectivity values (patches are identical) does not effect the ratio considerably as shown in Figure 5.31. For

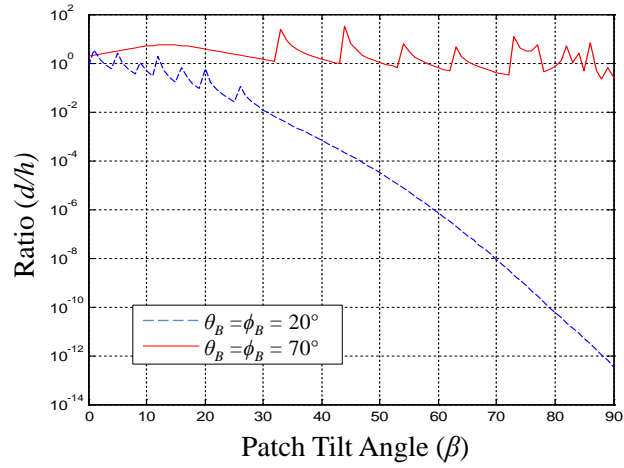


Figure 5.30: Ratio d/h vs Patch Tilt Angle for Different Antenna Beamwidths

non-identical patches the condition (5.34) was used for calculations, σ_{01} and σ_{02} which are the reflectivity of bore-sight and side patches, respectively.

$$r_2 < r_1 \frac{F(\theta_2, \phi_2, \zeta)}{F(\theta_1, \phi_1, \zeta)} \sqrt[4]{\frac{\sigma_{02}(\alpha_2)}{\sigma_{01}(0)}} \quad (5.34)$$

The result for non-identical and identical patches is given Figure 5.31 and 5.32.

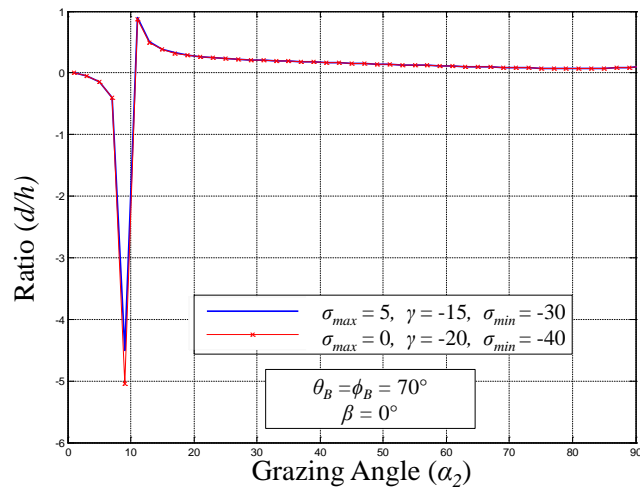


Figure 5.31: Effect of Reflectivity on Ratio (Identical Patches)

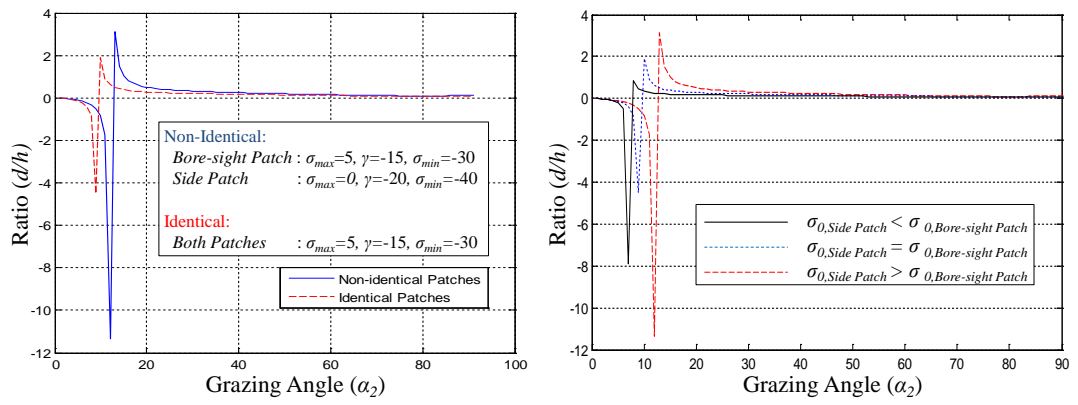


Figure 5.32: Effect of Reflectivity on Ratio

CHAPTER 6

CONCLUSION

6.1 Height Estimation Method

Use of radio waves is a very common choice for proximity fuzes. The stand-off distance for fuzes varies between a lower and an upper limit depending on the electromagnetic reflectivity of terrain (target). If the reflectivity of the terrain is comparably higher, the return power at the receiver reaches to the threshold level more quickly and the stand-off distance increases. This dissertation introduces an approach to estimate the height of airborne ballistic platforms more precisely compared to the conventional fuzes regardless of the reflection properties of the terrain. Independent measurements of the rate of change of voltage from the receiver and the rate of change of height (from Doppler shift) allow the height to be estimated when the terrain reflectivity is unknown. Fuze systems for munitions play two very important roles; one is to provide the safety of the munitions during storage, handling and carriage and the other is to provide exact timing for activation. One type of fuze which is used for airborne general purpose bombs is the proximity fuze with the ability to estimate height. These kinds of fuze sensors are desired to produce an activation signal at a specific height, however, they cannot measure the exact height and generate the trigger signal generally somewhere between 2 and 12 meters depending on the land clutter. The purpose of this article is to estimate the height of the ballistic platforms for detonation at a specific height with accuracy for different type of terrains.

Modulated waveforms are used for to increase the range resolution of fuzes, however, there are limiting factors in proximity applications. Use of CW, with a pre-set threshold level, is a simple method - immune to the problems of modulated signals although highly suscepti-

ble to the variations in the target's back scattering properties. The method presented in this study benefits from the following: simplicity of CW and immunity to variations in target's backscattering properties. Independent measurements of the rate of change in return power and Doppler shift (rate of change in height) allow the sensor's height to be estimated when terrain reflectivity is unknown.

The introduced method can be used effectively to estimate the sensor's proximal distance with a small relative error if the region of interest is shorter than 30 meters. Using this method, the height of the ballistic platform can be estimated with a simpler manner compared to Pulsed Doppler or FMCW altimeter sensor systems. Signal processing capability must be higher for our proposed method when compared with conventional proximity sensors. Moreover, processor solutions with sufficient process capability are easy to find at reasonable prices.

The theory is simple and seems applicable for a sensor system. However, the derivative of the received voltage used for estimation is very sensitive to the errors in the received voltage thus small variations of the received voltage causes large estimation errors. An effective signal processing is crucial to achieve a good estimation.

6.2 Future Studies

The noise analysis and some simple improvements for height estimation have been analysed in Section 4.3. Digital Signal Processing techniques must be investigated for better noise cancellation to get better results in estimation.

Multipath propagation may occur due to the reflections from the multiple surfaces and various man-made structures over the terrain. The effect of multipath propagation can be problematic. The multipath propagation causes additional Doppler frequencies [38] which result in Doppler spread in the spectrum. Additional Doppler frequencies, in the worst case, may result in false measurement of the sensor velocity. However, the frequency component with the highest amplitude will be resulted from the nearest distance from sensor to terrain when the sensor is at the near-to-the-terrain region. Moreover, due to the band spreading nature of the multipath signal, the multipath signal can be rejected by narrow band filtering [39] in a CW application. Multipath effect also cause rapid fluctuations in return signal's amplitude and phase due to the high velocity of the sensor. Adverse effects of these rapid amplitude fluctuations can be

decreased by averaging the return signal. A detail study for Multipath Effect Analysis will improve the results of the simulation. The results observed after adding the multipath effect will be a guide for improvement in Digital Signal Processing techniques.

The height estimation is based on the rate of amplitude change in the return signal and the Doppler shift. Both amplitude and the Doppler shift of the return signal is corrupted by additive random noise and interference of different kinds. When the signal is corrupted by noise and interference, we need to extract the desired signal from this data. The height can be estimated using the extracted data obtained from the noisy environment. Then the estimation can be compared with the previous estimations. A convenient solution for this sequential approach is the recursive filters such as Kalman or extended Kalman filters. In fact, the Kalman filter estimates the current state of the system by a recursive weighted least-squares method with special weighting using the previous estimations [40]. This approach can be called a form of Linear regression which have been proved to be useful for height estimation from a noisy return signal in Section 4.3.3.2. Kalman filter can be used for better estimation using the initial height estimation. The correction factor in Section 3.1.2 proved to improve the initial height estimation at a very good amount. The initial parameters such as initial velocity (v_0), tilt angle (ζ), and a good guess of the clutter ($\sigma_0(\psi)$) play a very important role for a well corrected estimation. While these information is used for correction factor, they can also be used in Kalman Filter for better estimation of the height and the results can be improved by using Kalman Filter technique.

The theory needs to be proved by a laboratory prototype at the final stage. Thus the RF circuitry can be implemented as a single channel Doppler system given in Figure 4.8. Digital signal processing techniques and the limitations of the system can be investigated using this laboratory prototype.

An air-borne platform approaching towards the sensor can be thought as a single clutter patch. The possibility of using this technique for the proximity measurement against air-borne moving platforms such as aircrafts or ballistic missiles can be studied as a future work as a new proximity sensor for air-to-air munitions or air defence missiles.

REFERENCES

- [1] W. S. Jr. Hinman and C. Brunetti. Radio proximity-fuze development. In *Proceedings of the IRE*, volume 34, pages 976–986, Dec 1946.
- [2] R.W. Burns. Early history of the proximity fuze (1937-40). *Science, Measurement and Technology, IEE Proceedings A*, 140(3):224–236, May 1993.
- [3] L. Brown. The origins of the proximity fuze. In *Microwave Symposium Digest, 1998 IEEE MTT-S International*, volume 2, pages 425–428, Jun 1998.
- [4] M.A. Kolodny. Radar proximity fuzing and the cold war paradigm. In *Microwave Symposium Digest (MTT), 2011 IEEE MTT-S International*, pages 1–4, 5-10 Jun 2011.
- [5] G.R. Osche and D.S. Young. Imaging laser radar in the near and far infrared. *Proceedings of the IEEE*, 84(2):103–125, Feb 1996.
- [6] E. Lissel, H. Rohling, and W. Plagge. Radar sensor for car applications. In *Vehicular Technology Conference, 1994 IEEE 44th*, volume 1, pages 438–442, Jun 1994.
- [7] S. Fericean, A. Dorneich, R. Droxler, and D. Krater. Development of a microwave proximity sensor for industrial applications. *Sensors Journal, IEEE*, 9(7):870–876, Jul 2009.
- [8] M.D. Pollman, P. Katzin, B. Bedard, V. Aparin, W. Grammer, and R. Orgusaar. A MMIC radar chip for use in air-to-air missile fuzing applications. In *Microwave Symposium Digest, 1996., IEEE MTT-S International*, volume 1, pages 253–256, Jun 1996.
- [9] Yuan Ping, Zhang He, Chen Bingling, and Sun Lei. Research and application of multi-function electronic fuze. In *Circuits and Systems, 2004. MWSCAS '04. The 2004 47th Midwest Symposium on*, volume 2, pages 261–264, Jul 2004.
- [10] I.I. Immoreev and P.G.S.D.V. Fedotov. Ultra wideband radar systems: Advantages and disadvantages. In *Ultra Wideband Systems and Technologies, 2002. Digest of Papers. 2002 IEEE Conference on*, pages 201–205, 2002.
- [11] R.J. Fontana. Recent system applications of short-pulse ultra-wideband (UWB) technology. *Microwave Theory and Techniques, IEEE Transactions on*, 52(9):2087–2104, Sep 2004.
- [12] I.Y. Immoreev. Practical applications of UWB technology. *Aerospace and Electronic Systems Magazine, IEEE*, 25(2):36–42, Feb 2010.
- [13] L. ZhaoBo. Implementation and development of compact UWB proximity fuze sensor system. In *Computational Problem-Solving (ICCP), 2011 International Conference on*, pages 120–122, Oct 2011.

- [14] F. Herbert. Ultra wideband technology for precision proximity fuzing [PDF Document]. In *49th Annual Fuze Conference*. Seattle, WA, 5-7 Apr 2005. Retrieved from http://proceedings.ndia.org/5560/Wednesday/Session_III-A/Fluhler.pdf [Accessed 27 April 2012].
- [15] S. Kurt, Ş. Demir, and A. Hızal. Zero-crossing counter for accuracy improvement of FMCW range detection. *Turk Journal of Electronic Engineers*, 16(2), 2008. TÜBİTAK.
- [16] S.O. Piper. FMCW radar range resolution effects with sinusoidal nonlinearities in the frequency sweep. In *Record of the IEEE 1995*, volume International, pages 563–567. Radar Conference, 8-11 May 1995.
- [17] Y. Tokieda, H. Sugawara, S. Niimura, and T. Fujise. High precision waterlevel gauge with an FMCW radar under limited bandwidth. In *Radar Conference, 2005*, pages 339–342. EURAD 2005, 6-7 Oct 2005.
- [18] M. Pichler, A. Stelzer, P. Gulden, and M. Vossiek. Influence of systematic frequency-sweep non-linearity on object distance estimation in FMCW/FSCW radar systems. In *33rd European Microwave Conference, 2003*, volume 3, pages 1203–1206, 7-9 Oct 2003.
- [19] M. Secmen, K. Topalli, M. Unlu, E. Erdil, O.A. Civi, and A. Hızal. Dual wideband antenna analysis for linear FMCW radar applications. In *Signal Processing and Communications Applications*, pages 1–4. IEEE 2006, 17-19 Apr 2006.
- [20] G.P. Kulemin. Clutter rejection in short-range radar with uncoded and wideband pulsed signals. In *Physics and Engineering of Millimeter and Submillimeter Waves, 1998. MSMW '98. Third International Kharkov Symposium*, volume 2, pages 523–525, Sep 1998.
- [21] Max Perrin. New Generation Artillery Proximity Sensor, Application to Naval Fuzes. <http://www.dtic.mil/ndia/2008fuze/IVAPerrin.pdf>, 2008. [Online].
- [22] Robert P. Hertlein. Extended Range Guided Munition Height-of-Burst Sensor. <http://www.dtic.mil/ndia/2003fuze/hertlien.pdf>, 2003. [Online].
- [23] Robert P. Hertlein. High Accuracy Radar Proximity Sensor (HARPS). <http://www.dtic.mil/ndia/2004fuze/hertlein.pdf>, 2004. [Online].
- [24] Michael J. Balk. The Evolution of the DSU-33 C/B Proximity Sensor, A Success in Customer-Contractor Partnership. <http://www.dtic.mil/ndia/2006fuze/balk.pdf>, 2006. [Online].
- [25] D.K. Barton and S.A. Leonov. *Radar Technology Encyclopedia*. Artech House, Inc., Electronic edition, 1998.
- [26] F.E. Nathanson. *Radar Design Principles*. McGraw Hill, Third edition, 1991.
- [27] M.I. Skolnik. *Introduction to Radar Systems*. McGraw Hill, Newyork, Second edition, 2000.
- [28] M.I. Skolnik. *Radar Handbook*. McGraw Hill, Second edition, 1990.

- [29] R.M. Narayanan, D.W.Doerr, and D.C. Rundquist. Temporal decorrelation of x-band backscatter from wind influenced vegetation. *Transactions on Aerospace and Electronic Systems*, 28(2), Apr 1992.
- [30] J.B. Billingsley, A. Farina, F. Gini, M.V. Greco, and L. Verrazzani. Statistical analyses of measured radar ground clutter data. *IEEE Transactions on Aerospace and Electronic Systems*, 35(2):579–593, Apr 1999.
- [31] M.W. Long. *Radar Reflectivity of Land and Sea*. Artech House, Third edition, 2001.
- [32] D.K. Barton. Land clutter models for radar design and analysis. In *Proceedings of the IEEE*, volume 73, pages 198–204, Feb 1985.
- [33] Mini-Circuits. ROS-3600-619+ Voltage Controlled Oscillator Datasheet. <http://www.minicircuits.com/pdfs/ROS-3600-619+.pdf>, 2012. [Online PDF Document].
- [34] Altunkan HIZAL. Supplementary lecture notes for EE-625 Radar Systems. Middle East Technical University, Ankara, 2001. Part-X.
- [35] D.K. Barton and S.A. Leonov. *Radar Technology Encyclopedia*. Artech House, London, electronic edition edition, 1998.
- [36] N.R. Draper and H. Smith. *Applied Regression Analysis*. Wiley, 1981.
- [37] Mil-Prf-89020B. *Performance Specification Digital Terrain Elevation Data*. 12310 Sunrise Valley Drive, Reston, Va, 23 May 2000.
- [38] V.F. Mecca, D. Ramakrishnan, and J.L. Krolik. Mimo radar space-time adaptive processing for multipath clutter mitigation. In *Sensor Array and Multichannel Processing, 2006. Fourth IEEE Workshop on*, pages 249–253, july 2006.
- [39] E.I. Muehldorf. The effect of multipath reflections on spaceborne interferometer accuracy. *Aerospace and Electronic Systems, IEEE Transactions on*, AES-7(1):122–131, jan. 1971.
- [40] J. Mochnac, S. Marchevsky, and P. Kocan. Bayesian filtering techniques: Kalman and extended kalman filter basics. In *Radioelektronika, 2009. RADIOELEKTRONIKA '09. 19th International Conference*, pages 119–122, april 2009.

APPENDIX A

MATLAB CODES IN THE SIMULATION

A.1 Codes for Estimating Height from a Single Planar Surface

A.1.1 Calculating Trajectory of the Ballistic Platform

```
function [t,h,x,Vz,Vx,V,Z,time]=newtrajectory(h0,V0,Zeta,samptime)

i=1;
t=0;h=[];x=[];Vz=[];Vx=[];V=[];Z=[];
g=9.81; %meters per second
Z(1)=Zeta;
Zeta=Zeta*pi/180;
time(1)=0;
h(1)=h0;
x(1)=0;
V(1)=V0;
Vx(1)=V*cos(Zeta);
Vz(1)=V*sin(Zeta);

while (h(i)-Vz(i)*samptime*10^-3-0.5*g*(samptime*10^-3)^2)>=0
    t=t+(samptime*10^-3);
    Vz(i+1)=Vz(i)+g*samptime*10^-3;
    Vx(i+1)=Vx(i);
    Z(i+1)=atan(Vz(i+1)/Vx(i+1))*180/pi;
    h(i+1)=h(i)-Vz(i)*samptime*10^-3-0.5*g*(samptime*10^-3)^2;
    x(i+1)=x(i)+Vx(i)*samptime*10^-3;
    V(i+1)=sqrt(Vz(i)^2+Vx(i)^2);
    time(i+1)=time(i)+(samptime*10^-3);
    i=i+1;
end
```

A.1.2 Generating Exponential Model of the Land Clutter

```

function [expcoeff]=lcfite(SmaxdB,G0dB,SmindB,PolyDeg)

%[expcoeff]=lcfite(SmaxdB,G0dB,SmindB,PolyDeg) land clutter fitting tool;
%Output is in DB and the angle is the one between the surface normal and
%thedirection of propagation and is in DEGREES.
%SmaxdB=input('Maksimum sigma value at Zeta 0 Degree (dB)=');
%G0dB=input('Gama for Zeta 20-80 Degrees (dB)=');
%SmindB=input('Minimum sigma value at Zeta 90 Degrees (dB)=');
%PolyDeg=input('Degree of the curve fitting polynomial=');
%Output of this function is the coefficients of the curve fitting polynomial
%of PolyDeg degree and land clutter data and exponential fit coefficients.
%ydata=land clutter model
%ydatadb=land clutter model (dB)
%coeffdb=polynomial coefficients
%expcoeff=exponential coefficients

Smax=10^(SmaxdB/10);
Smin=10^(SmindB/10);
G0=10^(G0dB/10);
polytype=strcat('Poly',num2str(PolyDeg));

%Construct ydata
%Zeta=0-20 degrees => exponential   y=A*exp(-a*Z)+B
%Zeta=20-80 degrees => cosine       y=Gama*cos(Z)
%Zeta=80-90 degrees => loglinear

%For 0-20 degrees
B=G0dB+log10(cos(20*pi/180))-5;
A=SmaxdB-B;
a=-1/20*log((G0dB+log10(cos(20*pi/180))-B)/A);
i=0:20;
ydatadb(i+1)=A*exp(-a*i)+B;
ydata(i+1)=10.^(ydatadb/10);

%For 20-80 degrees
j=21:80;
ydata(j+1)=G0*cos(j*pi/180);
ydatadb(j+1)=10*log10(ydata(j+1));

%For 80-90 degrees
k=81:90;
egim=(10*log10(G0*cos(80*pi/180))-SmindB)/10;
ydatadb(k+1)=10*log10(G0*cos(80*pi/180))-(k-80)*egim;
ydata(k+1)=10.^(ydatadb(k+1)/10);
ydata=(ydata)';
ydatadb=(ydatadb)';
xdata=(1:91)';

fitdata=fit(xdata,ydata,'Exp2');

% General model Exp2:
% a(x) = a*exp(b*x) + c*exp(d*x)
% expcoeff= [a b c d]

expcoeff=mean(confint(fitdata,0.95));
coeffdb=polyfit(xdata,ydatadb,PolyDeg);

```

A.1.3 Calculating Correction Factor by Initial Conditions

```
function [C]=corrfac2(Z,v0,Tb,Fb,c,sampletime,tol)

g=9.81; %meter/secondsquare
V=v0; %meter/second
% Z release angle in degree
Zeta=90-Z;
Vz=V*cos(Zeta*pi/180);
Vx=V*sin(Zeta*pi/180);
t=sampletime*0.001;

S=@(Ga) c(1).*exp(c(2).*(abs(Ga)))+c(3).*exp(c(4).*(abs(Ga)));
%while calculating land reflectivity zeta angle should be in degrees.

f1=S(90).*exp(-2.*log(2)).*cos((90).*pi/180);
f2=S(-90).*exp(-2.*log(2)).*cos((-90).*pi/180);

f3=@(T) -16.*log(2).*(Zeta-T)/Tb.^2.*S(T).*cos(T*pi/180).*exp(-8.*log(2)...
.*(Zeta-T)/Tb).^2).*10^4;

dZdt=-(Vx.*g)./((Vz+g.*t).^2+Vx.^2);

dIdZ=quadl(f3,-90,90)./10^4+f1-f2;

[It,If]=rpower3(Tb,Fb,90-Zeta,c,tol);

C=dZdt.*dIdZ.*sqrt(If./It)./2;
```

A.1.4 Calculating Reflected Power from the Terrain

```
function [It,If]=rpower3(Tb,Fb,z,c,tol)
%[It,If]=rpower3(Tb,Fb,Z,c)
%Tb:Elevation Beamwidth
%Fb:Horizontal Beamwidth
%z:Angle between trajectory axis (velocity vector) and horizontal axis
%c:Coefficients of the clutter exponential model calculated using lcfit.m
%Pr=4*K*It*If Pr:received power
%If:Integral over the azimuth
%It:Integral over the elevation

Tb=Tb*pi/180; Fb=Fb*pi/180;
wb=waitbar(0,'Calculating Parameters!');

for i=1:length(z)
Z=z(i)*pi/180;
Zi=pi/2-Z;

Tfunc=@(T) (c(1).*exp(c(2).*(abs(T).*180/pi))+c(3).*exp(c(4).*...
(abs(T).*180/pi))).*(exp(-2*log(2).*((T-Zi)./Tb).^2)).^4.*cos(T).*10^4;

Ffunc=@(F) (exp(-2.*log(2).*(F/Fb).^2)).^4.*10^4;

It(i)=quadl(Tfunc,-pi/2,pi/2,tol)./10^4;

If(i)=quadl(Ffunc,-pi/2,pi/2,tol)./10^4;

waitbar(i/length(z),wb);
end;

close(wb);
```

A.1.5 Graphical User Interface (GUI) Initialization (Automatically Generated by MATLAB™)

```
function varargout = ProjectGui1(varargin)
gui_Singleton = 1;
gui_State = struct('gui_Name',       mfilename, ...
                  'gui_Singleton',   gui_Singleton, ...
                  'gui_OpeningFcn',  @ProjectGui1_OpeningFcn, ...
                  'gui_OutputFcn',  @ProjectGui1_OutputFcn, ...
                  'gui_LayoutFcn',   [] , ...
                  'gui_Callback',    []);
if nargin && ischar(varargin{1})
    gui_State.gui_Callback = str2func(varargin{1});
end
if nargin
    [varargout{1:nargout}] = gui_mainfcn(gui_State, varargin{:});
else
    gui_mainfcn(gui_State, varargin{:});
end
function ProjectGui1_OpeningFcn(hObject, eventdata, handles, varargin)
handles.output = hObject;
guidata(hObject, handles);
function varargout = ProjectGui1_OutputFcn(hObject, eventdata, handles)
varargout{1} = handles.output;
function height_CreateFcn(hObject, eventdata, handles)
if ispc && isequal(get(hObject,'BackgroundColor'), ...
    get(0,'defaultUicontrolBackgroundColor'))
    set(hObject,'BackgroundColor','white');
end
function Velocity_CreateFcn(hObject, eventdata, handles)
if ispc && isequal(get(hObject,'BackgroundColor'), ...
    get(0,'defaultUicontrolBackgroundColor'))
    set(hObject,'BackgroundColor','white');
end
function ReleaseAngle_CreateFcn(hObject, eventdata, handles)
if ispc && isequal(get(hObject,'BackgroundColor'), ...
    get(0,'defaultUicontrolBackgroundColor'))
    set(hObject,'BackgroundColor','white');
end
function sampletime_CreateFcn(hObject, eventdata, handles)
if ispc && isequal(get(hObject,'BackgroundColor'), ...
    get(0,'defaultUicontrolBackgroundColor'))
    set(hObject,'BackgroundColor','white');
end
function Smin_CreateFcn(hObject, eventdata, handles)
if ispc && isequal(get(hObject,'BackgroundColor'), ...
    get(0,'defaultUicontrolBackgroundColor'))
    set(hObject,'BackgroundColor','white');
end
function power_CreateFcn(hObject, eventdata, handles)
if ispc && isequal(get(hObject,'BackgroundColor'), ...
    get(0,'defaultUicontrolBackgroundColor'))
    set(hObject,'BackgroundColor','white');
end
function frequency_CreateFcn(hObject, eventdata, handles)
if ispc && isequal(get(hObject,'BackgroundColor'), ...
    get(0,'defaultUicontrolBackgroundColor'))
    set(hObject,'BackgroundColor','white');
end
function gain_CreateFcn(hObject, eventdata, handles)
```



```
if ispc && isequal(get(hObject,'BackgroundColor'), ...  
    get(0,'defaultUicontrolBackgroundColor'))  
    set(hObject,'BackgroundColor','white');  
end  
function calmethod_CreateFcn(hObject, eventdata, handles)  
  
global selection;  
selection=1;
```

A.1.6 Height Estimation and Displaying Results in GUI

```

function calculatebutton1_Callback(hObject, eventdata, handles)
global releaseangle velocity height slang sloff selection expcoeff;

sampletime=str2num(get(handles.sampletime,'String'));
releaseangle=str2num(get(handles.ReleaseAngle,'String'));
velocity=str2num(get(handles.Velocity,'String'));
height=str2num(get(handles.height,'String'));

reflection_coefficient (hObject, eventdata, handles);

txpowerdBm=str2num(get(handles.power,'String'));
frequency=str2num(get(handles.frequency,'String'));
gaindB=str2num(get(handles.gain,'String'));

Tb=str2num(get(handles.teta,'String'));
Fb=str2num(get(handles.phi,'String'));

tol=10^(str2num(get(handles.tol,'String')));

sloff=str2num(get(handles.sloff,'String'));
slang=str2num(get(handles.slang,'String'));

t=0;h=[];y=[];Vz=[];Vx=[];V=[];Z=[];time=[];

[t,h,y,Vz,Vx,V,Z,time]=newtrajectory(height,velocity,releaseangle,sampletime);

txpower=10^(txpowerdBm/10-2); %watt
gain=10^(gaindB/10);
lambda=0.3/frequency; %m
K=txpower*gain^2*lambda^2/(4*pi)^3; %W/m^2
set(handles.K,'String',K);

axes(handles.axes1);

if selection
    [It,If]=rpower3(Tb,Fb,Z,expcoeff,tol);
    Ia=It.*If;
    hreal=h;
    cla
else
    [Ia,hslp,Vzslp,ys,beta]=rpowerslp(Tb,Fb,Z,expcoeff,h,y,Vz,sloff,slang,tol);
    %reduce the dimensions if the sensor hits the slope
    hreal=reducelength(h,hslp);
    h=hslp;
    Vz=Vzslp;
    y=reducelength(y,hslp);
    time=reducelength(time,hslp);
    Vx=reducelength(Vx,hslp);
    V=reducelength(V,hslp);
    Z=reducelength(Z,hslp);
    beta=reducelength(beta,hslp);
    cla
    line([ys ys+300*cos(slang*pi/180)], [0 300*sin(slang*pi/180)]);
end

hold on
plot(y,hreal);
title('Trajectory');

```

```

text(y(round(length(y)/2)),h(round(length(h)/2)),' \leftarrow Height');
xlabel('Horizontal Distance (m)');ylabel('Vertical Distance (m)')
hold off

axes(handles.axes2);
cla
plot(time,Vz,'c');
hold on;
title('Velocity vs Time');
text(time(round(length(time)/10)),Vz(round(length(Vz)/10)),' \leftarrow Vz');
plot(time,Vx,'r');
text(time(round(length(time)/2.5)),Vx(round(length(Vx)/2.5)),' \leftarrow Vx');
plot(time,V);
text(time(round(length(time)/1.5)),V(round(length(V)/1.5));
xlabel('Time (s)');ylabel('Velocity (m/s)');

axes(handles.axes4)
plot(Z,Ia)
text(Z(round(length(Ia)/3)),Ia(round(length(Ia)/3)),' \leftarrow Integral Value');
title('Integral Value');
xlabel('Grazing Angle');ylabel('Integral Value');

axes(handles.axes5)
Pr=K.*Ia./h.^2;
semilogy(h,Pr)
text(h(round(length(h)/2)),Pr(round(length(Pr)/2)),' \leftarrow Power');
title('Received Power vs Height');
xlabel('Height (m)');ylabel('Received Power (W)');
set(handles.axes5,'XDir','reverse')

axes(handles.axes6)

doppler=2.*Vz./lambda;
Vrec=sqrt(100*Pr);

mVz=[];mIa=[];mh=[];mdoppler=[];Vr=[];dVr=[];hest=[];
cla

wb2=waitbar(0,'Estimating Height!');

for i=1:(length(Vrec)-1)
    mVr(i)=(Vrec(i+1)+Vrec(i))/2;
    mVz(i)=(Vz(i+1)+Vz(i))/2;
    mIa(i)=(Ia(i+1)+Ia(i))/2;
    mh(i)=(h(i+1)+h(i))/2;
    mtime(i)=time(i);
    waitbar(i/(length(Vrec)-1),wb2);
end

doppler(1)=[];
mdoppler=doppler;

close(wb2);

%FINAL ESTIMATION
dVr=diff(Vrec)*10^3/sampletime;
hest=mVr./dVr.*mdoppler.*lambda./2;

hold on
dIadt=(sqrt(Ia(2))-sqrt(Ia(1)))*10^3/sampletime;

```

```

set(handles.mancorfac,'String',dIadt);

%If calculation with two slopes selected C coefficient won't be calculated
if selection
    C=corrfac2(releaseangle,velocity,Tb,Fb,expcoeff,samplertime,tol);
    set(handles.corfactor,'String',C);
else
    C=dIadt(1);
    set(handles.corfactor,'String','Not Calc.');
```

end

```

dIadt=C;
hcor=(sqrt(100*K)*dIadt+mVr.*mVz)./dVr;

title('Height vs Time');
xlabel('Time(s)');ylabel('Height (m)');
```

```

text(time(round(length(time)/8)),mh(round(length(mh)/8))...
    ,'\leftarrow Actual Height');
text(time(round(length(time)/3)),hest(round(length(hest)/3))...
    ,'\leftarrow Estimation');
```

```

if (selection)
text(time(round(length(time)/4)),hcor(round(length(hcor)/4))...
    ,'\leftarrow Corrected Estimation');
```

end

```

plot(mtime,mh,'b')
plot(mtime,hest,'r')
plot(mtime,hcor,'-.r')
```

```

axis([0 max(mtime) 0 max(max(max(mh,hest),hcor))])

axes(handles.axes7)
cla
grid on
hold on
title('Relative Error');
xlabel('Height (m)');ylabel('Error');
```

```

hesterr=(hest-mh)./mh*100;
hcorerr=(hcor-mh)./mh*100;

plot(mh,hesterr,'b')
if (selection)
    plot(mh,hcorerr,'-.r')
else
    plot(mh,hcorerr,'-.r')
end
```

```

if (height>=300)
    axis([ min(mh) 300 -inf inf])
else
    axis auto
end
set(gca,'XDir','reverse');
legend('Estimated','Corrected');
legend('Location','SouthEast');
plot(mh,hesterr,'b');
```

```

msgbox('Estimation Completed!');

function pushbutton2_Callback(hObject, eventdata, handles)
global releaseangle velocity height slang sloff;
cd ('C:\Program Files\MATLAB\R2006a\work\sonuclar');
a=clock;
SavedFigure=[ datestr(date) '_r' num2str( releaseangle ) '_v' ...
    num2str(velocity) '_h' num2str( height) '_s' num2str(slang) '_s' ...
    num2str(sloff) '_h' num2str(a(4)) '_t' num2str(a(5))]
saveas(gcf,SavedFigure,'emf');
cd ..

function calmethod_SelectionChangeFcn(hObject, eventdata, handles)
global selection;
switch get(hObject,'Tag')
    case 'radiobutton1'
        selection=1;
    case 'radiobutton2'
        selection=0;
end

function reflection_coefficient (hObject, eventdata, handles)
global smax smin gamma expcoeff;
axes(handles.axes3);
smax=str2num(get(handles.Smax,'String'));
gamma=str2num(get(handles.Gamma,'String'));
smin=str2num(get(handles.Smin,'String'));
expcoeff=lcfit(smax,gamma,smin,4);
i=0:90;
a=expcoeff(1).*exp(expcoeff(2).*(i+1))+expcoeff(3).*exp(expcoeff(4).*(i+1));
semilogy(90-i,a)
text(i(round(length(i)/1.5)),a(round(length(a)/3)),' \leftarrow Land Clutter');
title('Land Clutter Model');
xlabel('Grazing Angle');ylabel('Land Reflectivity');
set(handles.axes3,'XDir','reverse')
set(handles.axes3,'XLim',[0 90])

```

A.2 Codes for Estimating Height from the Terrain Composed of Two-Planes

A.2.1 Calculating Reflected Power from Two-Planes

```
function [I,hslep,Vzslp,ys,beta]=rpowersp(Tb,Fb,z,c,h,y,Vz,yoff,alfa,tol)

%Tb:Elevation Beamwidth
%Fb:Horizontal Beamwidth
%z:Angle between trajectory axis (velocity vector) and horizontal axis
%c:Coefficients of the clutter exponential model calculated using lcfite.m
%h is the height, y is y position of the sensor
%p is the position vector of sensor at (x,y,z)
%alfa is the angle of the slope and
%ys is the distance of the start of the slope to the impact point

Tb=Tb*pi/180;
Fb=Fb*pi/180;
alfa=alfa*pi/180;
ys=max(y)+yoff;

wb3=waitbar(0,'Calculating Parameters!');

for i=1:length(z)
Z=z(i)*pi/180;
Zi=pi/2-Z;
%beta is the angle of the line from slope start to sensor position
beta(i)=atan2(h(i),(ys-y(i)));

Ga=@(T,F) atan(sqrt(tan(T).^2+tan(F).^2));

cossin=@(T,F) 1./((1+tan(T).^2+tan(F).^2).^2.*cos(T).^2.*cos(F).^2);

func=@(T,F) (c(1).*exp(c(2).*abs(Ga(T,F)).*180/pi)) + c(3)...
.*exp(c(4).*abs(Ga(T,F)).*180/pi))...
.*(exp(-2*log(2).*(T-Zi)./Tb).^2).^4 ...
.*(exp(-2*log(2).*(F./Fb).^2)).^4 ...
.*cossin(T,F).*10^4;

func2=@(T,F) (c(1).*exp(c(2).*abs(Ga(T,F)).*180/pi)) + c(3)...
.*exp(c(4).*abs(Ga(T,F)).*180/pi))...
.*(exp(-2*log(2).*(T-(Zi-alfa))./Tb).^2).^4 ...
.*(exp(-2*log(2).*(F./Fb).^2)).^4 ...
.*cossin(T,F).*10^4;

if alfa ==0
I(i)=dblquad(func,-pi/2,pi/2,-pi/2,pi/2,tol)./10^4;
Vzslp(i)=Vz(i);
hslep(i)=h(i);
else
if sin(beta(i)+alfa)/sin(beta(i))>0

I(i)=dblquad(func,-pi/2,(pi/2-beta(i)), -pi/2,pi/2,tol)./10^4+ ...
dblquad(func2,(pi/2-beta(i)-alfa),pi/2,-pi/2,pi/2,tol)./10^4;

if beta(i)<=((pi-alfa)/2)
hslep(i)=h(i);
Vzslp(i)=Vz(i);
else
hslep(i)=h(i)./sin(beta(i)).*sin(beta(i)+alfa);
```

```
        Vzslp(i)=Vz(i).*cos(Zi-alfa)./cos(Zi);
    end;
end;
end;
waitbar(i/length(z),wb3);
end;
close(wb3)
```

A.3 Codes for Estimating Height from the Terrain Generated Using DTED

A.3.1 Calculating Trajectory over DTED Terrain

```
function [h,z,x,y,Vz,Vx,V,time]=trajectory(x0,y0,z0,V0,Zeta0,samplertime,terrain)

i=1;
t=0;z=[];x=[];y=[];Vz=[];Vx=[];V=[];Zeta=[];time=[];
g=9.81; %metre/saniyekare
%Zeta0 is the release angle; Angle between the sensor and the horizon.
Zeta0=Zeta0*pi/180;
time(1)=0;
z(1)=z0;
x(1)=x0;
y(1)=y0;
V(1)=V0;
Vx(1)=V0*cos(Zeta0);
Vz(1)=-V0*sin(Zeta0);
dx=V0*cos(Zeta0)*samplertime*10.^-3;

while ((z(i)-Vz(i).*samplertime*10.^-3-0.5*g*(samplertime.*10.^-3).^2)>=0);
    t=t+(samplertime*10^-3); %in seconds
    Vz(i+1)=Vz(i)-g*samplertime*(10.^-3);
    Vx(i+1)=Vx(i);
    y(i)=y0;
    z(i+1)=z(i)+Vz(i).*samplertime.*(10.^-3)+0.5*g*(samplertime.*10.^-3)^2;
    x(i+1)=x(i)+dx;
    V(i+1)=sqrt(Vz(i).^2+Vx(i).^2);
    time(i+1)=time(i)+(samplertime*10.^-3);
    i=i+1;
end

terrainpiece=interp1(terrain,x);
h=z-terrainpiece;
index=0;

for i=1:length(h);
    index=index+1;
    if (h(index)<0)
        index=index-1;
        break
    end
end

if (index+1)<length(time);
    time(index+1:length(time))=[]; %time vector
    Vz(index+1:length(Vz))=[];%vertical velocity
    Vx(index+1:length(Vx))=[];%horizontal velocity
    z(index+1:length(z))=[];%height (MSL)
    x(index+1:length(x))=[];
    y(index+1:length(y))=[];
    h(index+1:length(h))=[];
end
```


A.3.2 Adjusting DTED Limits

```
function [Zs,RMs,Smallmaporigin]=reducemapsize(Z,RM,Maporigin,x,y,h,mode)

Zs=Z;
mapylim=[Maporigin(2) (Maporigin(2)+deg2km((size(Z,1)-1)/RM(1))*1000)];
mapxlim=[Maporigin(1) (Maporigin(1)+deg2km((size(Z,2)-1)/RM(1))*1000)];

if (y-h)>mapylim(1)
    m=round(km2deg((y-h-mapylim(1))/1000)*RM(1));
    mdimS=round(km2deg(h/1000)*RM(1));
else
    m=0;
    mdimS=round(km2deg((y-mapylim(1))/1000)*RM(1));
end

if (y+h)>mapylim(2)
    mdimN=round(km2deg((mapylim(2)-y)/1000)*RM(1));
else
    mdimN=round(km2deg(h/1000)*RM(1));
end

if (x-h)>mapxlim(1)
    n=round(km2deg((x-h-mapxlim(1))/1000)*RM(1));
    ndimW=round(km2deg(h/1000)*RM(1));
else
    n=0;
    ndimW=round(km2deg((x-mapxlim(1))/1000)*RM(1));
end

if (x+mode*h)>mapxlim(2)
    ndimE=round(km2deg((mapxlim(2)-x)/1000)*RM(1));
else
    ndimE=round(km2deg(mode*h/1000)*RM(1));
end

mdim=mdimN+mdimS;
ndim=ndimE+ndimW;

if mdim>(size(Z,1)-1)
    mdim=(size(Z,1)-1);
end

if ndim>(size(Z,1)-1)
    ndim=(size(Z,1)-1);
end

%First the far elements must be erased
if (m+mdim+2)<size(Z,1);
    Zs(m+mdim+2):size(Z,1),:=[];
end

if m>1
    Zs(1:m),:=[];
end

if n+ndim+2<size(Z,2)
    Zs(:,(n+ndim+2):size(Z,2))=[];
end
```

```
if n>1
Zs(:,(1:n))=[];
end

Smallmaporigin=[(Maporigin(1)+ deg2km(n/RM(1))*1000) (Maporigin(2)...
+ deg2km(m/RM(1))*1000)];

Newlatitude = km2deg(Smallmaporigin(2)/1000)+mdim/RM(1);
Newlongitude = km2deg(Smallmaporigin(1)/1000);

RMs=[RM(1) Newlatitude Newlongitude];
```

A.3.3 Decreasing DTED Resolution (Increase in DTED Spacing)

```
function [Z R] = refine(Z,R, ratio)

sz=size(Z);
newindex=1;
control=1;

for i=1:(sz(1)-1);
    newindex=newindex+1;
    if control<ratio
        Z(newindex,:)=[];
        newindex=newindex-1;
        control=control+1;
    else
        control=1;
    end
end
newindex=1;
control=1;

for i=1:(sz(2)-1);
    newindex=newindex+1;
    if control<ratio
        Z(:,newindex)=[];
        newindex=newindex-1;
        control=control+1;
    else
        control=1;
    end
end

R=[R(1)/ratio (length(Z)-1)/R(1)*ratio 0];
end
```

A.3.4 Triangulation and Calculation Reflections from Clutter Elements

```

function [xcentroid,ycentroid,receivedpower,dopplershift]=...
    calculate_reflection(Z,RM,Maporigin,Vismap,x,y,z,Vx,Vy,Vz,...
        expcoeff,K,frequency,Beamwidth)
Velocity=norm([Vx Vy Vz]);
VelocityVector=[Vx Vy Vz]/Velocity;

receivedpower=zeros(2*(size(Z,1)-1),(size(Z,2)-1));
dopplershift=receivedpower;
xcentroid=receivedpower;
ycentroid=receivedpower;

for m=1:(size(Z,1)-1)
    for n=1:(size(Z,2)-1)
        P1=[Maporigin(1) + deg2km((n-1)/RM(1))*1000, (Maporigin(2)...
            + deg2km((m-1)/RM(1))*1000), Z(m,n) ];
        P2=[Maporigin(1) + deg2km((n-1)/RM(1))*1000, (Maporigin(2)...
            + deg2km((m)/RM(1))*1000), Z(m+1,n) ];
        P3=[Maporigin(1) + deg2km((n)/RM(1))*1000, (Maporigin(2)...
            + deg2km((m-1)/RM(1))*1000), Z(m,n+1) ];
        centroid=(P1+P2+P3)/3;

        if (Vismap(m+1,n) && Vismap(m,n+1) && Vismap(m+1,n+1))
            [receivedpower(2*m-1,n), dopplershift(2*m-1,n)]=power(P1,P2,P3...
                ,centroid,VelocityVector,Velocity,x,y,z,expcoeff,K,...
                frequency,Beamwidth);
        else
            receivedpower(2*m-1,n)=NaN;
        end

        xcentroid(2*m-1,n)=centroid(1,1);
        ycentroid(2*m-1,n)=centroid(1,2);

        P1=[Maporigin(1) + deg2km((n-1)/RM(1))*1000, (Maporigin(2)...
            + deg2km((m)/RM(1))*1000), Z(m+1,n) ];
        P2=[Maporigin(1) + deg2km(n/RM(1))*1000, (Maporigin(2)...
            + deg2km((m)/RM(1))*1000), Z(m+1,n+1) ];
        P3=[Maporigin(1) + deg2km(n/RM(1))*1000, (Maporigin(2)...
            + deg2km((m-1)/RM(1))*1000), Z(m,n+1) ];
        centroid=(P1+P2+P3)/3;

        if (Vismap(m,n) && Vismap(m+1,n) && Vismap(m,n+1))
            [receivedpower(2*m,n), dopplershift(2*m,n)]=power(P1,P2,P3,...
                centroid,VelocityVector,Velocity,x,y,z,expcoeff,K,...
                frequency,Beamwidth);
        else
            receivedpower(2*m,n)=NaN;
        end
        xcentroid(2*m,n)=centroid(1,1);
        ycentroid(2*m,n)=centroid(1,2);
    end
end

function [ReceivedPower,Dopplershift]=power(P1,P2,P3,centroid,...
    VelocityVector,Velocity,x,y,z,expcoeff,K,frequency,Beamwidth)

u=cross(P3-P1,P2-P1);
surfacenormal=u/norm(u);
R=norm(centroid-[x y z]);

```

```

RVector=(centroid-[x y z])/R;

ons = [1 1 1];
X=[P1(1) P2(1) P3(1)];
Y=[P1(2) P2(2) P3(2)];
Z=[P1(3) P2(3) P3(3)];

Area = 0.5*sqrt(det([X;Y;ons])^2 + det([Y;Z;ons])^2 + det([Z;X;ons])^2);

GrazingAngle = rad2deg(atan2 (norm(cross(-RVector , surfacenormal))...
    ,dot(-RVector , surfacenormal)));

AntennaAngle = rad2deg(atan2 (norm(cross(RVector , VelocityVector))...
    ,dot(RVector , VelocityVector)));

Reflectivity = expcoeff(1).*exp(expcoeff(2).*(GrazingAngle))+expcoeff(3)...
    .*exp(expcoeff(4).*(GrazingAngle));

ReceivedPower = K* exp(-2*log(2)*(0.5*AntennaAngle/Beamwidth)^2)...
    *Area* Reflectivity /R^4;

Dopplershift = 2* Velocity * cos(deg2rad(AntennaAngle))* (frequency/.3);

```

CURRICULUM VITAE

PERSONAL INFORMATION

Surname, Name : Aydın VURAL
Nationality : Turkish (T.C.)
Date and Place of Birth : 15 April 1978, Konya
Marital Status : Married
Phone : 0090 530 327 3113
e-mail : e1219526@metu.edu.tr

EDUCATION

Degree	Institution	Year of Graduation
MS	METU Electrical and Electronics Engineering	2002
BS	Hacettepe Uni. Electrical and Electronics Engineering	1999
High School	Erzurum Science High School	1995

WORK EXPERIENCE

Year	Place	Enrollement
2011-Present	Turkish Air Force Head Quarters	EW Project Management Officer
2009-2011	3 rd Air Supply and Maintenance Center	Chief of R&D Group
2004-2007	3 rd Air Supply and Maintenance Center	Chief of Quality Control
1999-2004	3 rd Air Supply and Maintenance Center	Chief of Production

FOREIGN LANGUAGES

Advanced English, Beginner German.

HOBBIES

Swimming, Scuba Diving, Under Water Hockey, Life-Guarding, Motorcycle, Chess.